

NANOPOROUS ANODIC ALUMINA MEMBRANES: TRANSPORT PROPERTIES
AND REPLICATION

By

DAMIAN J. ODOM

A DISSERTATION PRESENTED TO THE GRADUATE SCHOOL
OF THE UNIVERSITY OF FLORIDA IN PARTIAL FULFILLMENT
OF THE REQUIREMENTS FOR THE DEGREE OF
DOCTOR OF PHILOSOPHY

UNIVERSITY OF FLORIDA

2005

Copyright 2005

by

Damian J. Odom

To my family, for their continued love and support.

ACKNOWLEDGMENTS

Many individuals have influenced and advised me professionally and personally over the years. Their help, guidance and support have enabled me to write this Ph.D. dissertation. First, I would like to thank Dr. Edward Healy, my analytical and inorganic chemistry professor at the University of North Florida. He showed me how to look ahead into my professional career and to make plans (while remaining flexible) for getting there. He, as well as many others, inspired and *pushed* me on to graduate school.

I would like to thank previous advisor, Professor Laurie Gower, whom I studied under and earned my MS degree in Material's Science & Engineering. Those few years had led to many memories and on going friendships. Surprisingly, today in analytical chemistry I am using many of the concepts and skills I learned then.

I would like to thank my current advisor (Professor Charles R. Martin) for his assistance, ample advice, endless support, and the opportunity to work toward my PhD. I have met many friends here, and have had many positive experiences in his group, all while learning how to work more independently and assertively.

With time any good group brings contact with many good post-docs. Because of their immense influence on my early development in my graduate career, I would like to thank Sang Bok Lee, Marc Wirtz, and Punit Kohli for many late-night discussions about research, science and life in general. They showed great professionalism and leadership during their time in this group. Many graduate students I have met, have made the learning process a lot more fun: David Mitchell, Scott Miller, Shufang Yu, Naichoa Li,

Chad Harrell, Elizabeth Heins, Liisa Kauri, Lacramiaora Trofin, John Wharton, Fatih, and Robbie Sides. I would also like to thank Elizabeth Heins, Shufang Yu, Robbie Sides and Charley Malpass for reviewing this manuscript. This is to name a few, but so many people have been positive influences and friends over the years.

For their support and undying love over the many years, I would like to thank my parents, Soloman and Bobbie Odom. They have showed great patience and wisdom as parents and as my friends. Without their teachings and lessons I would not have been prepared for the journey of life. I would also like to thank my extended family members. They have all raised me and guided me as their son or brother as I have gone through life.

Finally, I would like to thank my soon-to-be wife, Nicole Gordon. She has endured a lot, as I have tried to complete this degree and spent many anguished ours editing this body of work. Most important, she has shown me there is more to life than just a lab and science.

TABLE OF CONTENTS

	<u>Page</u>
ACKNOWLEDGMENTS.....	.iv
LIST OF TABLES.....	viii
LIST OF FIGURES.....	ix
ABSTRACT.....	xiii
CHAPTER	
1 INTRODUCTION AND BACKGROUND.....	1
Track-etched and Nanoporous Anodic Alumina Membranes.....	2
Track-Etch Membranes.....	2
Nanoporous Anodic Alumina Membranes.....	5
Separations Based on Porous Membranes.....	8
Silane Modification.....	12
Langmuir Adsorption Isotherm.....	13
Scanning Electron Microscopy.....	16
Electroless and Electrochemical Deposition.....	21
Electroless Deposition.....	21
Electrochemical Deposition.....	24
Dissertation Overview.....	25
2 TRANSPORT RATE AND SELECTIVITY IN SILANE MODIFIED NANOPORE ALUMINA MEMBRANES.....	27
Introduction.....	27
Experimental.....	28
Membrane Modification.....	29
Transport Experiments.....	29
Results and discussion.....	32
Transport of Ni ²⁺ and 2,4-Dimethylphenol through Untreated Versus Octadecyltrimethoxy-Treated Membranes.....	32
Transport of a Homologous Series of Hydrophobic Permeate Molecules.....	35
Rate and Selectivity of Transport with our Supported Liquid	

Membranes.....	52
Conclusions.....	57
3 TRANSPORT RATE AND SELECTIVITY WITH SELECT SILANES FOR THE SURFACE MODIFICATION OF NANOPORE ANODIC ALUMINA MEMBRANES.....	59
Introduction.....	59
Experimental.....	59
Results and discussion.....	61
Transport with DiPS and DiPKS Modified Membranes.....	61
Transport with CF ₃ S Modified Membranes.....	68
Conclusions.....	74
4 TRANSPORT RATE AND SELECTIVITY IN SILANE MODIFIED NANOPORE ANODIC ALUMINA MEMBRANES AND PH DEPENDANCE.....	76
Introduction.....	76
Experimental.....	79
Results and discussion.....	80
PH Dependant Transport Utilizing ODS Modified Membranes.....	80
Solution pH Based Concentration and Separation of 2-Nitrophenol and Pyridine Based on Solution pH.....	90
Competitive Separation Studies.....	92
Conclusions.....	95
5 PRODUCTION OF POLYMERIC REPLICA MEMBRANES OF TRACK-ETCH AND NANOPOROUS ANODIC ALUMINA MEMBRANES.....	97
Introduction.....	97
Experimental.....	99
Results and discussion.....	103
Selection Mold Material.....	103
Complete Mold Method Applied to Track-Etched Membranes.....	111
Complete Mold Method Applied to Nanoporous Anodic Alumina Membranes.....	115
The <i>Incomplete</i> Mold Method.....	118
Conclusions.....	123
6 CONCLUSIONS.....	125
7 LIST OF REFERENCES.....	130
8 BIOGRAPHICAL SKETCH.....	140

LIST OF TABLES

<u>Table</u>		<u>page</u>
1-1	Selected solutions for electroless deposition.....	23
2-1	Calculated selectivities for ODS-treated BP20 and CP200 membranes.....	39
2-2.	Contact angle measurements of phenol solutions on an ODS-treated BP20 membrane.....	44
2-3.	Calculated partition coefficients and selectivities based on bulk solution extractions.....	48
2-4.	Calculated selectivities for ODS-treated BP20 membranes, with kerosene and mineral oils subphases.....	54
2-5.	Calculated transport rates for phenol and TMP into and out of bulk phases of kerosene and mineral oil.....	56
3-1.	Fluxes for DiPS and DiPKS-treated BP20 membranes with and without the presence of a subphase (2mM feed concentrations).....	59
3-2.	Fluxes for an CF ₃ S-treated BP20 membrane and 2mM feed concentrations.....	69
3-3.	Contact angle measurements of p-cresol and aniline on ODS and CF ₃ S-treated 20BP membranes.....	71

LIST OF FIGURES

<u>Figure</u>	<u>page</u>
1-1 The commercial track-etching process.....	3
1-2 Scanning electron micrographs of commercial polycarbonate track-etch membranes.....	4
1-3 Electrochemical production of a nanoporous anodic alumina membrane.....	6
1-4 SEM micrographs of commercial and in-house nanoporous anodic alumina membranes.....	8
1-5 Principle membrane transport mechanisms.....	11
1-6 Steps of surface silanization process.....	13
1-7 Diagram of a scanning electron microscope (SEM).....	19
1-8 Electron beam-to-sample interactions.....	19
2-1 U-tube permeation cell set-up.....	30
2-2...Membrane assembly without a subphase.....	31
2-3 Transport of Ni ²⁺ A), and 2,4-dimethylphenol (DMP) B with CP200 membrane (○) and octadecyltrimethoxysilane (ODS) treated CP200 membrane (□).....	34
2-4 Vapor and silane layer diffusions mechanisms.....	35
2-5 Homologous series of permeate molecules and their respective structures.....	37
2-6 Flux plots for ODS-treated A) BP20 and b) CP200 membranes with a 2 mM feed solution.....	38
2-7 Flux of phenol vs. phenol feed concentration for an ODS-treated BP20 membrane.....	42

2-8A Bulk solvent partition data for A) phenol and B) p-cresol used to determine partition coefficients.....	46
2-8B Bulk solvent partition data for A) DMP and B) TMP used to determine partition coefficients.....	47
2-9 Flux of phenol vs. phenol feed concentration for an ODS-treated BP20 membrane containing kerosene.....	49
2-10 Flux of phenol vs. phenol feed concentration for an ODS-treated BP20 membrane containing mineral oil.....	50
2-11 Plots for BP20 ODS-treated membranes with a A) kerosene, and B) mineral oil subphase with a 2 m <u>M</u> analyte feed solution.....	53
2-12 U-tube permeation cell set-up with organic solvent.....	55
3-1 Silanes used for anodic alumina membrane modification.....	61
3-2 Transport with DiPS and DiPKS-treated membranes.....	63
3-3 Transport with DiPS and DiPKS-treated membranes with a kerosene Subphase.....	64
3-4 Transport with DiPS and DiPKS-treated BP20 membranes with a mineral oil subphase.....	65
3-5 Transport with a CF ₃ S-treated BP20 membrane with increasing concentrations of analyte.....	68
3-6 Flux versus increasing feed concentrations of phenol with a CF ₃ S-treated BP20 membrane.....	70
3-7 Flux of p-cresol and aniline with ODS and CF ₃ S-treated membranes.....	73
4-1 Structures and pK _a values for A) aniline, B) 2-nitrophenol, C) benzoic acid and D) pyridine.....	77
4-2 Calculated A) alpha values, and B) the expected flux trend for aniline based on a pK _a of 4.6.....	79
4-3 Calculated alpha and measured flux versus feed pH for A) 2-nitrophenol and B) pyridine.....	82
4-4 Calculated alpha and measured flux versus feed pH for A) benzoic acid and B) aniline.....	83

4-5	Log(Flux) versus feed solution pH using a BP20 membrane with A) 2-nitrophenol and B) pyridine.....	85
4-6	Log(Flux) versus feed solution pH using a BP20 membrane A) benzoic acid and B) aniline.....	86
4-7	Linear relationship between expected flux and neutral species concentration.....	87
4-8	Correlation of the calculated concentration (based on calculated alpha) and the experimental flux at a given pH for A) 2-nitrophenol, and B) pyridine.....	88
4-9	Correlation of the calculated concentration (based on calculated alpha) and the experimental flux at a given pH for A) benzoic acid, and B) aniline.....	89
4-10	Percent change in the concentration of 2-nitrophenol in the feed and permeate versus time using a BP20 membrane.....	91
4-11	Separation of 2-nitrophenol and pyridine using a BP20 membrane.....	92
4-12	Separation of 2-nitrophenol and pyridine using a BP20 membrane with a kerosene subphase.....	93
4-13	Separation of 2-nitrophenol and pyridine using a BP20 membrane with a mineral oil subphase.....	94
5-1	Membrane replication methods.....	104
5-2	Surface SEM micrographs of PE4000 mold of CP200 membrane.....	105
5-3	SEM micrographs of a fracture surface of CP200 membrane molded with PS250000.....	106
5-4	SEM micrographs of a fracture surface of CP200 membrane molded with PS250000 after the dissolution of the membrane.....	107
5-5	SEM micrographs of the cross-section of CP200 membrane with electrolessly deposited nickel metal. Deposition with NiSI solution for 3 days.....	108
5-6	SEM micrographs of the cross-section of CP200 membrane with electrolessly deposited nickel metal. Deposition with the NiSII solution for 3 days.....	109

5-7	SEM micrographs of a CP200 membrane during various stages of the <i>complete</i> molding technique.....	110
5-8	SEM micrographs of <i>complete</i> molds deposited around track-etch membranes with different pores diameters.....	111
5-9	SEM micrographs of <i>incomplete</i> nickel molds of a $1.2\mu\text{m}$ polycarbonate track-etch membrane after removal of the membrane.....	112
5-10	SEM micrographs of produced polymeric replicas (polyethylene $M_w=15000$) from track-etch polycarbonate membranes.....	113
5-11	SEM micrographs of produced polymeric replicas (polystyrene $M_w=250000$) from $10\mu\text{m}$ track-etched polycarbonate membrane templates.....	114
5-12	Mold formed around a track-eth membrane versus from a nanoporous anodic alumina membrane.....	115
5-13	SEM micrographs of a nickel mold of a CP200 membrane produced via the <i>complete</i> mold method after chemical dissolution of the membrane.....	116
5-14	SEM micrographs of PE15000 replica produced from a CP200 membrane using the <i>complete</i> mold method.....	117
5-15	Schematics of the a mold produced via the <i>incomplete</i> mold method after removal of the membrane.....	120
5-16	SEM micrographs of an <i>incomplete</i> mold fabricated from a CP200 membrane.....	121
5-17	SEM micrographs of PE15000 and PS250000 replicas using the <i>incomplete</i> mold method.....	122

Abstract of Dissertation Presented to the Graduate School
of the University of Florida in Partial Fulfillment of the
Requirements for the Degree of Doctor of Philosophy

NANOPOROUS ANODIC ALUMINA MEMBRANES: TRANSPORT PROPERTIES
AND REPLICATION

By

Damian J. Odom

May 2005

Chair: Charles R. Martin

Major Department: Chemistry

Technology based on synthetic nanopore membranes is a burgeoning field, stretching into many branches of science. Nanopore membranes are used to decontaminate volatile organics from soils, for nanofiltrations, for separating and extracting metals, and as templates for materials science and engineering. The Martin group has had a longstanding interest in cylindrical nanopore membranes (more specifically, nanopore plastics made by the track-etch method), and in nanopore anodic alumina membranes made by anodic oxidation of aluminum metal.

The surfaces of nanopore anodic alumina can be chemically functionalized using well-known silane-coupling chemistry. We were interested in learning how modification with silanes possessing different alkyl groups would affect the transport rate and selectivity in nanopore anodic alumina membranes.

Four different substitutive alkyl groups were selected: a C₁₈, a diphenyl silane, an 8-hydroxyquinoline-like group, and an 8-carbon long fluorinated chain. These silane-treated membranes were also used to support a bulk organic solvent (kerosene or mineral oil) subphase within the pores. The flux of permeate molecules was measured, using a u-tube permeation cell (with the membranes of interest dividing each half). A homologous series of permeate molecules was selected for transport (phenol, p-cresol, 2,4-dimethylphenol, and 2,4,6-trimethylphenol).

The C₁₈ and fluorinated silanes prevented the pores of the membrane from flooding. Despite the pores remaining filled with air, the permeate molecules were still able to traverse the modified membranes, while rejecting a charged species (Ni⁺²). Membranes modified with the C₁₈ and fluorinated silanes also expressed a *Langmurian Adsorption Isotherm*-like property, when the flux was plotted versus increasing feed concentrations of phenol. The Langmuir adsorption equation could be successfully fit to these data ($R^2 > 0.99$) and the adsorption constant (KL) solved for.

Nanopore anodic alumina membranes inherently suffer from brittle fracture. Great strides were made in deriving a method for producing a more robust plastic replica of these membranes. Several methods were explored, using melt injection of polymers, or electroless or electrochemical deposition. The most successful method was the electrochemical deposition of nickel to form a mold around the original membrane. After mold formation, the membrane was replaced with a plastic material.

CHAPTER 1

INTRODUCTION AND BACKGROUND

Technology based on synthetic nanoporous membranes is a burgeoning field that reaches into many branches of science. Some uses of these nanoporous membranes are the removal of volatile organics from soils¹ and effluent streams,^{2,3,4,5} the extraction of high boiling point organics,^{6,7,8,9} nanofiltration,^{10,11,12} the separation and extraction of metals,^{13,14,15,16} as substrates for biosensors,¹⁷ and as templates for materials science and engineering.^{18,19,20} There are three principal families of synthetic nanoporous membranes: isotropic (organic and inorganic), track-etch, and nanoporous anodic alumina membranes.

The studies presented here are based on the track-etch organic and nanoporous anodic alumina membrane families. The first set of studies addressed membrane transport and selectivity, as well as the tailoring of these properties through surface modification. The second set of studies delved into the field of materials science. These studies explored the production of polymeric replicas of nanoporous anodic alumina membranes.

The remainder of this chapter is divided into six sections, each providing pertinent background information for this research. Section 1 reviews the fabrication and uses of track-etch and nanoporous anodic alumina membranes. Section 2 gives an overview of separation based on nanoporous membranes and some of the previous work done in the Martin group. Section 3 presents the basics of scanning electron microscopy (SEM)

which is used extensively in Chapter 5. Section 4 introduces and shows the derivation of the Langmuir adsorption isotherm, which is used to fit data in Chapters 2 and 3.

Electroless and electrochemical deposition methods and techniques are introduced in section 5. These deposition methods are the foundation for the replication methods developed in Chapter 5. Section 6 of this chapter is an overview of the entire dissertation.

Track-Etch and Nanoporous Anodic Alumina Membranes

Track-Etch Membranes

The concept of track-etch membranes evolved from the field of solid-state nuclear track detectors. The nuclear track detector field itself was born in 1958^{21,22} when D.A. Young discovered and described the first tracks in a crystal of LiF irradiated with an uranium foil.²³ Aided by the advancement of electron microscopy this field has blossomed²⁴ and several in-depth texts have been published.^{21,25,26,27} Solid-state nuclear track detectors are beyond the scope of this paper; however, the field of track-etch membrane based separations relies on an understanding of track formation and etching, so those concepts will be discussed.

Figure 1-1 shows a schematic of the two-step commercial track-etching process.²⁸ The process begins with the selection of a membrane to be tracked, polycarbonate and polyester are two typical commercial materials used today.²⁸ A plastic film is fed past a beam of high-energy particles, inducing the formation of tracks. The source of these high-energy particles is either a nuclear reactor^{21,25,29} (e.g. fragments from the fission of californium or uranium) or a heavy ion accelerator (e.g. Kr, Ar, Xe or S) operating in the

10 MeV/u range.^{21,25,30} As each high-energy particle passes through the membrane it leaves a damage pathway called a track.

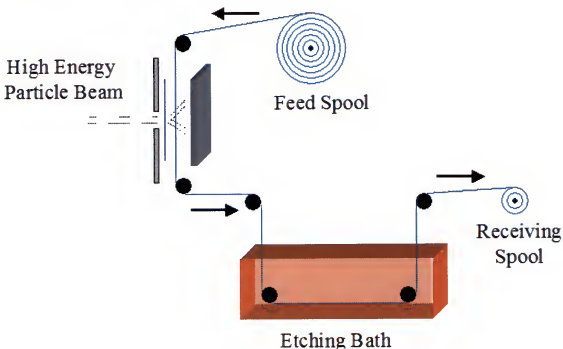


Figure 1-1. The commercial track-etching process.

Tracks, also called latent tracks,²² usual distinguishing characteristics are damage pathways of bond scission and ionization.^{21,25} The stability and lifetime of these generated tracks depend on the material in which they are formed. It turns out tracks in minerals and glass have longer resident lifetimes than tracks in plastics. This is because tracks in minerals are less susceptible to environmental factors, such as temperature, pressure, shock, humidity, and ionization.^{21,25}

The most important property of formed tracks to the field of nanoporous materials is their susceptibility to chemical attack. By exposing a tracked membrane to an appropriate etching solution (e.g. sodium hydroxide for polycarbonate), preferential etching of the material will create a pore where a track was previously located.^{21,25,29,30}

This process is predictable and can be well controlled; more specifically, the longer the exposure time to the etching solution, the larger the diameter of the pores etched.

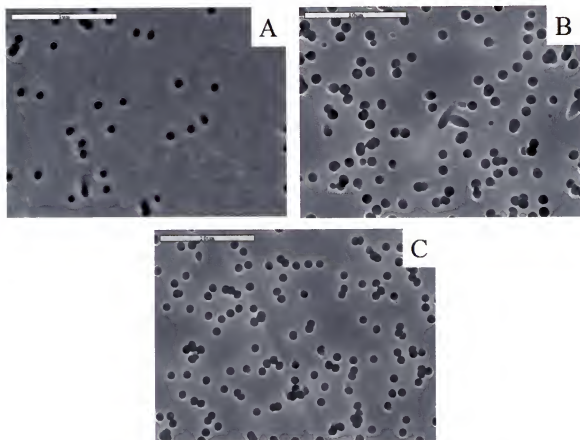


Figure 1-2. Scanning electron micrographs of commercial polycarbonate track-etch membranes. Membrane with A) 50 nm, B) 1 μ m, and C) 1.2 μ m diameter pores (Scale bars are 1 μ m, 10 μ m and 10 μ m respectively).

Examples of many-pored polycarbonate track-etch membranes are shown in the scanning electron micrographs in Figure 1-2. Typically, when the membrane is exposed to a high-energy particle beam, a thin metal foil is used to scatter this beam, resulting in a random placement of the tracks on the membrane. In commercial polycarbonate track-etch membranes, the pores have an incident angle (to the surface of the membrane) of 30° to 35°.²¹ These pores are distinct in the micrographs and are seen as non-circular pores. Today, membranes with many different pore diameters are commercially available,

ranging from 10 nm to 10 μm , with a thickness between 6 to 14 μm , and a porosity of less than 8%.³¹

Nanoporous Anodic Alumina Membranes

The surface oxidation of aluminum has been studied for years because of its large-scale commercial use.³² In 1974, the first patent for the production of nanoporous anodic alumina membranes based on electrochemical reduction of aluminum was issued.³³ Since the issuance of that patent, there has been a large body of research focused on understanding the mechanisms of porous alumina formation by the electrochemical reduction of aluminum metal.^{34,35,36,37,38,39} Today, nanoporous anodic alumina membranes with different pore diameters and thickness are routinely manufactured for both commercial and academic use. A general schematic for the production process of a nanoporous anodic alumina membrane is presented in Figure 1-3.

When aluminum metal is anodized, two types of surface aluminum oxide can be produced.^{32,40,41} If anodization is performed at a pH greater than 5, then an insulating film forms. However, in more acidic electrolytes, a film with pores open to the surface is formed. When the second type of porous aluminum oxide film (nanoporous anodic alumina) is desired, an aluminum foil of high purity is used. This foil, (typically with a purity greater than 99.99%) is annealed at 400°C for at least one hour, followed by electropolishing, most commonly in a perchloric acid:ethanol solution. Electropolishing has been shown that it can reduce the mean surface roughness of the foil to 3 nm over a 3 μm square area.^{42,43} The polished aluminum foil is then anodized in a dilute acidic electrolyte (oxalic, phosphoric or sulfuric acid) at electrolyte temperatures below ~10°C. After termination of anodization, the non-anodized aluminum can be removed by a

galvanic process using salt solutions of Hg(II) or Cu(II). Finally, the closed ends of the pores, which were adjacent to the aluminum metal, are opened using a treatment of a dilute phosphoric acid solution.^{35,42,43,44,45,46,47,48,49,50,51,52}

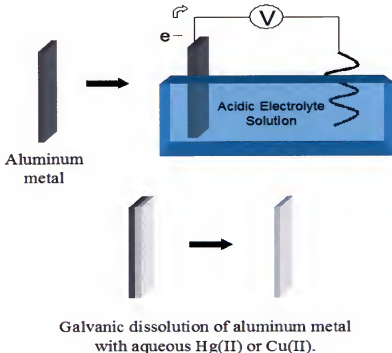


Figure 1-3. Electrochemical production of a nanoporous anodic alumina membrane.

Researchers that have been studying the formation process of this porous material have agreed upon three important observations. First, the longer the anodizing step, the more ordered the pores become and thicker the alumina membrane. Second, the greater the anodizing voltage used, the larger the resultant pore diameters. Third, by carefully applying the observations above, membranes with desired thicknesses and pore diameters (which are highly ordered) can be produced. A skilled practitioner can produce nanoporous anodic alumina membranes with pore diameters of 10 to 250 nm, porosities as high as 50% (a pore density of 1×10^8 to 1×10^{10} per cm^2), low tortuosity and pore size distribution, high pore orientation, and thicknesses from a few nanometers to over 300

μm. Figure 1-4 shows SEM micrographs of commercial alumina and alumina prepared in-house.

Besides the standard anodization process described above, other more creative methods for the fabrication of nanoporous anodic alumina membranes have been derived. It has been shown a nanoindentor can be used to place indentations into the surface of the aluminum metal, where the indentations act as initiation sites for pore formation during anodization.^{53,54} Using this nanoindentation method, pores can be promoted to grow in rows,⁵⁵ and in the shapes of squares or triangles⁵⁶ instead of the usually hexagonal pattern of cylindrical pores.

Asymmetric pores (pores with one end larger than the other) are obtainable via two methods. The first method is to vary the anodizing voltage during the growth of the membrane.⁵⁷ This yields larger pores at the higher anodizing voltage side which branch into the smaller pores at the lower anodizing voltage side. The second method is to change the anodizing electrolyte during the growth process.⁵⁸ Anodization is performed for a given time in one electrolyte solution, which is exchanged for a second electrolyte solution for further anodization. The membrane is then exposed to a mild etching solution. Done in this manner, the areas of the membrane anodized in differing electrolytes will etch at differing rates, producing membrane pores with two different pore diameter regions.

Finally, one study showed how a hollow cylindrical aluminum tube could be anodized to produce a nanoporous anodic alumina membrane in the shape of a hollow cylindrical tube.^{59,60} After its fabrication the cylindrical membrane could be fashioned into a flow-through chamber for filtration experiments.

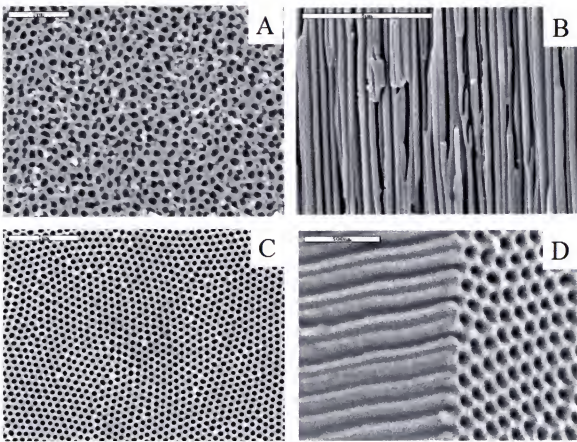


Figure 1-4. SEM micrographs of commercial and in-house nanoporous anodic alumina membranes. A) and B) are a 200 nm pore diameter commercial alumina membrane. C) and D) are an in-house alumina membrane. (Scale bars are 2 μm , 5 μm , 1 μm , and 500 nm respectively. In-house alumina membrane produced by Lacramioara Trofin. SEM images C) and D) courtesy of Elizabeth Heins.)

Separations Based on Porous Membranes

Chapters 2 through 4 utilize nanoporous anodic alumina membranes as platforms for membrane based separations. Here we give a brief look at separations based on porous membranes.

Over the last 30 years, membrane based separation processes have steadily increased in their use, slowly replacing conventional industrial techniques such as distillation, crystallization and solvent extraction.^{61,62,63} Porous membranes can be thought of as selective barriers or interfaces separating two phases, whose lateral

dimensions are much greater than its thickness, and through which mass transfer may occur under a variety of driving forces in a rather specific manner.^{61,62,64} In an attempt to classify membranes, they are often grouped according to their structure: homogeneous (symmetric, isotropic), heterogeneous (asymmetric, anisotropic), or a composite membrane.^{61,62,63} Membranes can also be classified according to their separation regime and application: microfiltration, ultrafiltration, nanofiltration, and reverse osmosis.^{61,62,63}

Separation membranes can be manufactured by many methods, such as: the extrusion of films, casting of solutions, pressing and sintering of powders, stretching of extruded polymer sheets, and phase inversion.⁶¹ The manufacture of the two principle membranes of interest here (track-etch and nanoporous anodic alumina) was previously in detail. The fundamental concepts of transport based on passage through porous membranes will now be discussed.

There are three main transport processes in membranes, passive transport, facilitated transport, and active transport.^{61,62,63} Figure 1-5 illustrates each case, where the analyte concentration is depicted versus respective position to the membrane. In passive transport, the membrane merely behaves like a physical barrier, through which the transport of species is governed by a gradient based driving force. A few examples of possible driving force gradients are temperature,⁶² concentration,^{65,66,67} pressure,⁶⁸ and potential.⁶⁹

For a passive transport processes, the average driving force (F_{ave}) can be described by Equation 1-1,

$$F_{ave} = \Delta X / \Delta x \quad (1-1)$$

where $\Delta X/\Delta x$ equals the gradient of X along the perpendicular coordinate x-axis. When there is a constant driving force, transport through the membrane establishes a steady state,⁶² for which a proportionality relationship between the flux (J) and the driving force (X) can be written as Equation 1-2,

$$\text{Flux}(J) = \text{proportionality_factor}(A) * \text{driving_force}(\Delta X / \Delta x) \quad (1-2)$$

where A is a phenomenological coefficient relating flux and force. One such linear relationship is Fick's law (Equation 1-3),

$$J = -D \left(\frac{\Delta C}{\Delta x} \right) \quad (1-3)$$

where ΔC represents a variation in concentration, Δx equals the distance covered by the variation in concentration, and D is a phenomenological coefficient for diffusion. Fick's law is an equation describing mass flux; other forms of flux are volume (Darcy's law), heat flux (Fourier's law), momentum flux (Newton's law), and electrical flux (Ohm's law).

Facilitated transport is a special case of passive transport because it involves a carrier species that can undergo a binding and release step with the analyte being transported.⁶² As in the case of normal passive transport, the rate of transport through the membrane depends on a gradient across the membrane. However, in this case, transport is promoted according to the interaction of each species with the carrier.^{61,62,63} A classic example of this type of membrane is a supported liquid membrane (SLM). These are membranes often filled with a hydrophobic solvent and doped with a chelator designed to bind a particular species.^{70,71,72} Without the chelator the analyte would be unable to traverse the membrane; however, the chelator enables the passage of the analyte through the membrane based on binding, transport and release events.

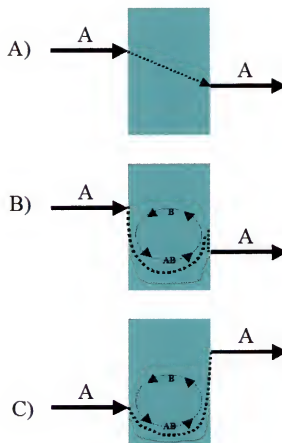


Figure 1-5. Principle membrane transport mechanisms: A) passive transport, B) facilitated transport, and C) active transport.

Passive transport and facilitated transport are considered *downhill* transport, which is transport *with* the concentration gradient. In the case of the third principle transport process, active transport, the transport of analyte is *against* the concentration gradient, or *uphill*. Active transport of a molecule is unique because it is accompanied by the consumption of energy. The most intricate and successful examples are found in the membranes of living cells.⁶¹ One example is the active transport of Na^+ and K^+ ions across the cell membrane by Na,K -ATPase (an enzyme) accompanied by the consumption of ATP.⁶³ As one can imagine, the equations governing each transport process becomes considerably more involved with each mentioned case.

We studied the passive transport of alkyl species with silane-treated nanoporous anodic alumina membranes is reported in Chapters 2, 3 and 4. It was shown the transport rates are solely dependant on the analyte feed concentration and the hydrophilic/hydrophobic affinity of the analyte for the membrane.

Silane Modification

Silane modification is the dominant surface modification method used in these studies. The basic concepts and fundamentals will now be introduced to the reader.

Alkoxy silanes [$R_1\text{-Si(OR}_2)_3$] are common and generally convenient reagents for the modification of a substrate.⁷³ The final chemical identity of the surface that results from reacting an organosilane with a substrate typically depends on the organic group (R_1) being anchored to the substrate. Substrate properties such as wetting, adhesion, catalytic response, or partitioning may be affected to a varying degree.⁷³ Silane treatment of a substrate from an aqueous alcohol (the method used here) tends to be the most amiable method, using a solution of ~95% ethanol and ~5% water, adjusted to a pH of 4.5 to 5.5 with acetic acid.

Silane treatment of a responsive surface has been reported to involve four steps: 1) hydrolysis, 2) condensation, 3) hydrogen bonding, and 4) bond formation (Figure 1-6).

⁷³ Bond formation can be promoted by heating the treated substrate at ~110° for a short period or simply allowing it to occur naturally by letting the sample sit at room temperature for at least 24 hours.

Silane treatment of substrates has found many scientific uses such as: providing bonded phases for gas and liquid chromatography,^{73,74,75} orienting crystals in liquid displays,⁷³ forming photochemical sensitive self-assembled monolayers,⁷⁶ acting as an

alkaline corrosion inhibitor for aluminum,⁷⁷ being a source for silicon carbide in electron cyclotron resonance CVD,⁷⁸ forming self-assembled monolayers that can be easily modified to hydroxyls,⁷⁹ and creating a highly efficient metal scavenger self-assembled layer.⁸⁰

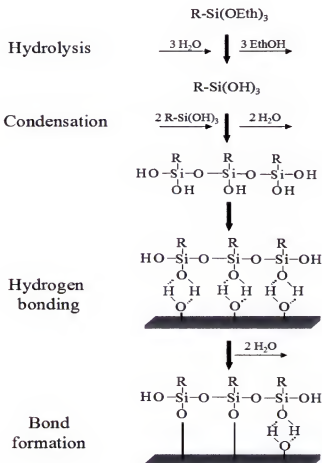


Figure 1-6. Steps of surface silanization process.

Langmuir Adsorption Isotherm

The Langmuir adsorption equilibrium isotherm is used to fit data in Chapters 2 and 3. This equation relates the number of adsorption sites occupied (by an analyte) on a surface to the concentration of the bulk analyte, the affinity of the analyte for the surface, and the temperature.

In 1916, Irving Langmuir derived an equilibrium equation for the fraction of a solid surface covered by an adsorbing species as a function of gas pressure.⁸¹ The derivation was as follows. For a molecule in the gaseous phase, A , which can bind to a site on a surface, S , an equilibrium expression can be written,



where SA represents an analyte occupied surface site. An equilibrium expression can be written for this adsorption process in terms of a constant K ,

$$K = \frac{[SA]}{[S][A]} \quad (1-5)$$

The analyte concentration is represented by $[A]$, the concentration of vacant sites is $[S]$ and the concentration of occupied sites is $[SA]$. A new value, θ , can be defined as the fraction of sites occupied at a given time,

$$\theta = \frac{SA}{S_{\max}} \quad (1-6)$$

where S_{\max} equals the total number of surface sites that can be occupied. Using the following proportionality expressions and resultant definitions a new equilibrium constant, b , can be defined.

$[SA] \propto$ to surface coverage of adsorbed molecules, therefore let $[SA] = \theta$

$[S] \propto$ to the number of vacant sites, therefore let $[S] = (1-\theta)$

$[A] \propto$ to the pressure of the analyte gas, P , therefore let $[A] = P$

Substituting the above definitions into Equation 1-5 gives Equation 1-7,

$$b = \frac{\theta}{(1-\theta)P} \quad (1-7)$$

Rearranging Equation 1-7 and solving for θ , we obtain Equation 1-8,

$$\theta = \frac{bP}{(1+bP)} \quad (1-8)$$

Equation 1-8 is a common form of the Langmuir adsorption equation and, after substituting Equation 1-6 into Equation 1-8 we obtain the second.

$$SA = \frac{S_{\max} bP}{1 + bP} \quad (1-9)$$

Equation 1-9 is the equilibrium expression for adsorption of a gaseous species on a solid interface. When the Langmuir adsorption equation is expressed for the adsorption of an analyte from dilute liquid onto a solid substrate it takes the form of Equation 1-10,

$$[X] = \frac{C_{\max} K_L [X_{aq}]}{1 + K_L [X_{aq}]} \quad (1-10)$$

where C_{\max} is the saturation concentration of X in the layer (mmol/g), K_L is the Langmuir adsorption constant (mM^{-1}), $[X]$ is the concentration of X in the adsorbing layer and $[X_{aq}]$ is the concentration of X in the solution (mM).^{82,83,84}

Certain assumptions must be fulfilled for the application of the Langmuir adsorption isotherm: 1) each surface site can be occupied by one analyte, 2) there are no lateral interactions between the adsorbed species, 3) the enthalpy of adsorption is independent of the magnitude of θ , and 4) there is dynamic equilibrium between the adsorption and desorption process.^{85,86,87,88} In essence, the surface is assumed to be a simple homogeneous substrate with discrete adsorption sites. Although most surfaces are known to be heterogeneous, the Langmuirian adsorption isotherm can still be used if a high R^2 -value is obtained when data is fitted to the linear expression. The linear form of this equation is derived by taking the reciprocal of Equation 1-10.

$$\frac{1}{[X]} = \frac{1}{C_{\max} K_L [X_{aq}]} + \frac{1}{C_{\max}} \quad (1-11)$$

The Langmuir adsorption isotherm has been used to model the adsorption of aqueous dyes,^{83,84,89,90} metal pollutants,^{82,91,92,93,94} hydrophobic analytes of the benzene family,⁹⁵ and band profiles in gradient elution chromatography.^{96,97}

The Langmuir isotherm assumes adsorption of an analyte at finite homogeneous sites in a monolayer.^{89,82} For cases that do not fulfill the assumptions of the Langmuir equation, other isotherms have been derived. In 1906, Freundlich presented the earliest documented equation for adsorption.⁹⁵ His equation related adsorption on non-ideal heterogeneous surfaces,⁹⁵ where his constants related the level of sorption and extent of nonlinearity between the solution concentration and adsorption.^{84,89} Other isotherms are the Redlich-Peterson equation (a hybrid of the Langmuir and Freundlich),^{89,95} Henry's law (for mobile films involving 2D ideal gases), Volmer's equation (for a mobile film involving hard sphere particles), Hill-de Boer equation (for mobile films with van der Waals gas interactions), Fowler's equation (for localized films with interactions), and the virial equation (for mobile films with non-ideal gases and interactions).⁹⁸

Scanning Electron Microscopy

Scanning electron microscopy (SEM) is an electron beam based imaging and analysis technique. SEM is used extensively in Chapter 5 for method development and, because of its extensive use, a summary of this technique will now be given.

Scanning electron microscopy (SEM) is typically turned to when the resolutions desired by an investigator can not be achieved with an optical microscope. The benefits of the SEM can be seen by looking at Abbe's equation, which relates the resolution d to the wavelength of the probing light λ ,

$$d = \frac{0.612\lambda}{n \sin \alpha} \quad (1-4)$$

where n is the index of refraction and α is the aperture angle. To see the benefits in resolution the shortest wavelength of visible light (blue light, $\lambda = 400$ nm) should be compared to typical operating conditions for an SEM (60 KeV, where λ of the probing electrons = 0.005 nm). This difference in incident beam wavelength produces an almost 5 order of magnitude advantage for an SEM over the optical microscope.

To the everyday scanning electron microscopist, the two most interesting analytical signals are secondary electrons (SE) and backscattered electrons (BSE).⁹⁹ Secondary electrons are emitted from the sample's surface near the point of electron beam impact and are quite useful for providing sample topographical information. Under the proper conditions SE can be used to generate very high-resolution images. Commercial instruments report SE resolutions in the range of 2 to 5 nm while research instrumentation has achieved resolutions as high as 1 nm.⁹⁹ Backscattered electrons are emitted from a larger volume within the sample and can be used to provide compositional information. Because of the larger volume of emission of BSE, the resolution of images generated are several nanometers greater than with SE.

The history and development of the modern day SEM shares some technological advancements with the transmission electron microscope (TEM). The SEM's history began in 1935, with its conceptual description first being presented in Germany by Knoll and coworkers.¹⁰⁰ In 1938, von Ardenne^{101,102} was the first to add scanning coils to a transmission electron microscope. Ardenne and coworkers also discussed the general theoretical and practical aspects of a scanning microscope. This prior groundwork led to the first recognizable modern day SEM used for the examination of a thick specimen in 1942 by Zworykin et. al.¹⁰³ whom worked at the RCA Laboratories in the US.¹⁰⁴ In

1963, Pease built a SEM system, which later became the prototype for the first commercial instrument from Cambridge, manufactured in 1965.^{99,104} Today, thousands of SEMs are available in many different shapes, sizes, and capabilities from over a dozen manufacturers.

The inner workings of a SEM are conceptually simple (Figure 1-7). An electron emitter is placed at the top of a vacuumed column. The electron beam is guided down the column by electromagnetic lenses and focused onto the sample of interest. The last lens (the objective lens) contains scanning coils, which enables the beam to be rastered across the surface of the sample. Finally, an appropriate detector is placed nearby to collect the analytical signals of interest that are emitted from the sample's surface.^{99,104}

Once the electron beam strikes the sample and penetrates beneath its surface, analytical signals are produced by several beam-to-sample interactions. These interactions are very complex and have been extensively modeled by Monte Carlo Electron-Trajectory Simulation over the years.^{105,106,107,108,109,110} Several useful analytical signals are generated from these interactions, such as SE, BSE, Auger electrons, characteristic x-rays, and cathodoluminescence. Details of these interactions are beyond the scope of this work; however, the signals relevant to this work will be discussed more thoroughly.

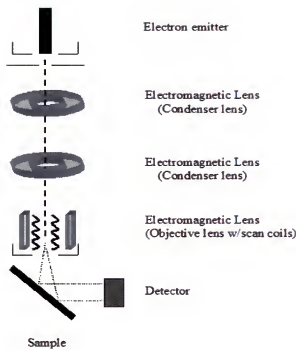


Figure 1-7. Diagram of a scanning electron microscope (SEM).¹⁰⁴

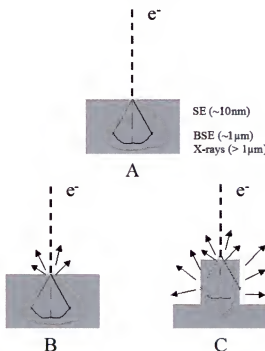


Figure 1-8. Electron beam-to-sample interactions. A) Emission depths of differing signals, B) secondary electron (SE) emission from a flat sample, and C) SE emission from a raised sample locale.

The two principle signals used in Chapter 5 are secondary electrons and characteristic x-rays. Secondary electrons are low energy electrons (<50eV) emitted during the scattering events from within a few nanometers of the sample's surface all within a close proximity to the impinging electron beam. These signals are most advantageous and are best utilized for imaging sample topography and morphology.

Looking at Figure 1-8, we can begin to understand how an SEM image is generated. The expected signal generations from a flat section of the sample and a raised area are depicted in Figure 1-8B and C. As the electron beam is scanned across the sample's surface, SE emission intensity fluctuates in accordance with the sample's topography. These fluctuating intensities are recorded versus the beam scan location. If the intensities are converted into a gray-scale color scheme (light for the highest recorded intensity and dark for the lowest) a topographical micrograph can be generated. Figure 1-2 and 1-4 show typical examples of SEM SE micrographs. SEM micrographs are often mistaken as photographs of the sample's surface, when in fact they should be correctly visualized as gray scale maps displaying recordings of SE signal intensity versus beam location.

The other important analytical signal used here was from characteristic x-rays, which are x-rays are photons emitted from the sample. The most important property of these x-rays is they are indicative of the sample's elemental composition. When the electron beam strikes the nucleus of an atom, it has the potential to knock out a lower shell electron, ionizing the atom. The atom may then undergo an electron rearrangement to lower its energy state. One route of electron rearrangement is for an outer shell electron to fall into the lower shell vacancy with a corresponding emission of an x-ray.

^{99,104} The emitted x-ray possesses an energy equal to the energy difference between the two electron shells.

Important to the analytical use of these x-rays is each element (with an atomic number greater than carbon) emits a family of x-rays that are characteristic of that element. Energy-dispersive spectroscopy (EDS) is a technique where the emitted characteristic x-rays are collected and their energies are measured. A spectrum of x-ray count versus energy is generated with the aid of computer analysis software. After collection of characteristic x-rays from a sample the analyst is able to identify the sample's elemental components.⁹⁹

Electroless and Electrochemical Deposition

The techniques of electroless and electrochemical deposition are used in Chapter 5. The basis of these concepts will now be introduced to the reader.

Electroless and electrochemical deposition describe two chemical methods of depositing metals and alloys. The principle difference between the two is electroless deposition (also known as autocatalytic deposition) occurs without the application of an electric current from an external source while electrochemical deposition does not.

Electroless Deposition

The method of electroless deposition is a relatively young technique, developed primarily over the last sixty years.¹¹¹ The Martin group has pioneered a method for the electroless deposition of gold inside the pores of polycarbonate track-etch membranes.¹¹² The surface of the polycarbonate is first sensitized with Sn^{2+} , followed by the galvanic reduction of silver, which undergoes a galvanic replacement by gold. The gold then acts

as a catalytic site for the continued reduction of gold ions in solution by formaldehyde.

The applicable equations can be written as Equations 1-4 through 1-6,



where A denotes the species is adsorbed on the surface of the membrane. This electroless deposition method has been used to fabricate gold nanorods,^{17,113} to coat the walls of the membrane, to produce a molecular sieve,^{69,114,115} and Coulter CounterTM like devices,¹¹⁶ to alter the membrane's transport and selectivity properties by the attachment of organic species to the gold coated pore walls,^{69,117,118,119} to create a conductive surface for the purpose of applying a potential,¹¹² and to manufacture electrochemical sensors.^{17,120}

Although the Martin group pioneered the electroless deposition of gold in nanoporous membranes, the membrane replication study in Chapter 5 required a more mechanically sound material. Metallic nickel was selected for this task. Gold is a soft ductile material, making it difficult to fashion the needed free-standing high-aspect ratio nanostructures for the replication project. Nickel is a more suitable building material due to its greater hardness and lower ductility. Metallic nickel has a high melting point of 1453°C, a density of 8.92 g/cm³ and a tensile strength of 317 MPa.¹²¹ This is in comparison to gold, which has respective values of 1063°C, 19.3 g/cm³, and 50.7 MPa.

The electroless depositon of nickel was reborn in 1944 with the investigations and eventual publications of Brenner and Riddell in 1946 and 1947.¹²² When nickel is deposited, there are four main reducing agents that are used: hypophosphite, sodium borohydride, amine boranes, and hydrazine. The first produces a Ni-P alloy, the second

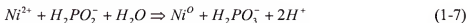
and third produce Ni-B alloys, and the fourth yields nickel metal with a purity of near 99%.^{111,122}

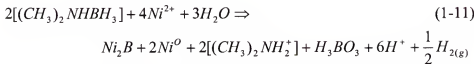
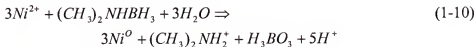
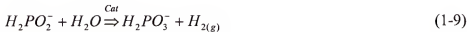
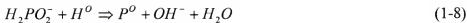
Two types of electroless plating solutions were chosen for our studies (Table 1-1).¹²² Plating Solution A, containing hypophosphite, is known to yield a Ni-P alloy with 4-11% phosphorus. When nickel-phosphate alloy is deposited electrolessly it possesses a low internal stress and good corrosion resistance, has a low-porosity, and is non-magnetic.¹¹¹ Plating Solution B produces a nickel-boron alloy with 5 to 7% boron.¹²² The properties of this nickel-boron alloy is comparable to those of the nickel-phosphorus, but with an increased hardness and better performance at temperatures above 400°C.¹¹¹

Table 1-1. Selected solutions for electroless deposition.

Composition	Plating Solution (g/L)	
	A	B
Nickel Chloride	42	--
Nickel Sulphate	--	20
Sodium hypophosphite	24	--
Sodium citrate	45	--
Ammonium chloride	30	15
Dimethylamine borane	--	3
Ammonium citrate	--	12
2-Mercaptobenzothiazole	--	2E-4 M

When the electroless deposition of nickel is performed, there are certain prevalent facts: 1) hydrogen gas will be emitted during deposition, 2) the deposited nickel is rarely pure (addressed above), 3) hydrogen ions are generated, and 4) this process is far from 100% efficient.¹¹¹ Examples of each can be seen in the equations that describe electroless deposition with hypophosphite (Equation 1-7 to 1-9) and dimethylamine borane reducing agents (Equation 1-10 to 1-12).





Equations 1-7 and 1-10 show the reduction of Ni^{2+} ion to elemental nickel. The four remaining equations illustrate the side reactions that occur to differing degrees. The side reactions produce impurities of phosphate (Equation 1-8) and borane (Equation 1-11) and generate the evolution of hydrogen gas (Equation 1-9, 11 and 12). Not known is the extent of hydrogen release from these solutions, nor how this gas formation may affect the efficiency of deposition into nanometer sized spaces.

Electrochemical Deposition

Electrochemical deposition, or electroplating, involves the deposition of a material upon an electrode.¹²¹ Nickel was chosen as the deposition material in Chapter 5, therefore it will be our focus here. Electroplating has been studied since 1837,¹²¹ with a large volume of research focused on the plating of nickel. This body of work has lead to the widespread use of electrochemical deposition in industry today.^{123,124} The main advantages of electrochemical deposition is it can be applied to small and large work pieces using relatively cheap deposition solutions.¹²¹

The nickel solution chosen for electrochemical plating is a slight variation of the Watts bath, described by Professor O.P. Watts in 1916.¹²⁵ The solution used (180 g/L nickel sulphate, 8 g/L ammonium chloride and 30 g/L boric acid) falls under the classification of a Hard Watts formulation,¹²² because the deposited nickel possesses a hardness, tensile strength, and yield strength almost twice that of nickel deposited from a regular Watts bath.

Data Presentation

Several points throughout this dissertation a numerical value is presented in a table or in the text (flux, moles transported). Each presented value is the average of three independent experiments, and the plus-or-minus number accompanying the value is the calculated standard deviation for the three experimental values. This is true in all cases unless otherwise stated. Graphical data is presented in a similar manner. Each point on a graph is the average of three independent experiments, and the accompanying error bars represent the calculated plus-or-minus standard deviation for those three values.

Dissertation Overview

The goals of this research was to understand the fundamental principles of membrane transport with silane-treated nanoporous anodic alumina membranes and fabricate polymeric replica membranes of these anodic alumina membranes. Chapter 1 has introduced the reader to track-etch and nanoporous anodic alumina membranes, membrane based transport and separations, silanization, the Langmuir adsorption isotherm, SEM and its principles, and electroless and electrochemical plating. All of the concepts and ideas that were presented are important to fully understand the information discussed in the following chapters.

Chapter 2 explores the modification of nanoporous anodic alumina membranes with an alkyl silane. The changes in surface wetting properties with water and transport properties of Ni^{2+} and neutral molecules are reported. Transport studies were carried out with a homologous series of permeat molecules and the respective selectivities were calculated.

In Chapter 3 and Chapter 4, silane-treatment of nanoporous anodic alumina membranes is explored further. Chapter 3 reports the results from silane-treatments with differing alkyl groups than the one utilized in Chapter 2, while Chapter 4 investigates the transport of species that can reside in a neutral or charged state (depending on solution pH). The alkyl silane used for the studies in Chapter 2, was once again used in Chapter 4. The results of pH-dependant transport are presented and fitted to theoretical predictions based on alpha values. Good agreement was found between the predicted and recorded results.

Chapter 5 looks at the production of polymeric replicas from nanoporous anodic alumina membranes. Replication was based on electroless and electrochemical methods. The results of these methods and their level of success are presented.

Chapter 6 summarizes the results of this dissertation and gives the overall drawn conclusions.

CHAPTER 2

TRANSPORT RATE AND SELECTIVITY IN SILANE MODIFIED NANOPORE ALUMINA MEMBRANES

Introduction

Nanopore membranes are available from a number of sources and have been used for numerous applications including separations,^{126,127,128} filtrations,^{129,130} extractions,¹³¹ materials science,^{132,133,134} and various membrane based technologies.^{135,136,137,138} The Martin group has a long standing interest in cylindrical nanopore membranes, more specifically nanopore plastics made by the track-etch method,^{21,139} and nanopore anodic alumina membranes made by the oxidation of aluminum metal.^{33,35,41,46} Some of the prior work has entailed using these membranes as templates for preparing nanowires and nanotubes via template synthesis.^{140,141,142,143,144}

The group has also investigated the influence of the pore wall chemistry on the membranes transport properties.^{112,145,146} Most of this prior work has focused on the nanopore track-etch membranes, after the electroless deposition of cylindrical gold nanotubes within the pores.¹¹⁹ Since the deposited Au is relatively easy to chemically functionalize with thiols, these gold nanotube membranes are very ideal for investigating how pore-wall chemistry effects membrane transport rate and selectivity.¹¹²

Nanopore anodic alumina membranes are also easily chemically functionalized, using well-known silane coupling chemistry.^{73,147} Building on our breadth of experience with the track-etch membranes, we were interested in learning the effects of silane-treatment on the rate of transport and selectivity in these membranes. To our knowledge,

studies of this type have not been conducted on the anodic alumina nanopore membranes. After silane-treatment of the alumina membrane with the hydrophobic octadecyltrimethoxy silane (ODS), we found the pores were no longer flooded by water. Nevertheless, hydrophobic molecules were still able to traverse the membranes, passing freely from an aqueous feed on one side of the membrane to an aqueous receiver solution on the other side.

We were able to show the mechanism of transport entailed Langmuir-like adsorption of the hydrophobic molecule with the ODS layer. More specifically, the molecules passed from the feed solution into the ODS layer coating the pore walls. Then a solid-state diffusion occurred along the ODS layer, followed by the release of the molecules into the receiver solution. The pores of these ODS-treated alumina membranes were filled with water immiscible solvents (kerosene or mineral oil) to make a new type of supported liquid membrane.^{105,148,149} Greater fluxes and selectivities were expressed with these water immiscible liquid filled ODS-treated membranes. The results of these investigations are described here.

Experimental

Materials

Alumina Anodisc® 47 filter membranes (60 µm thick, 47 mm diameter and ~50% porosity) were obtained from Whatman. Two different versions of these membranes were used. The first contained nominally cylindrical pores with a pore diameter, as specified by the supplier, of 200 nm; these are designated here as the CP200 membranes. The second type of membrane contained cylindrical pores through most of the membrane's thickness, but these pores branched into nominally 20 nm diameter pores at

one face of the membrane. The branched pore region of the membrane accounted for ~1 μm of the membrane's total thickness.¹³¹ These branched pore membranes are designated here as BP20 membranes.

NiSO₄, phenol, p-cresol, 2,4-dimethylphenol, 2,4,6-trimethylphenol, tetrahydrofuran, hexane, kerosene, light mineral oil, absolute alcohol, sodium acetate, NaH₂PO₄, and hexagonal polystyrene weighing dishes were used as received from Fisher Scientific. Octadecyltrimethoxysilane was obtained from Gelest and used as received. Extra fast setting epoxy was obtained from Cole Parmer and used as instructed. Purified water was prepared by circulating house-distilled water through a Millipore Milli-Q water purification system ($>17 \text{ M}\Omega \text{ cm}^{-1}$).

Membrane Modification

Before modification, the alumina membranes were cleaned by sequentially rinsing with water, tetrahydrofuran and acetone. This rinse sequence was performed a total of three times. Modification was accomplished by immersing the membrane into a solution prepared by mixing 2 mL of the desired silane with 15 mL of absolute alcohol and 1 mL of a 50 mM pH = 5.1 sodium acetate solution. Membranes were treated in this solution for 1 hour with agitation, rinsed with absolute alcohol, and placed in an oven overnight at 80°C.

Transport Experiments

Two membrane sample groups were investigated. The first group consisted of the untreated and silane-treated membranes (CP200 and BP20 membranes). The second group consisted of the silane-treated membranes but modified with an organic solvent (either kerosene or light mineral oil) incorporated into the pores. For the membranes

without chemical modifiers, the membrane samples were assembled as described previously, and then clamped between the two halves of a U-tube permeation cell (Figure 2-1).^{114,120} The membrane assembly exposed a 0.71 cm^2 area of the membrane to the solutions placed in the half-cells. A feed solution (15 mL) containing a known concentration of the permeating molecule or ion (dissolved in 50 mM, pH = 7 NaH₂PO₄ buffer) was placed in the feed half-cell, while only buffer was placed in the receiver half-cell. The U-tube cell was placed into a constant temperature bath at $25\pm1\text{ }^\circ\text{C}$, and both half-cell solutions were vigorously stirred during the transport experiments.

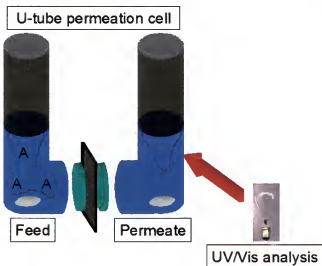


Figure 2-1. U-tube permeation cell set-up.

The membrane assembly discussed above could not be used for the membranes containing an organic solvent within the pores. This is because this assembly uses parafilm to secure the membrane sample,¹²⁰ and parafilm is not chemically compatible with the two solvents used here (Figure 2-2). A polystyrene based membrane assembly was used instead. A 0.97 cm^2 area hole was punched into a section of the polystyrene that was cut from the bottom of a weighboat ($\sim 280\text{ }\mu\text{m}$ thick). Epoxy glue was applied

around the hole, and the alumina membrane sample (without the chemical modifier) was firmly placed in the epoxy such that the membrane completely covered the hole.

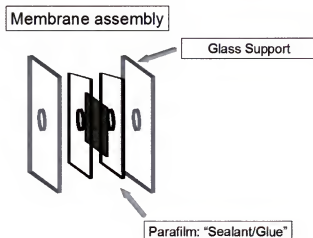


Figure 2-2. Membrane assembly without a subphase.

For membranes using kerosene as the chemical modifier, the membrane assembly was first mounted in the U-tube permeation cell, and kerosene was then pipetted onto the membrane surface to fill the pores. Kerosene freely entered the pores due to its relatively low viscosity and its affinity for the ODS layer. The feed and receiver half-cells were then immediately filled; this protocol minimized evaporation of the kerosene from the membrane. Because mineral oil has a much lower volatility, the membranes were loaded with this chemical modifier before mounting them in the U-tube cell. Though mineral oil possesses a greater viscosity than kerosene, it still readily entered the pores. Again, the cell was thermostated and stirred during the transport experiments.

The flux of the permeating species from the feed half-cell through the membrane and into the receiver half-cell was determined by periodically measuring the UV or visible absorbance of the receiver solution. The following wavelengths were monitored: Ni^{2+} - 385 nm, phenol - 268 nm, p-cresol - 276 nm, 2,4-dimethylphenol - 276 nm, and 2,4,6-trimethylphenol - 277 nm. An Agilent 8453 UV-Visible spectroscopy system with

Agilent ChemStation software was used for all UV/Vis analysis. Calibration curves were used to convert the measured absorbance to the concentration of permeating species in the receiver half-cell.

Contact Angle Measurements

A Tantec CAM-Micro contact meter was used to determine surface contact angles for the untreated and silane-treated membranes using the half-angle technique, as described in the user's manual. A ten microliter water droplet was dispensed for each measurement and four total measurements were recorded across the surface of each sample.

Results and Discussion

Transport of Ni²⁺ and 2,4-Dimethylphenol through Untreated Versus Octadecyltrimethoxysilane-Treated Membranes

Figure 2-3A shows plots of the flux of moles of Ni²⁺ transported versus permeation time across untreated and octadecyltrimethoxysilane (ODS) treated CP200 membranes. For the untreated membrane the plot is linear, and the flux of Ni²⁺ across the membrane ($58 \pm 3 \text{ }\mu\text{moles cm}^{-2} \text{ hr}^{-1}$) was obtained from the slope. However, with a membrane that has undergone ODS treatment, after permeation times as long as 24 hours (data not shown) no evidence of Ni²⁺ was observed.

A contact angle could not be measured for a water droplet applied to the surface of the untreated alumina because they rapidly spread across the membrane's surface and readily filled the pores. In contrast, the contact angle of water on the surface of an ODS-treated membrane was 120°, with no evidence of pore filling. The lack of pore wetting prevents Ni²⁺ from being transported across ODS-treated membranes because Ni²⁺

permeation is limited to wherever the aqueous solution has access to. Since there is no access to the pores of the membrane, the feed solution is isolated from the permeate solution, which means nickel has no transport passage way from the feed to the permeate solution. Analogous results were obtained for gold nanotube membranes that had been treated with hydrophobic hexadecyl thiol.^{118,120}

Figure 2-3B shows the analogous flux plots of 2,4-dimethylphenol (DMP) transported across untreated and ODS-treated CP200 membranes. Because of its lower extinction coefficient, the feed concentration used in the Ni²⁺ experiments (Figure 2-3A) was an order of magnitude higher than in the DMP experiments (Figure 2-3B). Which accounts for the lower flux of DMP in the untreated membrane ($5.94 \pm 0.07 \text{ } \mu\text{moles cm}^{-2} \text{ hr}^{-1}$). However, when the fluxes are corrected for the feed concentration difference, the Ni²⁺ and DMP fluxes in the untreated CP200 membranes are identical. This indicates the aqueous-phase diffusion coefficients for these two species do not significantly differ.

A difference in the transport rates of Ni²⁺ and DMP could only be seen with the ODS-treated membrane. DMP expressed a measurable flux and no flux was observed for Ni²⁺. DMP flux through these silane-treated membranes was only 28% lower than in the untreated case (Figure 2-3B). Based on the contact angle measurements and transport data, we have already shown pure water and water containing 100 mM Ni²⁺ is unable to wet the pores of an ODS-treated membrane. One possible explanation for a DMP flux across the ODS-treated membranes is the 10 mM DMP alters the aqueous solution properties to the point that the solution is able to wet the pores of the membrane.

To investigate this possibility, transport experiments were done with an ODS-treated CP200 membrane using a feed solution 10 mM in DMP and 100 mM in Ni²⁺. If

DMP promoted the flooding of the pores, then a flux for Ni^{2+} would be observable with this experiment. When performed the flux of DMP was identical to that obtained when only DMP was present in the feed, while no measurable Ni^{2+} flux was recorded. These results show DMP is being transported across the ODS-treated membrane even though the pores are not wetted by water. Put another way, the transport mechanism for the ODS-treated membrane is different than the solution-diffusion mechanism operative in the water-filled pores of the untreated membrane.

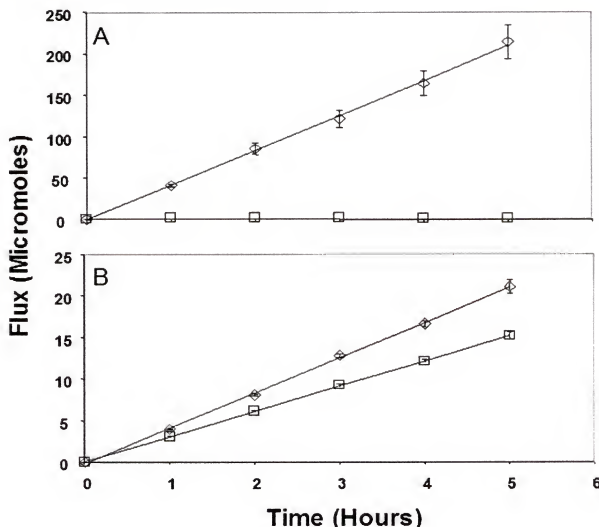


Figure 2-3. Transport of A) Ni^{2+} , and B) 2,4-dimethylphenol (DMP) with a CP200 (◊), and octadecyltrimethoxysilane (ODS) treated CP200 membrane (□). (Single molecule/ion experiments with feed concentrations of 100 mM Ni^{2+} and 10 mM DMP.)

Transport of a Homologous Series of Hydrophobic Permeate Molecules

At least two possible transport mechanisms can be proposed for the ODS-treated membrane. The first entails vapor pressure driven evaporation of the DMP from the feed solution at the membrane-solution interface, vapor phase transport through the dry pores, and re-dissolution of the DMP in the receiver solution. The second entails hydrophobic driven partitioning of the DMP from the feed solution into the hydrophobic ODS-treated membrane, transport via diffusion in (or on) the ODS films lining the pore walls, and back partitioning of the DMP into the receiver solution (Figure 2-4). In both cases, the net driving force for transport is the difference in chemical potential of DMP between the feed solution, where it has a finite (and for these experiments constant) concentration, and the receiver solution where, for these experiments, its concentration is always effectively zero.

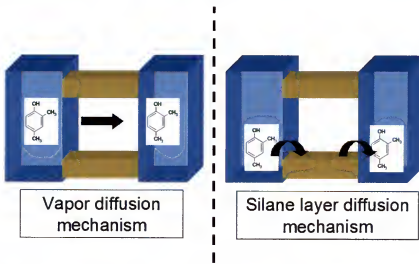


Figure 2-4. Vapor and silane layer diffusion mechanisms.

Transport experiments on a homologous series of hydrophobic permeating molecules can be used to distinguish between these two possible mechanisms. If the vapor-phase mechanism is operative, flux will decrease with the increasing molecular

weight of the molecules in the homologous series because vapor pressure decreases with increasing molecular weight.¹⁵⁰ In contrast, if the partitioning model is operative, flux will increase with the increasing molecular weight of the molecules in the homologous series. This is true because the partition coefficient for these hydrophobic molecules from the aqueous feed solution and into the hydrophobic ODS-treated membrane will increase with increasing molecular weight of the permeating molecule.¹⁵⁰ However, as will be discussed in the following section, at least two different transport models involving chemical partitioning driven by the hydrophobicity of the permeate species can be considered.

The homologous series used consisted of phenol, p-cresol (PC), DMP, and 2,4,6-trimethylphenol (TMP) (Figure 2-5). Permeation experiments with this series were first performed with untreated CP200 and BP20 membranes using 2 mM feed solutions of the permeating molecule. For both membranes, the resulting transport plots were linear, and the calculated slopes are the mathematical fluxes of the various permeating molecules through these membranes.

For the untreated CP200 and BP20 membranes, the fluxes of all members of the homologous series were very similar for each membrane. For the CP200 membrane the recorded fluxes were: phenol = 1.45 ± 0.07 , PC = 1.38 ± 0.8 , DMP = 1.38 ± 0.8 , and TMP = 1.27 ± 0.07 $\mu\text{moles cm}^{-2} \text{ hr}^{-1}$. For the BP20 membrane the recorded fluxes were phenol = 0.283 ± 0.005 , PC = 0.26 ± 0.02 , DMP = 0.256 ± 0.004 , and TMP = 0.228 ± 0.004 $\mu\text{moles cm}^{-2} \text{ hr}^{-1}$. Based on standard deviations, the BP20 membrane expressed slightly greater selectivities than the CP200 membrane. The greatest difference in flux, almost 20%, was observed between phenol and TMP.

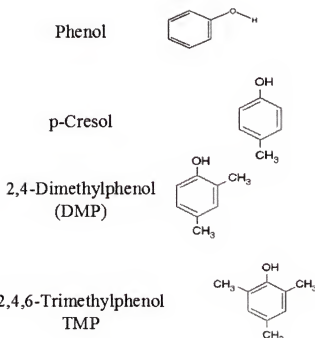


Figure 2-5. Homologous series of permeate molecules and their respective structures.

Figure 2-6 shows flux plots for the homologous series with the ODS-treated CP200 and BP20 membranes for feed concentrations of 2 mM. In general, the fluxes increase with increasing molecular weight of the molecules in this series. This trend is the opposite of what was observed for the untreated BP20 membrane and the opposite of what would be expected if the vapor-phase transport mechanism was dominant. This data is, however, consistent with the hydrophobically driven chemical-partitioning mechanism, suggesting this mechanism is operative in the ODS-treated membranes.

The fluxes obtained from the slopes in Figure 2-6 can be used to quantitatively evaluate the transport selectivity for the ODS-treated membranes. This was accomplished by dividing the flux of each permeating molecule in a particular membrane by the flux of phenol for that membrane. Phenol was chosen as the reference because it showed the lowest fluxes, yielding selectivity coefficients (α_p) greater than unity (Table 2-1).

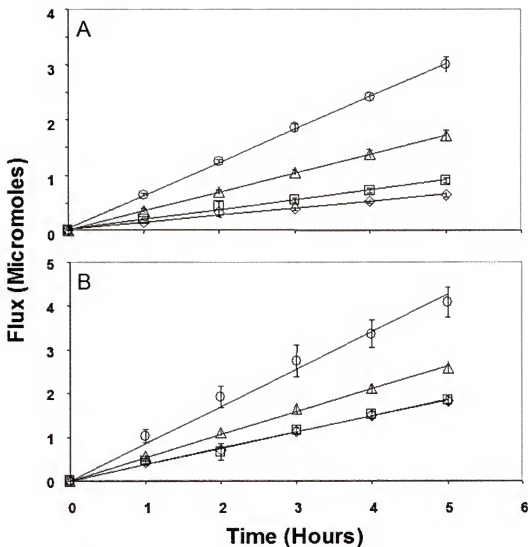


Figure 2-6. Flux plots for ODS-treated A) BP20 and B) CP200 membranes with a 2 mM feed solution. (\circ = TMP, Δ = DMP, \square = p-cresol, \diamond = phenol)

Table 2-1 quantifies the conclusion that transport in the ODS-treated membranes entails hydrophobically driven partitioning of the permeating molecule into the membrane. It is of interest to note, however, the selectivity coefficients for the BP20 membrane are larger than for the CP200 membrane. In agreement with the bare membrane experiments, the fluxes obtained with the BP20 membrane are lower than with the CP200. However, with the BP20 membrane there is a larger suppression of the flux of phenol, which accounts for its larger selectivities. In the end, it was seen there is an

inherent trade-off between an optimized flux and an optimized selectivity with the ODS-treated membranes.

Table 2-1. Calculated selectivities for ODS-treated BP20 and CP200 membranes. Feed concentrations were 2 mM.

ODS Modified Membrane	Analyte	Flux ($\mu\text{moles cm}^{-2}\text{hr}^{-1}$)	Selectivity (α)
BP20	Phenol	0.176 ± 0.009	1
	p-Cresol	0.25 ± 0.01	1.4
	DMP	0.480 ± 0.002	2.73
	TMP	0.838 ± 0.009	4.76
CP200	Phenol	0.51 ± 0.01	1
	p-Cresol	0.52 ± 0.02	1.0
	DMP	0.72 ± 0.01	1.4
	TMP	1.13 ± 0.05	2.2

Elucidating the Transport Mechanism. At least two different transport mechanisms involving hydrophobically driven chemical partitioning of permeate species into the membrane can be proposed. Both mechanisms entail Fick's first law of diffusion and, assuming a linear concentration gradient across the membrane, can be written as

Equation 2-1,

$$J_x = -D \frac{\Delta C}{L} \quad (2-1)$$

where J_x is the flux of a hydrophobic permeating molecule (X) through the membrane, D is the diffusion coefficient for X in the membrane, ΔC is the concentration gradient of X across the membrane, and L is the membrane thickness.

The first mechanism assumes that partitioning of the hydrophobic molecule X into the membrane is akin to the solvent extraction of X from water into an immiscible nonpolar solvent¹⁵¹.



The partition coefficient, K_P , is given by Equation 2-3.

$$K_p = \frac{[X_{memb}]}{[X_{aq}]} \quad (2-3)$$

However, in our transport experiments, the concentration of X in the membrane on the feed-solution side would be $[X_{memb}]$, and the concentration of X in the membrane on the receiver-solution side would be effectively zero. This makes $\Delta C = [X_{memb}]$ and $[X_{memb}]$ also equal to $K_p [X_{aq}]$, after rearranging Equation 2-3. Substituting this into Equation 2-1 gives Equation 2-4.

$$J_x = -DK_p \frac{[X_{aq}]}{L} \quad (2-4)$$

According to Equation 2-4, the flux is linearly related to $[X_{aq}]$ (the concentration of the permeating molecule X in the feed solution) for a bulk solution partitioning case.

The alternative transport mechanism assumes that partitioning into the membrane is described by the Langmuir adsorption isotherm, which can be written as Equation 2-5,^{81,82,83,84}

$$[X_{memb}] = \frac{C_{max} K_L [X_{aq}]}{1 + K_L [X_{aq}]} \quad (2-5)$$

where C_{max} is the saturation concentration of X in the membrane and K_L is the Langmuir adsorption constant.

In our membranes, K_L reflects the hydrophobic driven adsorption of X from the aqueous feed solution onto the hydrophobic ODS layers lining the pore walls in the membrane. Substituting Equation 2-5 into Equation 2-1, and recalling $\Delta C = [X_{memb}]$, gives Equation 2-6,

$$J_x = \frac{-D}{L} \left(\frac{C_{max} K_L [X_{aq}]}{1 + K_L [X_{aq}]} \right) \quad (2-6)$$

which means, with experimental flux data, Equation 2-6 can be used to solve for K_L . Figure 2-7 shows the flux of phenol across the ODS-treated BP20 membrane versus concentration of phenol in the feed solution. Phenol was selected because of its high solubility of ~850 mM³¹ (under these experimental conditions it was determined to be between 700 and 750 mM). The inset shows an enlarged graph of the feed concentrations from zero to 500 mM. Early stages of a plateau are seen in the data between 300 and 500 mM before the flux suddenly increases. Equation 2-6 predicts the behavior seen in Figure 2-4 up to a feed concentration of 500 mM, whereas Equation 2-4 does not. In order fit the data, the reciprocal of Equation 2-6 is taken and, after some mathematical rearrangement, gives Equation 2-7.

$$-J_x^{-1} = \left(\frac{L}{DC_{\max} K_L} \right) \frac{1}{[X_{aq}]} + \frac{L}{DC_{\max}} \quad (2-7)$$

A plot of Equation 2-7 yields a straight line, where the slope is $(L / DC_{\max} K_L)$ and the y-intercept is (L / DC_{\max}) . To solve for K_L the y-intercept is divided by the slope. The experimental flux data from 0 to 500 mM was graphed as one over flux versus one over the feed concentration. A best-fit line was found, with an r^2 value of 0.9991, a y-intercept of $-18 \pm 7 \text{ }\mu\text{moles cm}^{-2} \text{ hr}^{-1}$ and a slope of $-20500 \pm 200 \text{ }\mu\text{moles cm}^{-2} \text{ hr}^{-1} \text{ mM}$. Using this graphical data, a K_L value of 0.86 M^{-1} was calculated. In the literature a value of 0.75 M^{-1} ¹ was found for the adsorption of phenol on a zeolite modified with a hexadecyl moiety.⁹⁵ Therefore the value obtained here is in good agreement with the literature.

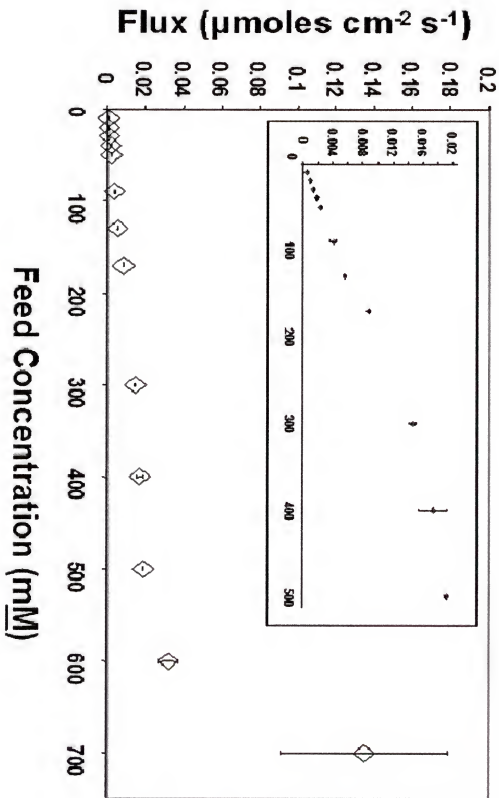


Figure 2-7. Flux of phenol vs. phenol feed concentration for an ODS-treated BP20 membrane. Inset is a magnification from 0 to 500 mM.

The fact the transport data fit an adsorption isotherm model (Equation 2-6) better than a solvent extraction model (Equation 2-4) is reasonable since the permeating molecule does not partition into a liquid subphase within the pores, but rather it partitions onto the C₁₈ groups lining the pore walls. However, contrary to Equation 2-6, at feed concentrations greater than ~500 mM, the flux increases dramatically above the saturation value (Figure 2-7) with the value at 700 mM being most conspicuous. It occurred to us this sudden increase in flux might reflect a change in the properties of the aqueous solution at these very high concentrations of phenol, leading to flooding of the pores of the membrane.

To explore this issue, we made contact angle measurements on the ODS-treated BP20 membrane with aliquots of the various feed solutions used in Figure 2-7 (Table 2-2). The contact angle decreased dramatically at the highest feed concentrations. This indicated the sudden increase in flux observed (Figure 2-7) was caused by the mechanism of phenol transport switching from one type to another. At the highest phenol concentrations the transport mechanism changed from the Langmuir adsorption model in dry pores to a simple solution-diffusion process in solvent-flooded pores. This is a reasonable conclusion because it is known that for a solution in contact with the surface of a porous material possessing a contact angle less than 90° the solution will eventually enter and flood the pores.⁶²

The large standard deviation for the highest phenol concentration is probably a reflection of the lack of reproducibility for the rate of flooding of the pores. At these larger fluxes, any variation in wetting time greatly alters the overall flux.

Table 2-2. Contact angle measurements of phenol solutions on an ODS-treated BP20 membrane.

Phenol Concentration (mM)	Contact Angle (degrees)
Water	119.8 ± 0.5
30	119.2 ± 0.5
50	119.8 ± 0.5
90	117 ± 2
170	108 ± 3
300	99 ± 2
500	75 ± 2
600	64 ± 4
700	Could not be determined

Creating a Liquid Subphase within the Pores. Saturation of the flux at high feed concentrations (Equation 2-6, Figure 2-4) is undesirable because it limits the range of concentrations over which optimal transport selectivity will be observed. By creating a liquid subphase (a supported liquid membrane) within the pores^{148,149} saturation should be eliminated or at least pushed to such high feed concentrations that the solubility of the permeating molecule in the subphase will be exceeded first. Simple construction of a liquid subphase is accomplished by filling the pores of the ODS-treated membrane with a water immiscible liquid. Two such liquids were explored here – kerosene and light mineral oil. Kerosene is a mixture of C₉ to C₁₆ hydrocarbons¹⁵² whereas mineral oil contains much longer hydrocarbons ranging from 18 to 35 carbons in length.¹⁵³

With the introduction of a subphase we would expect the transport rate of a species to be related to its partition coefficient between the aqueous and organic phases. The partition coefficients for these species were determined graphically in the following manner.^{154,155} First, the mass balance equation for partitioning can be written as Equation 2-8,

$$V_{aq} C_o = V_{aq} C_{eq} + V_{org} C_{org} \quad (2-8)$$

where V_{aq} is the aqueous phase volume, C_o is the initial analyte concentration, C_{eq} is the analyte in the aqueous phase equilibrium concentration, V_{org} is the volume of the organic phase, and C_{org} is the analyte organic phase equilibrium concentration. Dividing Equation 2-8 by V_{aq} and, after rearrangement Equation 2-9 is produced.

$$\left(\frac{C_o}{C_{eq}} \right) - 1 = K \left(\frac{V_{org}}{V_{aq}} \right) \quad (2-9)$$

This graphically states the partition coefficient is the slope of the line described by the above equation. Figures 2-8A and 2-8B shows the graphical data used for the determination of the partition coefficients of our analytes with kerosene and mineral oil.

Based on Equation 2-9, it would be expected the best-fit lines for each set of data points would pass through point (0,0). In the case of phenol this is not true. The equilibrium studies were performed in closed containers with UV\Vis analysis performed on the aqueous layer. Initially, it was thought the total volumes of the aqueous and organic solvents were too low because they did not completely fill the container. The vacant space above the solvents allowed for phenol evaporation, which reduced the concentration of phenol within the solvents. To lessen this effect, larger volumes of solvent were used, reducing the solvent to vacant space ratio. Even when the largest liquid volume (40 mL, with 1 mL vacant space) was used, the best-fit lines through the data sets still did not pass through the point (0,0). A better design of this experiment would have been to measure the concentration of phenol in the aqueous and organic solvents to determine how much, if any, phenol was lost as a gaseous species.

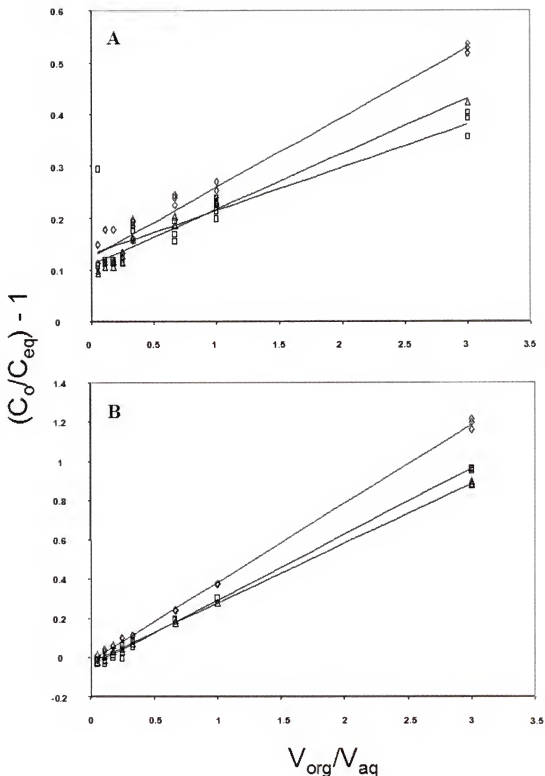


Figure 2-8A. Bulk solvent partition data for A) phenol and B) p-cresol used to determine partition coefficients between an aqueous and organic phase (\diamond hexane, \square = kerosene, Δ = mineral oil).

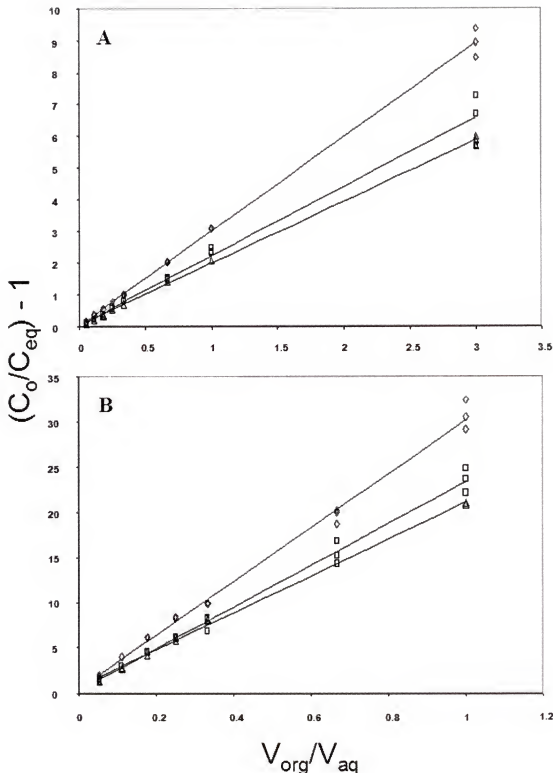


Figure 2-8B. Bulk solvent partition data for A) DMP and B) TMP used to determine partition coefficients between an aqueous and organic phase (\diamond hexane, \square = kerosene, Δ = mineral oil).

Table 2-3 summarizes the results of these solvent-partitioning experiments. An encouraging result from this data is the high predicted selectivity between phenol and TMP of ~180 with both kerosene and mineral oil. Thus, it would be expected the introduction of either subphase into the pores of the membrane would yield three advantages. First, we would expect greater selectivities than with only using an ODS-treated membrane alone. Second, we would expect greater fluxes with kerosene than with mineral oil, since mineral oil has a viscosity about 30 times greater than kerosene.³¹ Third, saturation of these membrane systems would be expected at higher analyte feed concentrations than with the membranes only treated with ODS.

Table 2-3. Calculated partition coefficients and selectivities based on bulk solution extractions.

		Partition Coefficient [l org/l aq]	Selectivity
Hexane	Phenol	0.14±0.01	1
	pCresol	0.402±0.003	3.0
	DMP	2.97±0.04	22
	TMP	29.8±0.6	220
Kerosene	Phenol	0.13±0.01	1
	pCresol	0.336±0.004	2.7
	DMP	2.18±0.06	17
	TMP	23.1±0.6	180
Mineral Oil	Phenol	0.12±0.01	1
	pCresol	0.304±0.003	2.6
	DMP	1.95±0.02	17
	TMP	20.4±0.4	180

We wanted to see if these advantages were true for the untreated, as well as for the ODS-treated membranes. The solvents were applied to the untreated membrane but it was seen the liquid was rapidly displaced from the pores by the aqueous feed solution. This rapid leaching of the solvents from the pores of the membrane made it impossible to obtain reproducible data. However, if the solvents were placed in the ODS-treated membranes, experiments could be performed for at least five days before leaching from the pores could be detected.

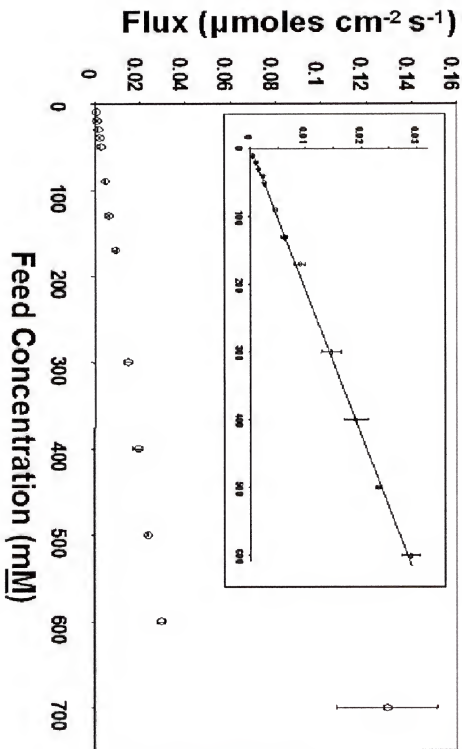


Figure 2-9. Flux of phenol vs. the phenol feed concentration for an ODS-treated BP20 membrane containing kerosene. Inset is a magnification from 0 to 600 mM.

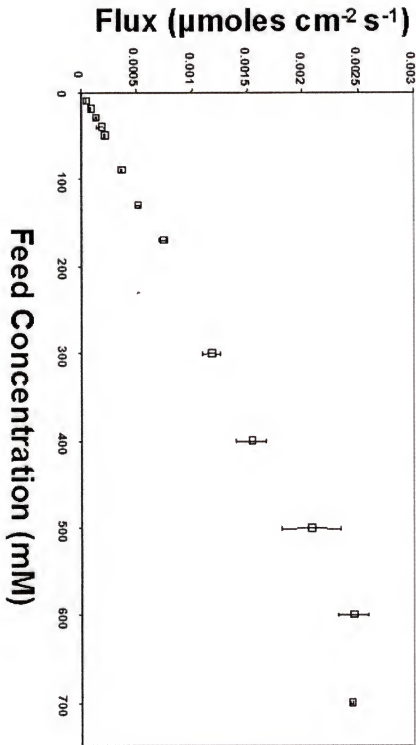


Figure 2-10. Flux of phenol vs. the phenol feed concentration for an ODS-treated BP20 membrane containing mineral oil.

Figure 2-9 shows plots of phenol flux versus the concentration of phenol in the feed solution for an ODS-treated BP20 membrane containing kerosene within the pores. The first point to note is that unlike the BP20 membrane with no liquid subphase (Figure 2-7), the flux does not form a saturation plateau. Instead (as predicted by Equation 2-4), the flux increases linearly with feed concentration until the pores were flooded by water at 700 mM for the same reasons as with the ODS-treated membranes.

Figure 2-10 shows analogous data for an ODS-treated BP20 membrane with mineral oil in the pores. With this membrane, we again see an extended (relative to data in Figure 2-7) region where phenol flux varies linearly with feed concentration. Apparent saturation is observed above 600 mM, but this was believed to be a result of the limited solubility of phenol in mineral oil. To show saturation was occurring, the following was performed.

Increasing amounts of phenol was dissolved in bulk mineral oil until phenol reached its saturation point within a range of 90 and 150 mM it reached its saturation point. Saturation was indicated by a clear solution at 90 mM and a slightly cloudy suspension at 150 mM. This would imply, if the concentration of phenol in the mineral oil filling the pores of the membrane approached this concentration range, then saturation of the membrane would be expected. To quantitatively prove this, we start with the partition equation (Equation 2-10),

$$K = \frac{[X]_{org}}{[X]_{aq}} = \left(\frac{X_{org}}{V_{org}} \right) \left(\frac{V_{aq}}{X_{aq}} \right) \quad (2-10)$$

where V_{aq} and V_{org} are the respective volumes of the aqueous and organic phases. X_{aq} and X_{org} are the respective number of moles in the aqueous and organic phase. Based on the conservation of matter we can write Equation 2-11,

$$X_o = X_{aq} + X_{org} \quad (2-11)$$

where X_o is the total number of moles of X present. We can now substitute $X_o - X_{org}$ for X_{aq} in Equation 2-10 and, after some mathematical rearrangement, we obtain Equation 2-12.

$$X_{org} = X_o K \left[K + \frac{V_{aq}}{V_{org}} \right]^{-1} \quad (2-12)$$

We can solve for X_{org} by substituting for the various known values, $V_{aq} = 0.015$ L and from Figure 2-7 we use a feed concentration of 650 mM, making $X_o = 9.75$ μmoles. The value of K is obtained from Table 2-3, a value of 0.12. The organic volume, V_{org} , is calculated as 2.9 μL based on a membrane thickness of 60 μm, a membrane porosity of ~50%,³¹ and an exposed transport area of 0.97 cm². If we solve for X_{org} we get a value of 208 nmoles. Finally dividing X_{org} by V_{org} gives a phenol concentration of 72 mM in the mineral oil subphase. Within the confinements of the error of these calculations, most importantly the known organic volume, we consider this value within the saturation range determined by using bulk solutions of 90 to 150 mM.

Rate and Selectivity of Transport with Our Supported Liquid Membranes

Figure 2-11 shows plots for the homologous series of hydrophobic permeating molecules through an ODS-treated BP20 membrane with a kerosene and mineral oil subphase. The calculated fluxes from these plots and the corresponding calculated selectivity coefficients are given in Table 2-4.

When kerosene is used as the subphase, the transport flux of phenol does not change greatly (Table 2-4) from the ODS BP20 case (Table 2-1). This is of interest because it shows that phenol permeates through the ODS layer on the walls of the

membrane pores at nearly the same rate as it permeates through a bulk kerosene solvent filling the pores. Thus, with regards to phenol there is only a slight gain in flux when kerosene is used as the subphase. In contrast, the flux of TMP essentially doubles through the kerosene filled pores as compared to the ODS BP20 case. The enhanced flux of TMP with the kerosene subphase results in an overall increase in the calculated selectivity (between phenol and TMP) of almost twice as before.

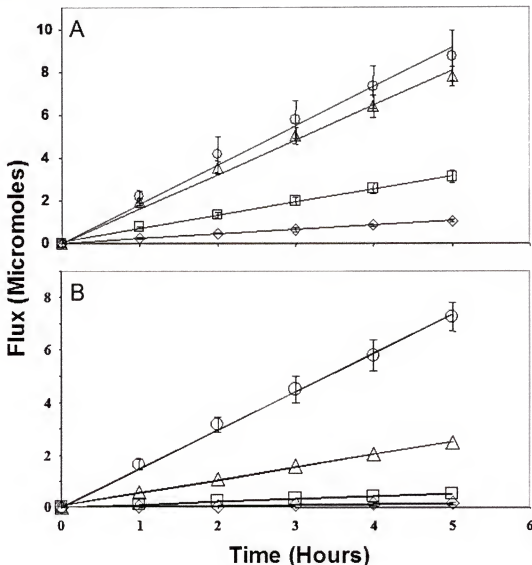


Figure 2-11. Plots for BP20 ODS-treated membranes with a A) kerosene, and B) mineral oil subphase with a 2 mM analyte feed solution. (\circ = TMP, Δ = DMP, \square = p-cresol, \diamond = phenol).

performed to measure the flux the other way. Table 2-5 shows the flux results for phenol and TMP recorded using this method.



Figure 2-12. U-tube permeation cell set-up with organic solvent.

It was observed that phenol and TMP exhibited opposite preferences of transport. Phenol passed out of both organic phases and into the aqueous phase faster than vice versa, while TMP exhibited the opposite trend, preferring passage into the organic phase. Since phenol expresses one order of magnitude preference for passage out of the organic phase, we would expect the overall flux through a membrane with one of these subphases to be limited by how fast it passes into the organic subphase. If we compare the transport fluxes of phenol from the aqueous into the organic (Table 2-5) to the overall experimental fluxes (Table 2-4) we see they are essentially the same.

Similar to the phenol case, the explanation of the transport rate of TMP is almost as straightforward. The flux of TMP from an aqueous solution into the organic solvents was at least 25 times greater than in the opposite direction. This means the total observed

Table 2-4. Calculated selectivities for ODS-treated BP20 membranes, with kerosene and mineral oil subphases. Feed concentrations were 2 mM.

BP20 Solvent Containing Membrane	Analyte	Flux ($\mu\text{moles cm}^{-2}\text{hr}^{-1}$)	Selectivity (α)
Kerosene	Phenol	0.213 ± 0.003	1
	p-Cresol	0.64 ± 0.01	3
	DMP	1.58 ± 0.05	7.42
	TMP	1.78 ± 0.08	8.36
Mineral Oil	Phenol	0.032 ± 0.003	1
	p-Cresol	0.108 ± 0.003	3.3
	DMP	0.50 ± 0.01	16
	TMP	1.48 ± 0.03	46

When mineral oil is used as the subphase (compared to the kerosene subphase case) the flux of TMP drops by ~17% while the flux of phenol drops by a factor of almost ten (Table 2-4). These different magnitudes of change yield a selectivity of ~46 between phenol and TMP. The larger calculated selectivities with a kerosene or mineral oil subphase are not surprising when we look back at the partition studies (Table 2-3). What is surprising is the large discrepancy between the predicted selectivity between phenol and TMP with kerosene and mineral oil (~180) and the experimental values of 8.36 and 46 respectively. To explain this discrepancy and bridge this seemingly large gap between these values, we must explore the transport of these species based on their rates of transport.

First we must determine the rate of passage of phenol and TMP into and out of both kerosene and mineral oil. A simple modification to the transport method was performed by substituting organic solvent for aqueous buffer in one half of the permeation cell (Figure 2-12). If we wanted to measure the flux of the analyte from the aqueous into the organic solvents, the analyte was introduced into the aqueous side and the organic was monitored for the appearance of the analyte. The opposite was

flux of TMP through a membrane containing a subphase of one of these organic solvents would be directly dependant on its release rate from the organic phase. Knowing TMP passes into these subphases faster than it exits them implies that its concentration within the subphase will steadily increase with time. We would expect the steady-state concentration of TMP to fulfill two possible scenarios: 1) TMP is able to reach its equilibrium concentrations, which are dictated by its partition coefficient between the two solvents, or 2) TMP is able to reach its saturation point in the organic solvent.

Table 2-5. Calculated transport rates for phenol and TMP into and out of the bulk phases of kerosene and mineral oil. An ODS-treated BP20 was used to separate the two halves of the permeation cell (Analyte feed concentration of 2 mM.)

Analyte	Flux ($\mu\text{moles cm}^{-2} \text{hr}^{-1}$)			
	Into Kerosene	Out of Kerosene	Into Mineral Oil	Out of Mineral Oil
Phenol	0.22 \pm 0.02	1.91 \pm 0.06	0.0221 \pm 0.002	0.127 \pm 0.009
TMP	6 \pm 1	0.14 \pm 0.01	2.01 \pm 0.03	0.07 \pm 0.02

The saturation range of TMP in kerosene and mineral oil was experimentally determined to be 290 to 330 mM and 150 and 200 mM, respectively. We can assume the concentration of the analyte in the feed remains constant in order to achieve equilibrium with the organic subphase in the pores of the membrane. This is a reasonable assumption since the feed has a volume of 15 mLs while the organic subphase volume (calculated previously) is \sim 3 μL , meaning only a few μmoles of TMP would have to pass out of the aqueous phase into the organic subphase to reach its saturation concentrations. If the system can achieve equilibrium according to its partition coefficient, we would expect a TMP concentration of about 46 mM (based on its calculated partition coefficient) within the subphase when a 2 mM TMP aqueous feed is used. This equilibrium value of 46 mM is well below the saturation range for TMP in

either organic subphase. Therefore we can assume an equilibrium based on partitioning is occurring between the aqueous and organic phases. If we return to our assumption above (the feed concentration remaining constant) we see it is justifiable. A 46 mM TMP concentration in the subphase at equilibrium corresponds to less than a 2% analyte transfer from the aqueous feed to the organic subphase.

Assuming the rate of release of TMP from the organic phase completely dominates the overall measured flux, the expected flux is calculated by multiplying the concentration of the analyte in the subphase by the transfer rate from each subphase, more specifically, 46 mM times 0.07 $\mu\text{moles cm}^{-2} \text{ hr}^{-1} \text{ mM}^{-1}$ for kerosene and 46 mM times 0.035 $\mu\text{moles cm}^{-2} \text{ hr}^{-1} \text{ mM}^{-1}$ for mineral oil (half the flux values in Table 2-5 were used because they were normalized based on a 2 mM feed concentration used to acquire those values). Therefore, the predicted net fluxes for TMP with a membrane containing a kerosene or mineral oil subphase are 3.22 and 1.61 $\mu\text{moles cm}^{-2} \text{ hr}^{-1}$ respectively. The predicted flux of TMP with a mineral oil subphase is almost exactly the same as the experimental values (Table 2-4). However, the predicted flux with a kerosene subphase is almost twice the experimental value (Table 2-4). We are still exploring the transport rates and mechanisms to better understand what could fully explain this discrepancy.

Conclusions

Using alkyl silanes, the permeation characteristics of porous anodic alumina membranes can be selectively altered. It was shown an ODS-treated alumina membrane can be modified to transport hydrophobic species and not hydrophilic species. ODS-treated membranes also showed selectivity among a homologous series of permeate molecules phenol, p-cresol, 2,4-dimethylphenol, and 2,4,6-trimethylphenol. Their

transport rate followed their hydrophobicities, i.e., the most hydrophobic molecule (TMP) had the greatest flux and the least hydrophobic (phenol) had the lowest flux.

The flux of phenol with increasing feed concentrations displayed a trend similar to Langmuirian adsorption isotherm. This trend exhibited a linear region that slowly passed into a plateau. A good fit was found between the linear form of the Langmuir adsorption equation and the experimental data here ($R^2 = 0.9991$). Our affinity constant value K_L , solved for 0.86 M^{-1} , was in good agreement with literature values.

Placing a hydrophobic subphase of kerosene or mineral oil in the ODS-treated membranes increased their selectivity for TMP by almost 2 and 10 fold respectively. Much higher selectivities, as predicted by the partition coefficients, could not be achieved due to a preference based transport limitation. This transport limitation stemmed from phenol and TMP having a preferred transport in these subphases.

CHAPTER 3

TRANSPORT RATE AND SELECTIVITY WITH SELECT SILANES FOR THE SURFACE MODIFICATION OF NANOPORE ANODIC ALUMINA MEMBRANES

Introduction

In Chapter 2 the transport properties of nanopore anodic alumina membranes were investigated. Unmodified membranes, ODS-treated membranes, and ODS-treated membranes with subphases (kerosene and mineral oil) were used for those studies. Here we studied the effect of using a different set of silanes for the surface modification of nanoporous anodic alumina membranes. Diphenyldiethoxysilane (DiPS), 2-hydroxy-4-(3-triethoxysilylpropoxy)diphenylketone (DiPKS), and (heptadecafluoro-1,1,2,2-tetrahydrodecyl)triethoxysilane (CF_3S) were used in these studies.

All three silanes contain hydrophobic organic side groups. Two results were expected after modification with these silanes. First, the surface of the membrane would be rendered hydrophobic, as in the case with ODS. Second, in the case of DiPS and DiPKS, the transport of the phenol family would be facilitated due to the presence of the phenyl side groups.

Experimental

Materials.

BP20 alumina Anodisc® 47 filter membranes (60 μm thick, 47 mm diameter, and ~50% porosity) were obtained from Whatman. Phenol, p-cresol, 2,4-dimethylphenol, 2,4,6-trimethylphenol, hexane, tetrahydrofuran, kerosene, light mineral oil, absolute

alcohol, sodium acetate, citric acid, sodium bicarbonate, N-(1,1-Dimethyl-2-hydroxyethyl)-3-amino-2-hydroxypropansulfonsyre (AMPSO), and sodium phosphate was used as received from Fisher Scientific. (Heptadecafluoro-1,1,2,2-tetrahydrodecyl)triethoxysilane, diphenyldiethoxysilane, and 2-hydroxy-4-(3-triethoxysilylpropoxy)diphenylketone were obtained from Gelest and used as received. Extra fast setting epoxy was obtained from Cole Parmer and used as instructed. Purified water was prepared by circulating house-distilled water through a Millipore Milli-Q water purification system ($>17\text{M}\Omega\text{cm}^{-1}$).

Membrane Modification

Prior to modification, the nanoporous anodic alumina membranes were cleaned by sequentially rinsing with water, tetrahydrofuran, and acetone. This rinse sequence was performed three times. Modification was accomplished by immersing the membrane into a solution prepared by mixing 2 mL of the desired silane with 15 mL of absolute alcohol and 1 mL of a 50 mM pH = 5.1 sodium acetate solution. Membranes were treated in this solution for one hour with agitation, rinsed with absolute alcohol, and placed in an oven overnight at 80 °C.

Transport Experiments

Fabrication of the membrane assembly and subphase modification methods were performed as described in Chapter 2.

The flux of the permeating species from the feed half-cell into the receiver half-cell was determined by periodically measuring the UV/Vis absorbance of the receiver solution. The following wavelengths were monitored: phenol - 268 nm, p-cresol - 276 nm, 2,4-dimethylphenol - 276 nm, and 2,4,6-trimethylphenol - 277 nm. An Agilent 8453

UV-Visible spectroscopy system with Agilent ChemStation software was used for all UV/Vis analysis. Calibration curves were used to convert the measured absorbance into the concentration of permeating species in the receiver half-cell.

Contact Measurements

A Tantec CAM-Micro contact meter was used to determine surface contact angles for the silane-treated membranes using the half-angle technique, as described in the user's manual. A ten microliter water droplet was dispensed for each measurement and four total measurements were recorded across the surface of the sample.

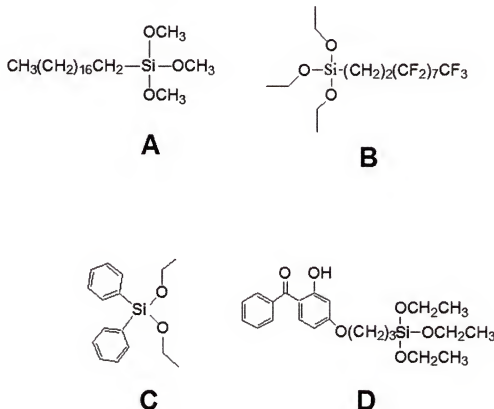
Results and Discussion

Transport with DiPS and DiPKS-Treated Membranes

Figure 3-1 shows the structure of the ODS silane from Chapter 2 and the three silanes used in this chapter for the surface modification of the membranes. Contact angle measurements with buffer were attempted on membranes modified with the DiPS and DiPKS silanes. A contact angle could not be determined because the droplet quickly spread across the surface and filled the pores of these membranes. This means the pores of membranes modified with DiPS and DiPKS would be filled with solution during transport studies.

Transport of the homologous series of permeate molecules from Chapter 2 were performed with DiPS and DiPKS-treated membranes (Figure 3-2). Almost no measured selectivity was achieved with the DiPS-treated membrane, while the DiPKS-treated membrane expressed low measurable selectivities. Interestingly, for the DiPKS-treated membrane, the magnitude of the fluxes of the permeate molecules followed the same trend seen for an unmodified nanoporous alumina membrane. For these membranes, the

flux of phenol was greatest and the subsequent fluxes were in the decreasing order of p-cresol, DMP, and TMP. This trend emphasizes the importance and influence of the hydrophilic hydroxyl and ketone moieties on the organic side-chain of the DiPKS silane. This influence was also seen in the quickly wetting of the membranes' pores by the aqueous buffer solution during contact angle measurements.



Despite the wetting of the pores and little to no expressed selectivity by the DiPS and DiPKS-treated membranes, the net fluxes exhibited considerable enhancement (Table 3-1). It was reported in Chapter 2, that an unmodified BP20 membrane displayed fluxes in the range of $0.3 \mu\text{moles cm}^{-2} \text{ hr}^{-1}$. Treatment with these silanes promoted an

enhancement of flux by a factor of almost three. This measured enhancement of flux points to an interaction and facilitation effect of the analytes by the silane-treated membrane pore walls.

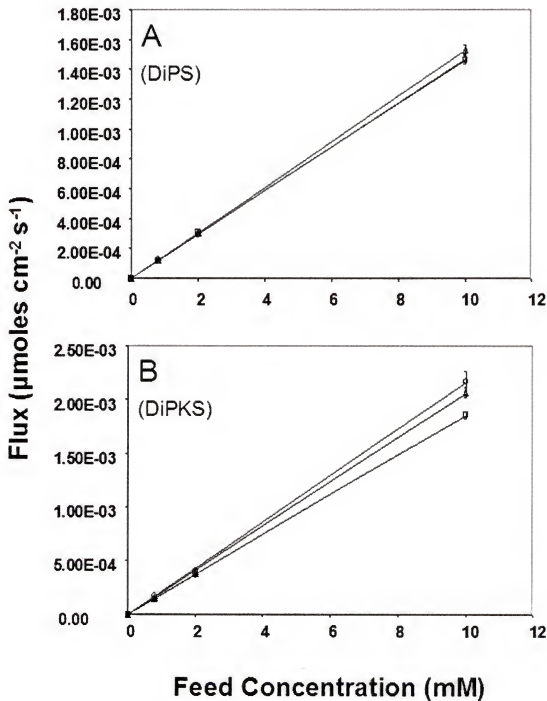


Figure 3-2. Transport with DiPS and DiPKS-treated membranes (\circ = Phenol, Δ = p-cresol, \square = DMP, \diamond = TMP).

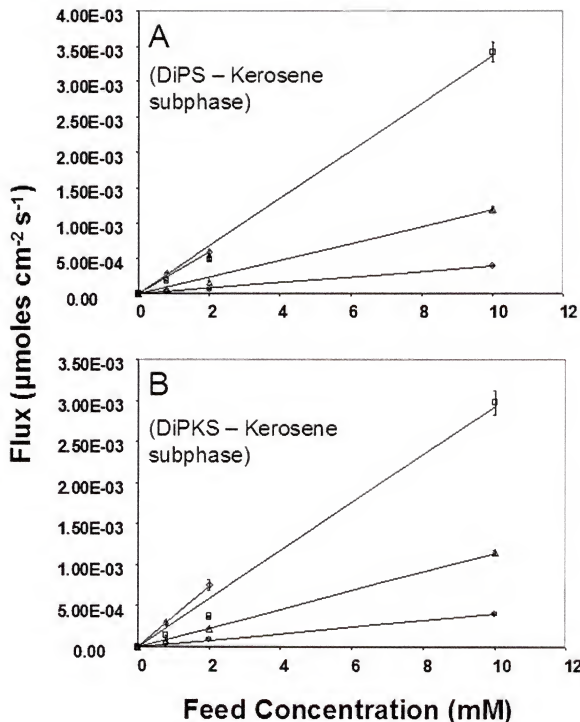


Figure 3-3. DiPS and DiPKS-treated membranes with a kerosene subphase (○ = Phenol, △ = p-cresol, □ = DMP, ◊ = TMP).

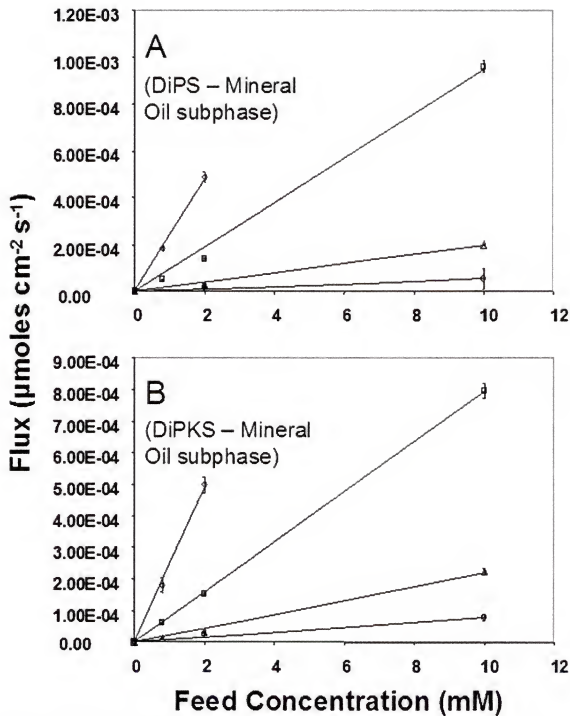


Figure 3-4. DiPS and DiPKS-treated BP20 membranes with a mineral oil subphase (○ = Phenol, Δ = p-cresol, □ = DMP, ◊ = TMP).

Table 3-1. Fluxes for DiPS and DiPKS-treated BP20 membranes, with and without the presence of a subphase (2mM feed concentrations).

Silane Modification	Subphase	Analyte	Flux ($\mu\text{moles cm}^{-2} \text{ hr}^{-1}$)	Selectivity (a)
DiPS	--	Phenol	1.05±0.01	1
		p-Cresol	1.10±0.02	1
		DMP	1.11±0.03	1
		TMP	1.09±0.02	1
	Kerosene	Phenol	0.23±0.02	1
		p-Cresol	0.62±0.02	2.7
		DMP	1.75±0.08	7.5
		TMP	2.1±0.1	8.9
	Mineral Oil	Phenol	0.06±0.01	1
		p-Cresol	0.11±0.01	2
		DMP	0.50±0.01	8.8
		TMP	1.76±0.08	31
DiPKS	--	Phenol	1.47±0.05	1
		p-Cresol	1.38±0.02	1
		DMP	1.33±0.02	1
		TMP	1.33±0.03	1
	Kerosene	Phenol	0.31±0.03	1
		p-Cresol	0.80±0.03	2.6
		DMP	2.2±0.1	7
		TMP	2.7±0.2	8.8
	Mineral Oil	Phenol	0.09±0.01	1
		p-Cresol	0.120±0.007	1
		DMP	0.55±0.02	6
		TMP	1.80±0.09	20

Figures 3-3 and 3-4 show the calculated fluxes versus feed concentrations for DiPS and DiPKS-treated membranes with a kerosene or mineral oil subphase. As in Chapter 2 with ODS, the DiPS and DiPKS silanes were able to stabilize the organic subphase within the pores for several days. When these results are compared to prior treatment with DiPS and DiPKS alone, we can see distinct and large measurable selectivities (Table 3-1). Further, if these values are compared to the ODS-treated membrane containing the same subphase (Table 2-4), the fluxes and selectivities are almost equivalent between the two cases. From this data we can draw two things. First, as implied earlier, the silane is necessary to stabilize the subphase within the pores of the membrane. Second, once a subphase is introduced into the pores of these nanoporous membranes, the transport process is dominated by partitioning into and out of the bulk solvent. The last statement is also supported by the bulk solvent partitioning studies and rates of transport of analytes into and out of the organic phases performed in Chapter 2. There it was shown the specie's flux through a subphase filled membrane depended on its rate of passage into and out of organic subphases.

Treatment of the membrane with DiPS or DiPKS did not provide any added advantage to ODS-treatment. Without the addition of a subphase there was enhancement of the flux of the permeate molecules but selectivity was almost indiscriminant. Addition of a subphase to these membranes caused them all to exhibit similar fluxes. This was due to transport being dominated by the partitioning of the analyte into and out of the bulk solvent.

Transport with CF₃S-Treated Membranes

For these studies, BP20 membranes were modified using the CF₃S fluorinated silane (Figure 3-1). After modification of the membrane with this silane, a contact angle of ~120° was measured against e-pure water. Unlike the DiPS and DiPKS-treated membranes, it was deduced the pores of CF₃S-treated membranes would not be flooded during the transport studies and would remain dry, much like the ODS-treated membranes.

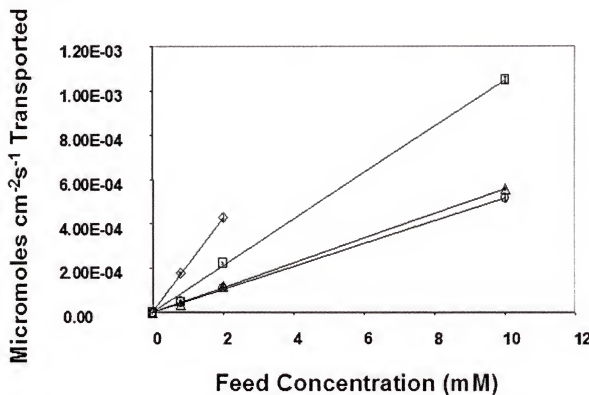


Figure 3-5. Transport with a CF₃S-treated BP20 membrane with increasing concentrations of analyte. (○ = Phenol, Δ = p-cresol, □ = DMP, ◇ = TMP).

Figure 3-5 shows transport experiments with the homologous series of permeate molecules over an increasing range of feed concentrations. Very similar to the results with the ODS-treated BP20 membranes, the recorded flux increases with the hydrophobicity of the permeate molecule being transported. However, with the CF₃S-

treated membranes a two-fold enhancement in flux was expressed for all the species. Nevertheless, due to the near equal magnitude of enhancement in flux for all the species, the calculated selectivities with CF_3S -treated membranes were almost equal to the ODS case (Table 3-2).

Table 3-2. Fluxes for a CF_3S -treated BP20 membrane and 2 mM feed concentrations.

Silane Modification	Analyte	Flux ($\mu\text{moles cm}^{-2} \text{ hr}^{-1}$)	Selectivity (a)
CF_3S	Phenol	0.40 ± 0.02	1
	p-Cresol	0.42 ± 0.03	1.1
	DMP	0.79 ± 0.02	1.9
	TMP	1.54 ± 0.05	3.8

Recalling from earlier, an ODS-treated membrane was shown to express a Langmuirian adsorption transport behavior for phenol. We wanted to determine if CF_3S -treated membranes would display a similar behavior. The flux of phenol through CF_3S -treated membranes was recorded as a function of increasing feed concentration (Figure 3-6). The plotted flux of phenol with the ODS-treated membranes began to plateau between 300 and 500 mM and the start of the influence of pore flooding was seen between 600 and 700 mM. With the CF_3S -treated membrane, the flux plateau was shifted to a higher concentration range (600 and 700 mM range) and evidence of pore flooding was never observed. To further support a lack of pore flooding at high feed concentrations, contact angle measurements were taken of the feed solution on the treated membranes. At the highest phenol feed solution of 700 mM, a contact angle of $\sim 110^\circ$ was recorded, signaling the pores were not in danger of undergoing flooding.

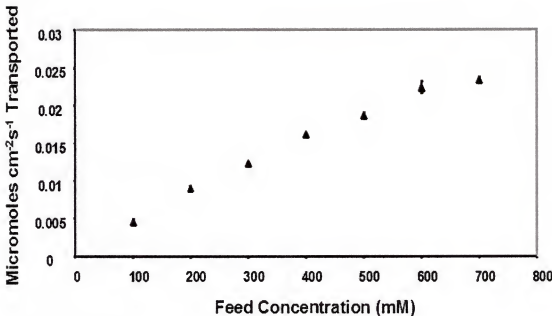


Figure 3-6. Flux versus increasing feed concentration of phenol with a CF_3S -treated BP20 membrane.

As in Chapter 2, the Langmuir equation can be written as Equation 2-7,

$$-J_x^{-1} = \left(\frac{L}{DC_{\max} K_L} \right) \frac{1}{[X_{aq}]} + \frac{L}{DC_{\max}} \quad (2-7)$$

and K_L could be solved for graphically. A best-fit line was calculated with an r^2 value of 0.9995, a y-intercept of $-11 \pm 2 \text{ }\mu\text{moles}^{-1} \text{ cm}^2 \text{ sec}^{-1}$, a slope of $-2100 \pm 300 \text{ }\mu\text{moles cm}^{-2} \text{ hr}^{-1}$ mM, and a calculated K_L value of 0.5 M^{-1} . Before it was found the K_L value for phenol with an ODS-treated membrane was larger (0.86 M^{-1}). Recalling, K_L is a measure of the hydrophobic driving force for adsorption of a species into a layer, then intuitively we can explain this difference. It would be predicted, that the greater the hydrophobicity of a species, the greater its K_L value with the ODS layer would be. In addition, predictions would show that changing the nature of the silane layer would also change the magnitude of K_L . When a species like phenol is presented with an alkyl layer (ODS) or a Teflon-like

layer (CF_3S), it would be expected to have a greater preference for the alkyl layer, which is reflected experimentally in our calculated K_L values.

Another way of looking at this concept is the lower the aqueous solubility of a species, the greater its K_L value with a hydrophobic layer would be. To explore this further, we selected p-cresol and aniline. The solubility values for p-cresol and aniline are 210 mM and 350 mM.³¹ Experimentally, in the pH 7 running buffer their solubilities were found to be between 150 and 180 mM for p-cresol and 350 and 400 mM for aniline. Recalling phenol reached its experimental solubility limit in solution between 700 and 750 mM, it would be predicted p-cresol would have the highest K_L value (in line with their aqueous solubilities) followed by aniline and then phenol.

Table 3-3. Contact angle measurements of p-cresol and aniline on ODS and CF_3S -treated membranes. *The contact angle of phenol solutions with the CF_3S -treated membranes only fell to a value of 110 ± 1 with the 700 mM solution.

	Concentration (mM)	Silane Modification	
		ODS	CF_3^*
Water	--	119.8 ± 0.5	120 ± 1
p-Cresol	30	118 ± 1	123 ± 2
	60	112 ± 1	119 ± 4
	90	95 ± 5	114 ± 4
	120	69 ± 15	107 ± 12
	150	47 ± 7	105 ± 3
	50	112 ± 3	128 ± 3
Aniline	100	118 ± 2	126 ± 1
	150	117 ± 2	121 ± 2
	200	117 ± 1	117 ± 2
	250	108 ± 1	119 ± 3
	300	100 ± 2	119 ± 3
	350	83 ± 5	112 ± 2

Table 3-3 shows the contact angle measurements for increasing solution concentrations of p-cresol and aniline on the surface of ODS and CF_3S -treated

membranes. The contact angles of p-cresol and aniline on ODS-treated membranes did not drop below 90° until solution concentrations of 120 mM for p-cresol and 350 mM for aniline. Unlike with the ODS-treated membranes, the contact angles of p-cresol and aniline on CF₃S-treated membranes did not drop below 100° at the highest solution concentrations of each species. The pores of porous membranes are expected to flood with solution if the surface contact angle is less than 90°.⁶²

In Chapter 2, it was also seen for a solutions whose contact angle dropped below 90° there was a sharp rise in flux on a flux versus feed concentration graph. As expected from the contact angle measurements, in the flux versus feed concentrations graphs, the CF₃S-treated membranes did not express any evidence of pore flooding (seen as a straight line relation) while the ODS-treated membrane did (seen as a loss of linearity, Figure 3-6 and 3-7). The loss of linearity was from 90 to 120 mM for p-cresol and from 300 to 350 mM for aniline.

Even though the pores of the CF₃S-treated membrane never flooded, we were not able to observe a Langmuirian plateau for p-cresol or aniline. Unfortunately for our experiments, the linear response of flux versus feed concentration was maintained through all feed concentrations of the analytes until their solution saturation points were reached.

An attempt was made to place kerosene and mineral oil subphases in the CF₃S-treated membranes and perform analogous experiments to the ODS, DiPS and DiPKS-treated membranes. However, the fluorinated membranes resisted wetting with the hydrocarbon solvents. Kerosene quickly leached from the pores, while mineral oil

beaded up on the surface, displaying a lack of wetting preference for the Teflon®-like coated membrane.

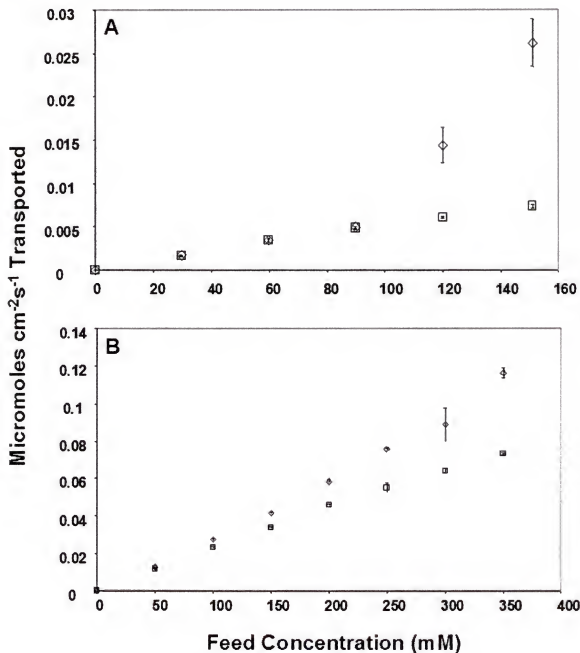


Figure 3-7. Flux of p-cresol and aniline with ODS and CF₃S-treated membranes. A) p-cresol, and B) aniline feed. (◊ = ODS-treated and □ = CF₃S-treated)

Conclusions

A group of three different silanes were selected to further study the influence of silane modification on the transport of the homologous series of permeate molecules. After treatment of BP20 membranes with DiPS or DiPKS silanes, little to no measurable selectivities were calculated, especially when compared to treatment with the CF₃S silane. The measured differences were mostly due to the quick flooding of aqueous solution into the pores of the DiPS and DiPKS-treated membranes and to the flood resistant pores of CF₃S-treated membranes. With respect to the bare BP20 membranes, DiPS and DiPKS silane-treatment increased the flux by approximately three-fold, even though their pores were completely flooded with buffer solution. The CF₃S-treated membranes, when compared to the ODS-treated membranes, promoted an almost two-fold increase in flux.

With the addition of a subphase (kerosene or mineral oil) to the DiPS and DiPKS-treated membranes, their transport properties were almost identical to the equivalent case with the ODS-treated membranes. These findings further support that transport through a membrane with a solvent subphase is dominated by analyte partitioning into and out of the solvent subphase that is present in the pores of the membrane. Similar experiments were attempted with the CF₃S-treated membranes. However, the placement of a subphase in the CF₃S-treated membranes could not be performed with either organic solvents due to a lack of proper wetting.

Much like the ODS-treated membranes, CF₃S-treated membranes expressed a Langmuirian adsorption-like transport behavior with increasing concentrations of a phenol feed solution. In contrast to the ODS-treated membranes, the CF₃S-treated

membranes did not undergo pore flooding and plateaued at higher feed concentrations of phenol. A predicted Langmurian behavior for p-cresol and aniline could not be observed with the ODS or the CF₃S-treated membranes. The ODS-treated membrane experienced pore flooding while the CF₃S-treated membrane displayed a linear relationship until the solution solubility of the analyte was exceeded.

CHAPTER 4
TRANSPORT RATE AND SELECTIVITY IN SILANE-TREATED NANOPORE
ANODIC ALUMINA MEMBRANES AND PH DEPENDANCE

Introduction

In Chapters 2 and 3 we investigated the transport of neutral species utilizing nanopore anodic alumina membranes. In Chapter 2 octadecyltrimethoxysilane (ODS) was used to modify the surface of these membranes. The pores of these membranes were then filled with an organic subphase (kerosene or mineral oil). In Chapter 3, a set of three different silanes were used for surface modification, diphenyldiethoxysilane (DiPS), 2-hydroxy-4-(3-triethoxysilylpropoxy)diphenylketone (DiPKS), and (heptadecafluoro-1,1,2,2-tetrahydrodecyl)triethoxysilane (CF_3S). In this chapter we return to the ODS-treated nanopore anodic alumina membranes (with and without subphases) and investigate their transport properties of species whose charge is dependant on solution pH.

Livingston et. al. have been studying the removal of aromatic species from wastewater for a number of years using a membrane based system.^{3,4,5,156} This system, named *MARS* for Membrane Aromatic Recovery System, utilized a permeable PDMS based nonporous membrane which divided two solutions of differing pHs. When species belonging to the phenol family were investigated they made the feed acidic and the permeate basic. In the case of aniline transport, the opposite pH ranges were used. We wanted to investigate the transport of protonatable analytes over a range of pH.

Based upon data obtained in Chapter 2 (where charged species are denied passage through an ODS-treated membrane) it was concluded that solution pH could be used to separate two species at a given pH, where one is neutral and the other is charged. Aniline, 2-nitrophenol, benzoic acid, and pyridine were selected for these studies. The structures and pK_a values of these species are given in Figure 4-1.

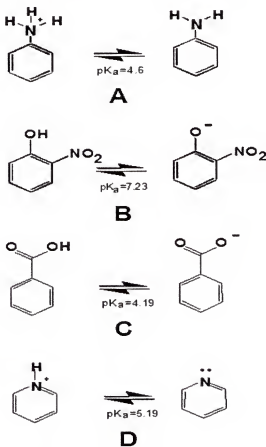


Figure 4-1. Structures and pK_a values of A) aniline, B) 2-nitrophenol, C) benzoic acid, and D) pyridine.

In Chapter 2 and 3 the flux of a permeate molecule through ODS-treated membranes was shown to be dependant on the hydrophobicity of the molecule and the feed concentration of the transported form. Interestingly, for the species selected for these studies there are two available states to each species in Figure 4-1, a neutral and

charged state. Therefore, it would be expected at low pHs there would be the greatest fluxes of 2-nitrophenol and benzoic acid through these membranes, while at high pHs aniline and pyridine would express their greatest fluxes. In order to predict and model the flux versus pH behavior it was thought we could use the calculated alpha values for each species.

The alpha value is defined as the ratio of the amount of a species in solution in the neutral state, $A_{neutral}$, divided by the total amount of that species in all states in solution, A_{total}

$$\text{Alpha} = \frac{A_{neutral}}{A_{total}} \quad (4-1)$$

Alpha has a value ranging from zero to one, where a value of zero indicates none of the species is in the neutral state and a value of unity indicates 100% of the species is in the neutral state. Figure 4-2 shows a plot of the calculated alpha values for aniline. Since by definition, the alpha curve is a representative plot of the concentration of the neutral state of aniline in solution we would also expect a plot of flux versus solution pH to possess a similar profile (Figure 4-2B). Based on the same rationale, we would expect pyridine to exhibit the same trend, and 2-nitrophenol and benzoic acid to exhibit the opposite trends.

The following experiments were performed to test these ideas. The concentration and separation of analytes based on these concepts were also performed.

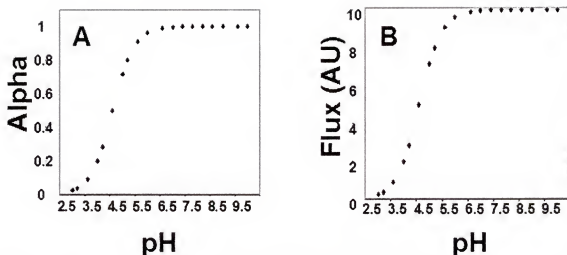


Figure 4-2. Calculated A) alpha values, and B) the expected flux trend for aniline based on a pK_a of 4.6.

Experimental

Materials

Alumina Anodisc® 47 filter membranes (60 μm thick, 47 mm diameter, and ~50% porosity) were obtained from Whatman. BP20 membranes were selected for these studies. Sodium acetate, citric acid, sodium bicarbonate, N-(1,1-Dimethyl-2-hydroxyethyl)-3-amino-2-hydroxypropansulfonsyre (AMPSO), aniline, 2-nitrophenol, pyridine, benzoic acid, hexane, tetrahydrofuran, kerosene, light mineral oil, absolute alcohol, sodium acetate, NaH_2PO_4 , and hexagonal polystyrene weighing dishes were used as received from Fisher Scientific. Octadecyltrimethoxysilane (ODS) was obtained from Gelest and used as received. Extra fast setting epoxy was obtained from Cole Parmer and used as instructed. Purified water was prepared by circulating house-distilled water through a Millipore Milli-Q water purification system ($>17 \text{ M}\Omega \text{ cm}^{-1}$).

Membrane Modification

The membranes were cleaned and modified in accordance with the protocol in Chapter 2.

Transport Experiments

The fabrication of the membrane assembly and subphase modification methods were performed as outlined in Chapter 2. The flux of each analyte molecule was determined in the following manner. The analyte molecule was introduced into the feed side of the u-tube cell, and the permeate side was monitored for its appearance with UV/Vis spectroscopy. In all, four different buffers were used: citric acid for a pH of 3 to 6, sodium phosphate for a pH of 7, AMPSO for a pH of 9, and sodium bicarbonate for a pH of 10. All four buffer systems had a concentration of 50 mM. The pH 7 NaH₂PO₄ buffer was used in the permeate side of all experiments except in the concentration and separation studies. The analyte feed concentrations used were 800 µM, except in the concentration and separation studies where they were 100 µM.

The flux of the permeating species from the feed half-cell through the membrane and into the receiver half-cell was determined by periodically measuring the UV or visible absorbance of the receiver solution. The following wavelengths were used: aniline-230 nm, pyridine-256 nm, and 2-nitrophenol-279 nm. An Agilent 8453 UV-Visible spectroscopy system with Agilent ChemStation software was used for all UV/Vis analysis. Calibration curves were used to convert the measured absorbance into the concentration of permeating species in the receiver half-cell.

Results and Discussion

PH Dependant Transport Through ODS-Treated Membranes

The effect of the feed solution pH on the transport of 2-nitrophenol and pyridine was performed. ODS-treated and ODS-treated membranes with a kerosene or mineral oil subphase were used.

With the three membrane systems used, pyridine and 2-nitrophenol each expressed trends predicted by their respective alpha curves (Figures 4-3). The inflection point of each curve was located at each species K_a value, 7.2 for 2-nitrophenol and 5.2 for the protonated form of aniline. When kerosene was used as the subphase, the maximum flux for pyridine was approximately equal to 2-nitrophenol's. However the ODS-treated membrane and ODS-treated membrane, with a mineral oil subphase, differed from pyridine to 2-nitrophenol. Perhaps this is due to a difference in the rate of passage of aniline and 2-nitrophenol into and out of the mineral oil subphase. Identical transport studies were performed with benzoic acid and aniline and similar results were obtained (Figure 4-4).

As graphed in Figure 4-3 and 4-4, it is difficult to compare these experimental flux curves to their respective alpha curves, making it hard for a conclusion to be directly drawn. The ambiguous nature of this comparison is a direct result of the arbitrary magnification of the respective y-axis for the alpha curves of each analyte. In order to derive a more direct comparison, the data was plotted as the log of flux versus feed pH and the log of the alpha values versus pH (Figure 4-5 and 4-6).

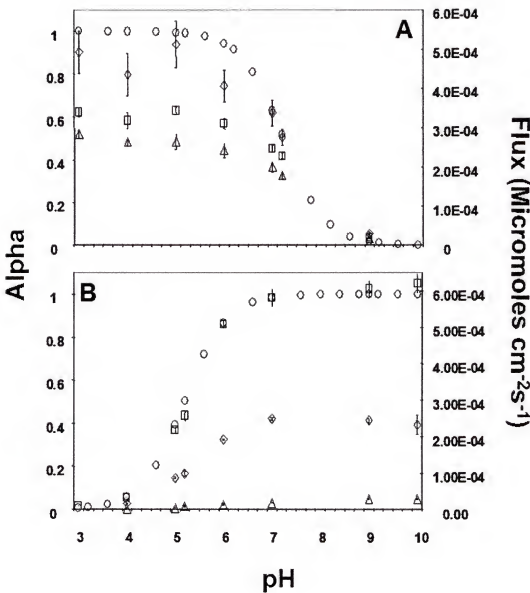


Figure 4-3. Calculated alpha and measured flux versus feed pH for A) 2-nitrophenol and B) pyridine. (□ = ODS, ◊ = kerosene subphase, Δ = mineral oil subphase, and ○ = alpha calculation).

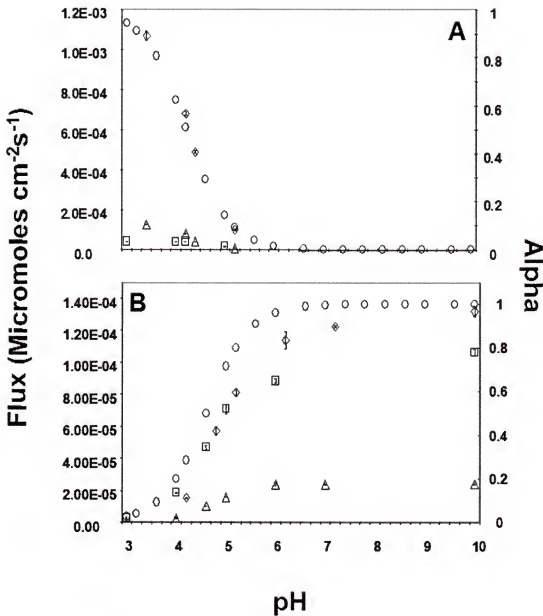


Figure 4-4. Calculated alpha and measured flux versus feed pH for A) benzoic acid and B) aniline. (\square = ODS, \diamond = kerosene subphase, Δ = mineral oil subphase, and \circ = alpha calculation).

Each group of analyte curves graphed was shifted to overlay at the pH yielding the greatest flux (pH 3 for 2-nitrophenol and benzoic acid and pH 10 for pyridine and aniline). In this way, a more direct comparison could be made.

For a particular analyte each group of curves closely follows its respective alpha curve. Showing the alpha curve for each species can be used as a model for the theoretical prediction of the transport behavior of each species through these membranes. This close correlation indicates, over this range of pHs, the flux of each species is directly related to the amount of neutral species in solution. This is not surprising based on the work and results obtained in Chapter 2 and 3.

Since the alpha value is the mole fraction of an analyte in the neutral state, it would be expected at the extreme pHs (where the alpha value is extremely low) a complete *shut-off* of transport would be observed. The benzoic acid experimental curves (Figure 4-6A) showed a complete *shut-off* of transport above a pH of 6. In the 2-nitrophenol case, *shut-off* was not seen until a solution pH of 10. Aniline and pyridine do not seem to express a pH at which a complete *shut-off* is seen for any of the membranes.

In Figures 4-3 and 4-4, it was seen the flux of pyridine and 2-nitrophenol increased with rising solution pH, where benzoic acid and aniline exhibited the opposite response to pH. While Figures 4-5 and 4-6 seem to show a closer correlation between the experimental fluxes and the calculated alpha values, it still is not clear from these figures if there is the expected linear relationship between alpha (amount of neutral analyte) and the respective flux, which was shown in Chapter 2.

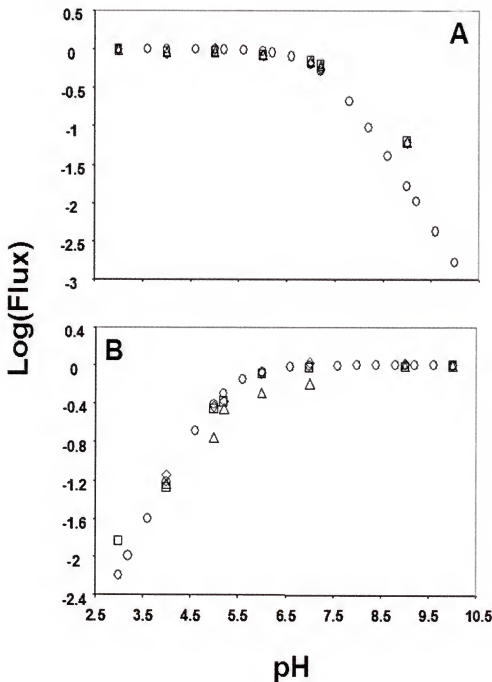


Figure 4-5. Log(Flux) versus pH of feed solution using a BP20 membrane with A) 2-nitrophenol and B) pyridine (\square = ODS, \diamond = kerosene subphase, Δ = mineral oil subphase, and \circ = alpha calculation).

Note: Each graph has been shifted to align with its respective alpha curve at its zero point.

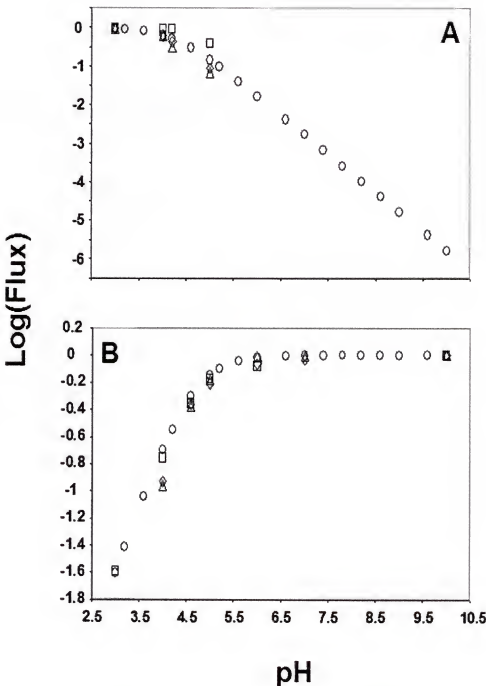


Figure 4-6. Log(Flux) versus pH of feed solution using a BP20 membrane A) benzoic acid and B) aniline (\square = ODS, \diamond = kerosene subphase, Δ = mineral oil subphase, and \circ = alpha calculation).

Note: Each graph has been shifted to align with its respective alpha curve at its zero point.

Figure 4-7 can be used to explain the expected linear relationship by graphing the data in a third way. At a given solution concentration of the neutral species, a flux is expected, x , and at a concentration twice that a flux of $2x$ would be expected. Thus, when the experimental fluxes are graphed versus the calculated solution concentrations of the neutral forms of each analyte at a given pH, a linear relationship should be observed (Figure 4-8 and 4-9). In these figures a very similar linear relationship is seen between the flux and feed concentration . This similar relation was also seen in the graphs in Chapter 2 and 3.

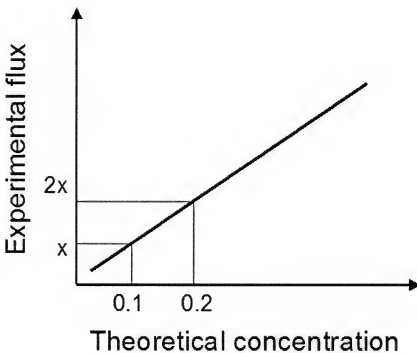


Figure 4-7. Linear relationship between expected flux and neutral species concentration.

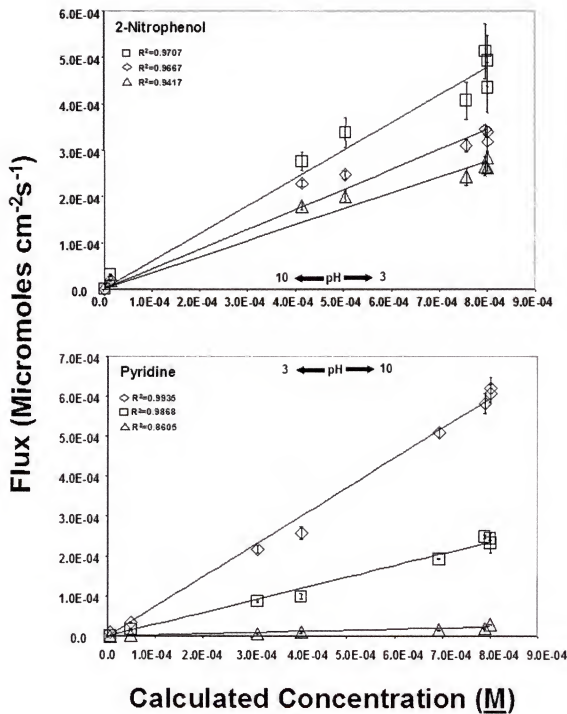


Figure 4-8. Correlation of the calculated concentration (based on calculated alpha) and the experimental flux at a given pH. (An ODS-treated BP20 membrane, ◊ = ODS, □ = kerosene subphase, △ = mineral oil subphase).

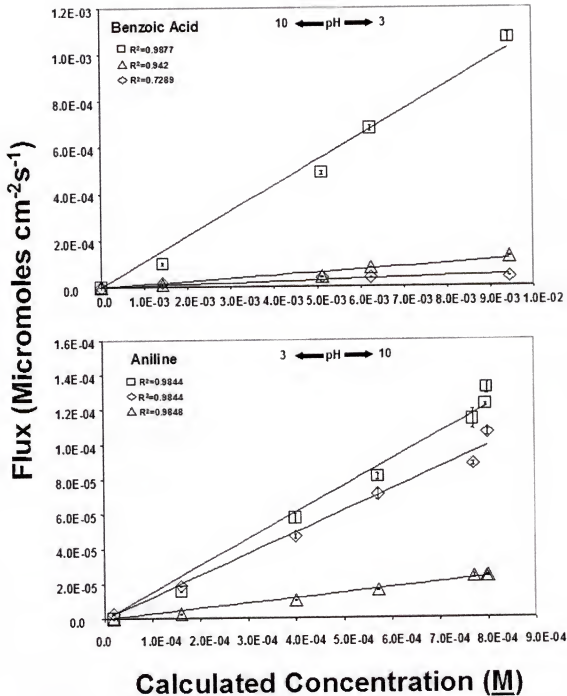


Figure 4-9. Correlation of the calculated concentration (based on alpha) and experimental flux at a given pH (An ODS-treated membrane with a 10 mM and 800 μmole feed for benzoic acid and aniline, respectively. An ODS-treated BP20 membrane, \diamond = ODS, \square = kerosene subphase, Δ = mineral oil subphase).

It would be ideal if we could obtain a complete and sharp flux *shut-off* at reasonable and predictable pHs (according to a species pK_a). This would allow us to perform precise concentration and very selective separation studies based on the pK_a's of the analytes present in solution.

Solution pH Based Concentration and Separation of 2-Nitrophenol and Pyridine

Based on the results obtained earlier it seemed plausible a species could be concentrated using the ODS-treated membrane and the ODS-treated membrane with either a kerosene or mineral oil subphase membrane based solely on solution pH. Two-nitrophenol was selected for these concentration studies. Two-nitrophenol is predominantly in the neutral state in a solution at a pH of 3 and in a negative one state at a pH of 10 (Figure 4-1). It can be predicted, if 2-nitrophenol is placed in a permeation cell with a pH 3 solution in one side and a pH 10 in the other, then 2-nitrophenol would concentrate in the pH 10 side of the permeation cell.

Initially a 100 μM solution of 2-nitrophenol was introduced on both sides of the permeation cell and the change in concentration versus time was monitored (Figure 4-10). At first glance it appears these membranes are able to transport 2-nitrophenol against the concentration gradient. In the pH 3 side of the permeation cell (at time zero) the concentration of 2-nitrophenol in the neutral state is ~100 μM. After 24 hours, there is at most a concentration of a few μmolar which is just below the detection limit of the instrument. In the pH 10 side of the cell, with a final concentration of 200 μM, there is a calculated concentration of the neutral state of 2-nitrophenol of ~0.34 μM. Thus, when the concentration gradient was examined (with respect to the neutral species) that was extending from the pH 10 side of the u-tube to the pH 3, it was effectively zero. There

was a value on one side of the membrane of at most a few μM and on the other side a calculated value of 0.34 μM . These facts make the concentration of 2-nitrophenol possible a sink for 2-nitrophenol is formed in the pH 10 side of the permeation cell due to deprotonation.

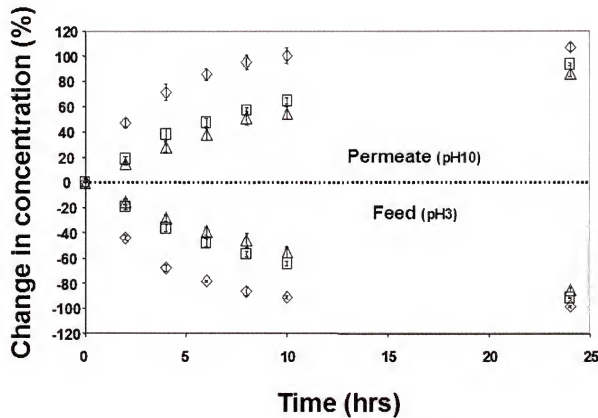


Figure 4-10. Percent change in the concentration of 2-nitrophenol in the feed and permeate versus time using a BP20 membrane (\square = ODS, \diamond = kerosene and Δ = mineral oil subphase).

In the concentration studies the ODS-treated membrane with the kerosene subphase exhibited the greatest flux, achieving nearly 100% concentration after about 10 hours. The ODS-treated membrane outperformed the ODS-treated membrane with a mineral oil subphase. These results are in agreement with the recorded transport data earlier from this chapter and from Chapters 2 and 3. However, after nearly 24 hours all membranes obtained a concentration value of near 100%.

Competitive Separation Studies

We wanted to show two analytes could be separated based on their pK_a values using only on solution pH. Two-nitrophenol and pyridine were selected for these studies. Two-nitrophenol and pyridine were introduced into the feed side, which was at a pH of 3. ODS-treated membranes and ODS-treated membranes with a kerosene or mineral oil subphase were used. The feed and permeate (at a pH of 10) were monitored versus time (Figure 4-11 through 13).

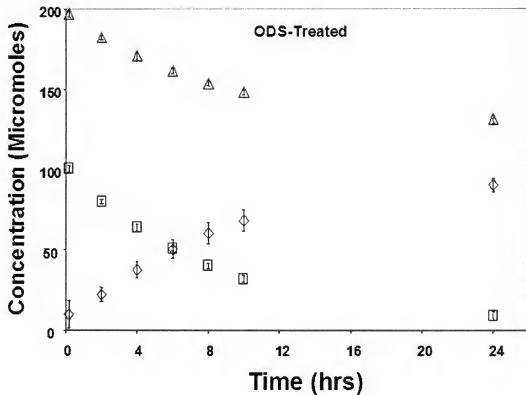


Figure 4-11. Separation of 2-nitrophenol and pyridine using a BP20 membrane (\diamond = 2-nitrophenol in the pH 10 side, \square = 2-nitrophenol in the pH 3 side, Δ = pyridine in the pH 3 side).

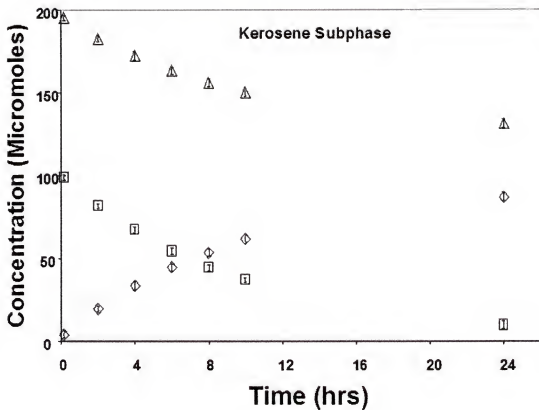


Figure 4-12. Separation of 2-nitrophenol and pyridine using a BP20 membrane (\diamond = 2-nitrophenol in the pH 10 side, \square = 2-nitrophenol in the pH 3 side, Δ = pyridine in the pH 3 side).

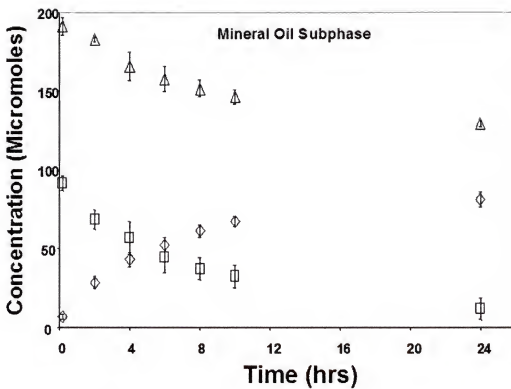


Figure 4-13. Separation of 2-nitrophenol and pyridine using a BP20 membrane (\diamond = 2-nitrophenol in the pH 10 side, \square = 2-nitrophenol in the pH 3 side, Δ = pyridine in the pH 3 side).

Similar results were obtained with the three membranes used. The concentration of 2-nitrophenol in the pH 3 feed decreased with time, while it steadily increased in the pH 10 permeate. However, no pyridine could be detected in the permeate side over the entire course of the experiments. These results were not surprising based on previous results and those seen in Figure 4-9. However, what was not originally expected was the apparent decrease of pyridine concentration in the pH 3 feed of the cell. Yet, this apparent decrease is easy to explain. The absorbance peak of pyridine and 2-nitrophenol slightly overlap in a pH 3 solution. So, the pyridine peak effectively sits atop of the absorbance peaks of 2-nitrophenol, and as the concentration of 2-nitrophenol decreases with time, the pyridine peak also decreases. This is supported by the similarity of the time curves of pyridine and 2-nitrophenol in the pH 3 side of the permeation cell and no appearance of pyridine in the pH 10 side.

Conclusions

It was shown the transport of a deprotonatable species with an available neutral and a charged state could be modeled by their calculated alpha curves. Aniline, pyridine, benzoic acid, and 2-nitrophenol transported through bare ODS, and ODS-treated membranes with a kerosene or mineral oil subphase were all shown to obey the behavior predicted by their calculated alpha curves.

Using these membranes and solution pH, it was possible to concentrate 2-nitrophenol, transporting it against an apparent concentration gradient. The concentration rates of the membranes, from fastest to slowest, were a membrane with a kerosene subphase, the ODS-treated membrane, and an ODS-treated membrane with a mineral oil subphase. However, after 24 hours all three membranes achieved a concentration value

of nearly 100%. Finally, it was shown 2-nitrophenol and pyridine could be separated based on solution pH.

CHAPTER 5

METHOD DEVELOPMENT FOR THE PRODUCTION OF POLYMERIC REPLICA MEMBRANES OF TRACK-ETCH AND NANOPOROUS ANODIC ALUMINA MEMBRANES

Introduction

Separation membranes can be perceived as thin phases through which the species of interest are intended to controllably traverse. The rate of passage of molecules may depend on physical differences in size and, on specific or non-specific interactions between the molecules and the membrane. The Martin group has researched all such cases.^{112,114,115,118,119,126,157} The two families of membranes that were used for these studies were polycarbonate track-etch and nanoporous anodic alumina membranes.

Polycarbonate track-etch membranes are commercially available in a limited number of pore sizes, ranging in pore diameter from 10 nm to 10 μm .³¹ These membranes are quite marketable because they possess a high chemical and solvent resistance and an excellent mechanical stability and toughness.^{21,31} The main disadvantages of the track-etch membranes, are porosities less than 8%, limited commercial substrate materials and pores with a surface intersection angle of 30 to 35 degrees.²¹

Nanoporous anodic alumina membranes are porous films composed of aluminum oxide. Their primary advantages over the track-etch membranes are a porosity as high as 50%, tunable pore diameters (from 10 to 250 nm), low pore size distribution and tortuosity, high pore orientation, and thicknesses from a few nanometers to over 300 μm .^{32,33,34,35,36,37,38,39} The main disadvantage of nanoporous anodic alumina membranes

are they suffer from a low threshold for brittle fracture and membrane etching occurs at pHs below 4.7 and above 9.

The focus of the work here was to derive a method for the production of a new type of membrane. Ideally, this new membrane would possess the combined advantageous properties of the track-etch and nanoporous anodic alumina membranes. The production of this new type of membrane centered on formation of a mold around nanoporous anodic alumina membranes and their replication. Two mold and membrane replication techniques were derived for this project. They are both based on the process of using a material to fill the pores of the nanoporous anodic alumina membrane, encasing it to form a mold and then, after a series of steps, replacing the membrane with a polymeric material. The methodology of these techniques were initially tested and proven with the track-etch family. Track-etch membranes were used because of their lower porosities and thicknesses, making their replication easier and more amiable to method validation.

The synthesis of a nanometer sized structures inside the pores of nanoporous membranes and filling the pores with a material has been previously performed within the Martin group. Prior areas of exploration have been the production of gold nanoparticles,^{158,159} metal microtubules,¹⁶⁰ organic fibrils,^{161,162} metallic fibrils,¹⁶³ semiconductor fibrils¹⁶⁴ and the fabrication of polymeric microcapsules.¹⁶⁵

Numerous other groups have performed similar experiments. More relevant to our work here is the growth of nickel wires (which was conducted in this work). The nickel was used to fill the pores of track-etch¹⁶⁶ membranes and to image the structure of the pores after the removal of the membrane. Nickel nanoparticles and nanorods have

also been deposited in nanoporous anodic alumina membranes.^{167,168} After deposition, they could imagine the structures of these nano materials and investigate their magnetic properties.

Not only have other groups deposit nanostructures within the pores of these membranes, they have also explored their replication. Dobrev, et. al. explored the replication of track-etch membranes. They showed they could fabricate a thin metallic replica of track-etch membranes via a one-step¹⁶⁹ or two-step method.¹⁷⁰ However, the replica membranes they were able to produce were limited to conductive materials and all had thicknesses under 15 μm . Using a two-step replication process, Masuda et. al. fabricated nickel, cadmium sulfide, platinum, gold, titanium oxide, and palladium replicas of nanoporous anodic alumina membranes.^{171,172,173,174,175,176,177} Similar techniques were also used to fabricate an organically modified silica¹⁷⁸ and cobalt replica¹⁷⁹ of nanoporous anodic alumina membranes. However, in each case the fabricated replica membranes were less than 10 μm in thickness. In the end, all of the discussed replication methods effectively replaced one brittle membrane with another.

The ideas proposed and goals set are unique and will be of great use to the fields of passive and active separation and to the scientific community as a whole.

Experimental

Materials. Whatman Anodisc® filter membranes (200 nm pore diameter, 60 μm thickness, 47 mm diameter, and ~50% porosity by volume), concentrated nitric acid, 6 M sodium hydroxide, nickel (II) sulphate hexahydrate, sodium hypophosphite, dimethylamine borane, ammonium chloride, boric acid, and methylene chloride were used as received from Fisher Scientific. Polycarbonate track-etch membranes (6 to 10

μm in thickness, 30 nm to 10 μm pore diameter) were used as received from Poretics. Polyethylene pellets (M_w 15000) from Sigma-Aldrich and polystyrene (M_w 250000) from Acros were used as received. A Hummer 6.2 (Anatech LTD) was used to sputter gold at 60 mTorr and 15 mA for 5 minutes. An Arbin Mstat 4 system was used for electrochemical applications. Purified water ($>17\text{M}\Omega\text{cm}^{-1}$) was prepared by passing house-distilled water through a Millipore Milli-Q water purification system. A JEOL JSM6400 SM scanning electron microscope (SEM) with Energy-Dispersive Spectroscopy (EDS) capabilities was used for sample analysis.

Replication Process Based on a Polymeric Mold. A four-step replication process of nanoporous anodic alumina membranes was derived using a polymer as the molding material. First, the membrane was placed in a container with the polymeric material and the sample was heated under vacuum (~28" Hg) until the polymer melted completely and covered the membrane. Then the vacuum was released and heating discontinued. Second, the alumina membrane was removed from the mold by dissolution in 6 M solution of sodium hydroxide under sonication for 24 hours. Third, a polymeric material possessing different chemical properties than the first material was introduced into the mold. Finally, the mold was removed with an appropriate solvent. For example, if the mold was polystyrene and the membrane material was polyethylene, the mold could be removed using methylene chloride. Imaging was performed at each step using SEM to weigh the level of success for this method.

Replication Process Based on a Nickel Mold. Four replication routes using nickel deposition were explored. The basic steps of these replication processes were similar to

the polymeric mold method with the addition of one step. Nickel electroless and electrochemical deposition techniques were utilized in these methods.

The overall goal of the first three methods was to completely encase the membrane in a nickel mold. This became dubbed the *complete* mold method. The first method was based on the electrochemical deposition of nickel using: 180 g/L Ni(II)SO₄, 8 g/L NH₄Cl, 30 g/L Boric acid.¹²² To do this, either a track-etch polycarbonate or a 200 nm pore diameter (CP200) membrane was selected for replication. Then, a thin layer of gold was sputtered on one face of the membrane to render the entire surface electrically conductive. Next, the sputtered membrane was fashioned into an electrode with a 0.75" diameter area exposed for deposition. This electrode was then placed in an electrochemical plating bath for metal deposition with a platinum anode. A constant potential of 2.4 V was applied for 48 hours versus a platinum anode and the membrane electrode assembly. The final steps of this process entailed mold formation, membrane removal, introduction of a polymeric material, and removal of the mold.

The removal of the template membrane depended on which porous membrane was selected for replication. If a polycarbonate template membrane was used, it was dissolved using excess amounts of methylene chloride under sonication for 24 hours. If a CP200 membrane was used, then a solution of 6 M sodium hydroxide was used for dissolution under sonication for 24 hours.

Next injection of a polymeric membrane material was performed with an in-house vacuum chamber. The mold (after dissolution of the membrane) was placed with the polymer to be injected in the vacuum chamber and a vacuum was applied (~28" Hg). After the establishment of a stable vacuum, the polymer was heated to its melting point

and the vacuum was slowly released. Releasing the vacuum initiated injection of the melt into the mold due to a pressure difference across the polymeric melt. This pressure difference was a result of atmospheric pressure above the melt and a vacuum inside the mold below the melt. After allowing the sample piece to return to room temperature, the replica membrane was recovered from the mold by dissolving the nickel mold in a 10% nitric acid solution (V/V) under sonication for 12 hours.

The next two methods were based on the electroless deposition of nickel using either nickel chloride (42g/L), sodium hypophosphite (24g/L), sodium citrate (45g/L), and ammonium chloride (30g/L) or nickel sulfate (20g/L), ammonium chloride (15g/L), dimethylamine borane (3g/L), ammonium citrate (12g/L), and 2-mercaptobenzothiazole ($2E^{-4}$).^{122,124} The Martin group has a long background with electroless deposition into nanoporous membranes, having electrolessly deposited gold for numerous years.^{17,112,113,115,118,157} This previous experience was used here for solution selection and troubleshooting. However, before electroless deposition could be performed, nickel had to be electrochemically deposited for ten minutes using the method described above. Once an accessible nickel layer was established, introduction of the electroless deposition solutions promoted further nickel deposition on this base layer.

The fourth nickel deposition method, dubbed the *incomplete* mold method, closely resembled the electrochemical deposition method described previously. The only difference was that once electrochemical plating of nickel achieved breakthrough on the unspattered surface of the template membrane, the deposition was ceased. This was discernible because of the intense reflective property of nickel, making it easily visible on

the surface. The end result was a membrane with a nickel film on one side and nickel wires filling the pores.

For all the nickel based mold methods mentioned above, imaging was performed at each step using SEM to weigh the level of success for these methods.

Results and Discussion

Selection of Mold Material

Two replication methods were derived for this work (Figure 5-1). These methods (the *complete* and *incomplete* mold methods) involve the fabrication of a mold into and around the original template membrane to differing degrees. After mold fabrication, the template membrane was removed, leaving a free-standing mold. Since the pore diameters of the original membrane are within the nanometer scale regime, the molds will also have structures in the nanometer regime. To avoid mechanical failure of the mold, it was important to select a material possessing suitable mechanical properties on the same scale. Polymers (polyethylene and polystyrene) and nickel metal were explored as molding materials.

Polymeric Mold Material. The materials selected for the replication process using a polymeric mold were polyethylene $M_w=4000$ (PE4000) and polystyrene $M_w=250000$ (PS250000). By processing the polymeric melt under a vacuum, a mold could be cast around a CP200 membrane. Samples were collected and prepared for SEM analysis after solidification of the polymeric melt.

Figure 5-2 shows SEM micrographs of a PE4000 mold after the dissolution of the CP200 membrane. Numerous interconnecting “ravines” and “crevices” are seen crisscrossing the polymeric membrane’s surface (Figure 5-2A). At higher

magnifications, it is apparent these observed morphologies are a result of a lack of a mechanical stability of the PE4000. The polyethylene nanorods were able to remain intact, but they were unable to remain standing and parallel to one another after the removal of the alumina template membrane. The polymeric nanorods are seen leaning onto adjacent rods. This is a common problem for nanostructures with high aspect ratios¹⁶⁷ (height-to-width ratio). The polymeric nanorods produced here are 200 nm in diameter and 60 μm in length, for a calculated aspect ratio of 300. Thus, it was not completely surprising these relatively soft nanorods were unable to remain standing.

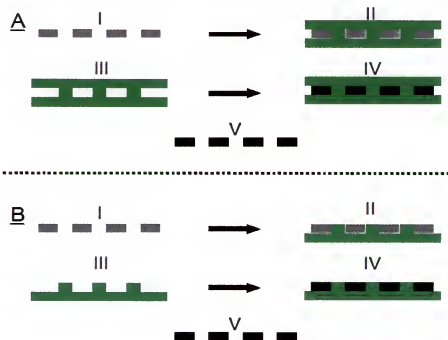


Figure 5-1. Membrane replication methods. A) The *complete* mold method: I) Alumina membrane, II) formation of the mold around the membrane, III) membrane is removed from the mold, IV) a new material is injected into the mold, and V) the mold is removed. B) The *incomplete* mold method.

In an attempt to move away from the softer polymers, the heavier and harder PS250000 was used in place of the PE4000. Even though PS25000 has a higher melt viscosity,³¹ it still could be used to produce a *complete* mold (Figure 5-3). PS250000 not

only fully encased the CP200 membrane, it also was shown to completely fill its pores (Figure 5-3C). However, much like the PE4000 molds, upon removal of the CP200 membrane, the mold still could not retain its integrity (Figure 5-4).

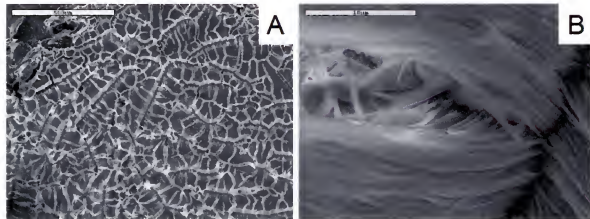


Figure 5-2. Surface SEM micrographs of a PE4000 mold of a CP200 membrane. One surface of the mold was mechanically polished away followed by dissolution of the alumina membrane (scale bars 500 μm and 10 μm respectively).

We found when either PS250000 or PE4000 were used as molding materials, the mold failed to maintain its integrity after removal of the template membrane. Failure was usually manifested as the polymeric nanowires bending to the point of touching their neighbors. A new mold material had to be found that would not undergo failure after removal of the template membrane. Nickel metal was investigated for the purpose of molding material due to its high melting temperature, toughness, hardness, and relatively low cost.¹²² However, because of its higher melting temperature it could not be introduced into the mold in the same manner as the polymeric materials.

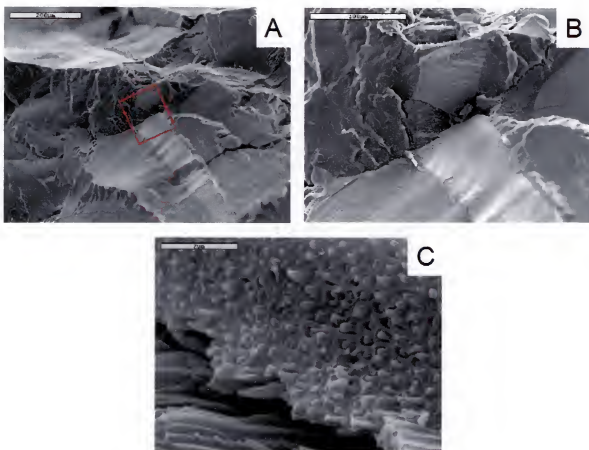


Figure 5-3. SEM micrographs of a fracture surface of a CP200 membrane molded with PS250000. A) Cross-section of the molded membrane. Red square denotes the location of the membrane and the location of the higher magnifications B) and C) (scale bars 200 μm , 100 μm and 2 μm respectively).

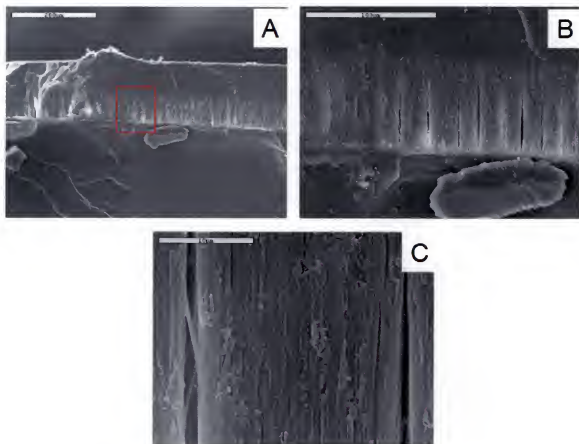


Figure 5-4. SEM micrographs of a fracture surface of CP200 membrane molded with PS250000 after the dissolution of the membrane. A) Cross-section. Red square denotes prior location of the membrane and indicates the higher magnifications B) and C) (scale bars 200 μm , 100 μm and 10 μm respectively).

Nickel Metal Mold Two different recipes were selected for the electroless deposition of nickel: I) 42 g/L nickel chloride, 24 g/L sodium hypophosphite, 45 g/L sodium citrate, and 30 g/L ammonium chloride (Referred to as NiSI, Figure 5-5) and II) 20 g/L nickel sulfate, 3 g/L dimethylamine borane, 12 g/L ammonium citrate, 15 g/L ammonium chloride, and $2E^{-4}$ 2-mercaptobenzothiazole (Referred to as NiSII, Figure 5-6). Utilizing either deposition solution, it was found nickel was not uniformly deposited within the pores of the membrane.

It is known that $H_{2(g)}$ is readily released during the electroless deposition process of nickel using these solutions.^{122,124} It was believed non-uniform deposition within the pores was due to the generation of hydrogen gas. The observed morphologies could be a manifestation of nickel growth around the entrapped hydrogen gas. Or perhaps, the evolution of hydrogen gas during deposition dislodged nickel seed crystals and pushed them up the pore where they autocatalytically nucleated the formation of new nickel islands on the pore wall.

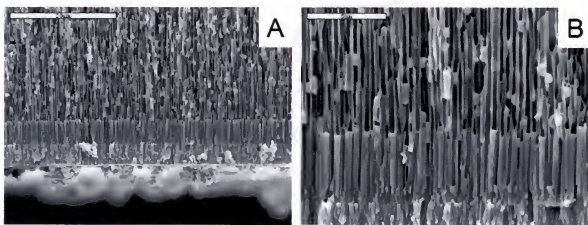


Figure 5-5. SEM micrographs of a cross-section of a CP200 membrane with electrolessly deposited nickel metal. Deposition with NiSI solution for 3 days (scale bars 20 μm and 5 μm respectively).

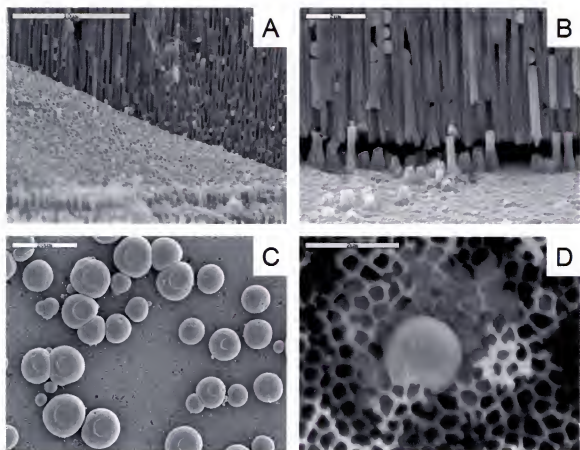


Figure 5-6. SEM micrographs of the cross-section of a CP200 membrane with electrolessly deposited nickel metal. Deposition with the NiSII solution for 3 days (scale bars 10 μm , 2 μm , 20 μm , and 2 μm respectively).

After a reaction time of three days, both procedures produced very short nickel nanorods at one end of the membrane and scattered nickel nanoparticles through the length of the membranes pores. Presented with no feasible way to prevent the non-homogeneous deposition of nickel, we turned to the electrochemical deposition of nickel.

A *complete* mold was electrochemically grown using a CP200 membrane (Figure 5-7). Not only was there an intimate contact between the nickel mold and the membrane, but also there was uniform growth of the nanowires and complete filling of the pores with nickel. Based on these SEM micrographs, electrochemical deposition of nickel seemed a more viable avenue to be pursued.

Before replication was attempted on the nanoporous anodica alumina membranes, it was first performed with the track-etch membranes. Nanoporous anodic alumina membranes possess a porosity of ~50%³¹ while track-etch membranes have porosities less than 8%.^{21,31} Commercially, anodic alumina membranes are available with a maximum pore size of 200 nm, while track-etch membranes are available with pores as large as 10 μm . Mostly due to their larger range of pore diameters, after comparing these two families of membranes, track-etch membranes were thought to be an ideal surrogate for investigating the nickel based electroplating and replication method. It was reasoned this should make it easier to scrutinize the limits of this replication method.

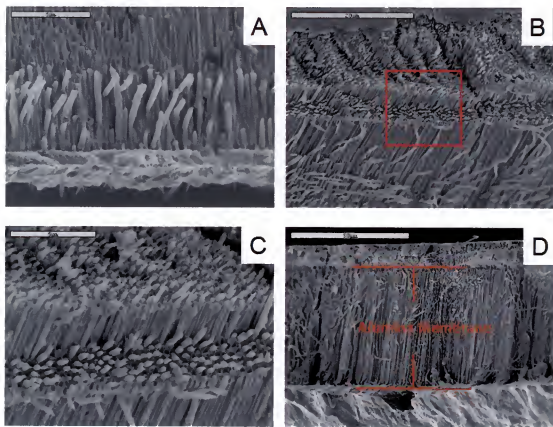


Figure 5-7. SEM micrographs of a CP200 membrane during various stages of the *complete* molding method. A) Cross-section at an early stage of mold production, B) fracture surface of the mold near completion, C) higher magnification of denoted area in B), and D) a cross-section at the completion of the molding process (scale bars 5 μm , 20 μm , 5 μm , and 50 μm respectively).

Complete Mold Method Applied to Track-Etch Membranes

As depicted in Figure 5-1, the first step of the replication process was to form a mold around the selected membrane. Several track-etch membranes with differing pore diameters were selected and nickel molding was performed (Figure 5-8).

Experimentally, it was seen nickel molds could be successfully grown around membranes with pore diameters as small as 30 nm. When the upper and lower layers of a mold were removed, the nickel nanowires could be seen intact and completely filling the pores of the membrane (Figure 5-8D).

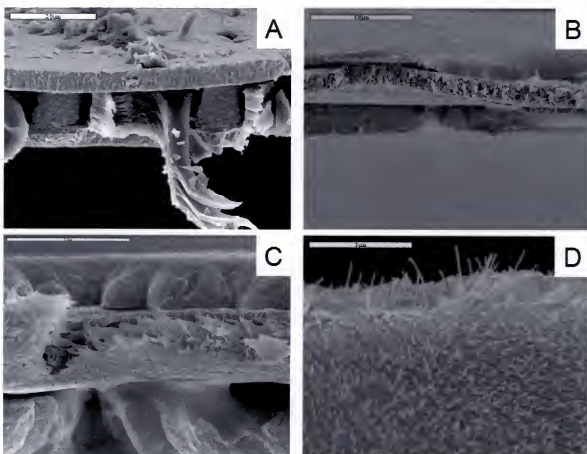


Figure 5-8. SEM micrographs of *complete* molds deposited around track-etch membranes of different pore diameters: A) 10 μm , B) 220 nm, C) 50 nm, and D) 30 nm (After the upper and lower layers of the mold have been removed. Scale bars 20 μm , 50 μm , 10 μm , and 5 μm respectively).

Stability of these molds had to be demonstrated after the removal of the track-etch membrane. Figure 5-9 shows SEM micrographs of nickel molds fabricated via the *incomplete* mold method from a 1.2 μm pore diameter track-etch membrane. Even without the upper layer of the mold (as in the *complete* mold method) to help stabilize the nanorods, the mold still maintained its integrity. The homogeneity of this electrochemical deposition process was also demonstrated by the nanorods of equal length and by the filling of every pore.

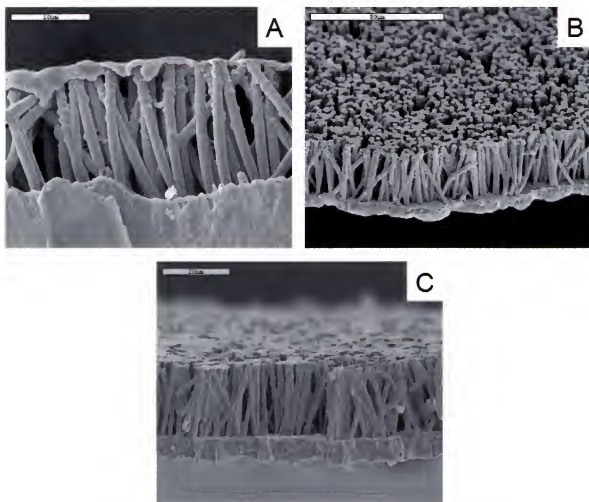


Figure 5-9. SEM micrographs of *incomplete* nickel molds of a 1.2 μm polycarbonate track-etch membrane after removal of the membrane (scale bars 10 μm , 50 μm , and 20 μm respectively).

Presented with a method for the production of a stable mold after the removal of the template membrane, injection of a polymeric material could now be performed. The polymeric materials chosen were PE15000 and PS250000 because it was previously demonstrated their melts could be processed. Polymeric replicas produced via the *complete* mold method had comparable results with either PE15000 (Figure 5-10) or PS250000 (Figure 5-11).

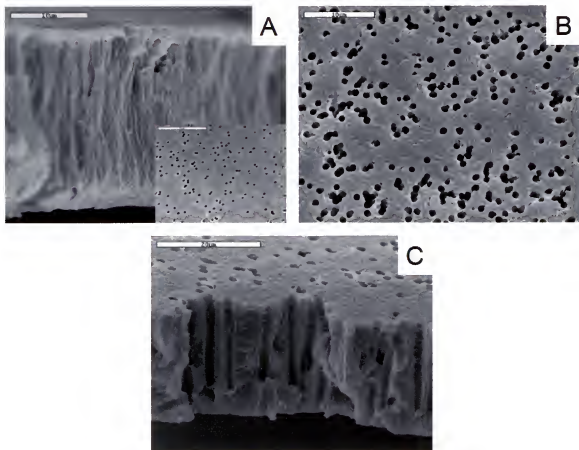


Figure 5-10. SEM micrographs of produced PE15000 replicas from track-etch polycarbonate membranes. A) 50 nm (inset is a surface micrograph), B) 1 μm , and C) 1.8 μm diameters templates (scale bars 10 μm , 2 μm , 10 μm and 20 μm respectively).

Figure 5-10A shows a replica produced from a 50 nm pore diameter track-etch membrane. The morphology on the surface (mostly the pore spacing) was preserved in the replica; however, the internal pore structure seems to have been lost. Attempted

molding of the smaller 30 nm pore diameter membranes suffered from mechanical failure of the mold itself after the removal of the track-etch membrane. The two layers of the mold slightly peeled away from each other. It is known during the electrochemical deposition of nickel from the solution used here, an inherent stress resides in the deposited nickel.¹²² The peeling of the mold is believed to be a relaxation and release of the internal stress within the mold.

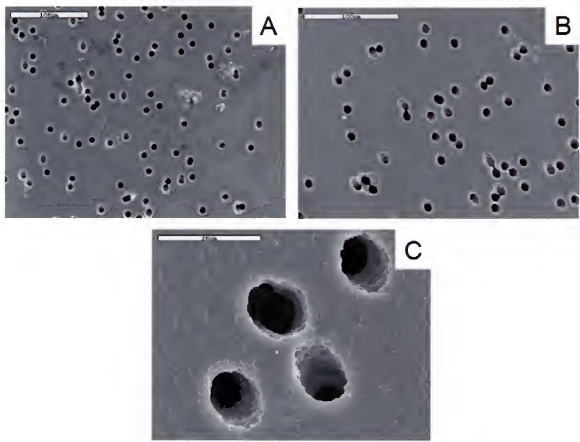


Figure 5-11. SEM micrographs of PS25000 replicas from 10 μm track-etch polycarbonate membranes (scale bars 100 μm , 100 μm , and 20 μm respectively).

The mold relaxation placed a ~100 nm minimal pore diameter limitation on the track-etch membrane that could be replicated. The larger diameter nanorods are able to stabilize the mold and prevent failure from a release of internal stress. This relaxation process was not believed to be a concern for the replication of CP200 membranes

because of their much greater pore densities. Previously mentioned, most track-etch membranes have a porosity of 8%, which translates into 8% of the space between the upper and lower layers of the mold existing as nickel nanowires anchoring the two halves together (Figure 5-12). On the other hand, the nanoporous anodic alumina membranes possess porosities up to 50%. This means a larger percent volume of anchoring nickel nanowires would be present and effectively create a more stable mold.

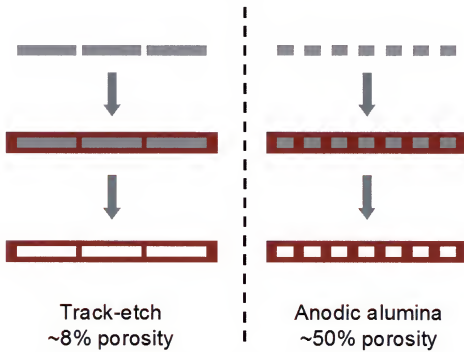


Figure 5-12. Mold formed from a track-etch membrane versus from a nanoporous anodic alumina membrane.

Complete Mold Method Applied to Nanoporous Anodic Alumina Membranes

Figure 5-7 showed nickel could be used to electrochemically place a mold around CP200 membranes. It had to be shown the mold would maintain its integrity after the removal of the CP200 membrane. When the CP200 membrane was dissolved from the nickel mold formed around it, it was ambiguous if the mold had maintained its integrity. This was mostly due to the high density of nickel nanowires (Figure 5-13). Further,

sample preparation artifacts of the cross-sections of the nickel molds for SEM analysis compounded the problem of interpretation. Sample preparation artifacts are expressed in the images as shearing of the sample and “smearing” of nickel nanowires (Figure 5-13B).

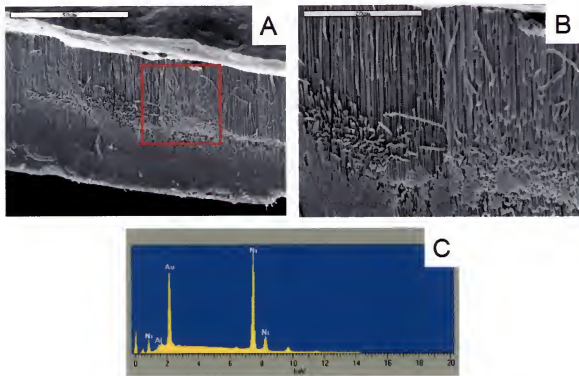


Figure 5-13. SEM micrographs of a nickel mold of a CP200 membrane produced via the *complete* mold method after chemical dissolution of the membrane. A) Micrograph of the cross-section of the mold, B) a higher magnification of marked area in A), and C) energy-dispersive spectrum of marked area in A (scale bars 50 μm , and 20 μm respectively).

However, using Energy-Dispersive Spectroscopy (EDS) we could probe the mold to determine if any alumina material was still present (Figure 5-13C). The distinct and large aluminum and oxygen peaks indicative of alumina were absent, suggesting that all of the original alumina membrane had been removed.

Because we lacked the ability to directly confirm if the mold retained its internal integrity after the removal of the alumina membrane, we proceeded to the next step (the

injection of a polymeric material). By examining the produced replica we could infer the suitability and the integrity of the mold.

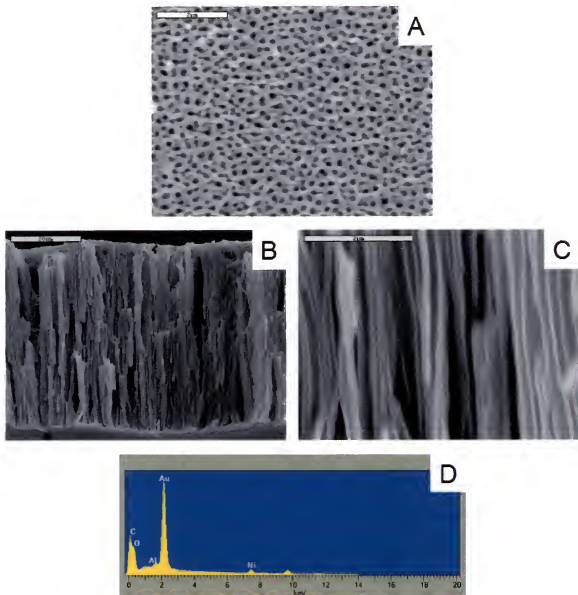


Figure 5-14. SEM micrographs of PE15000 replica produced from CP200 membranes using the *complete* mold method. A) Surface micrograph, B) SEM micrograph of the cross-section, C) higher magnification micrograph of cross-section and D) energy-dispersive spectrum of area imaged in B) (scale bars 2 μm , 20 μm , and 2 μm respectively).

Figure 5-14 shows the SEM micrographs of a PE15000 replica membrane made from a CP200 membrane. EDS analysis indicated the membrane was primarily

composed of the expected polymeric material, denoted by the relatively large carbon peak and trace amounts of aluminum, oxygen and nickel. The replica maintained the surface morphology (the shape and spacing of the pores) of the original CP200 membrane.

The replicas did seem to suffer from a partial loss of the internal pore structure of the original membrane. Examining the micrographs closely, the pores are generally oriented parallel to one another (Figure 5-14C), but some of the pores appear incomplete and possess voids. We concluded these discontinuous pores and voids were a consequence of a lack of complete injection of the polymeric melt into the mold. Apparently, this incomplete filling of the mold resulted from the difficulty in pushing a polymer into the edges of the mold, through the large number of nickel nanorods, and into the center of the mold. One method to enhance the efficiency of injection would be to apply a large pressure behind the polymeric melt, effectively pushing it completely into the mold. However, lacking a chamber where injection can be enhanced with the addition of an external pressure, we were presented with no way to avoid this problem.

The *Incomplete* Mold Method

As designed, the mold was several centimeters wide and injection of the polymeric melt occurred from the edges of the mold. Injection so far from the center of the mold had to be avoided. A new approach was derived and dubbed the *incomplete* mold method (Figure 5-1). This method slightly differed from the *complete* mold method because it lacked the formation of an upper layer of the mold. Injection was now along the entire upper surface of the mold and the melt only had to travel a few microns down

into the mold. This logistical change would greatly enhance the efficiency of the polymer melt injection process.

The *incomplete* mold step-by-step methodology was very similar to the *complete* mold method. The only variation was electrochemical nickel deposition was ceased once there was breakthrough of the nickel nanorods at the upper surface. After removal of the nanoporous anodic alumina membrane, we would expect a large “wheat field” of nanorods to be attached to a nickel base layer. It has been observed that nickel nanorods, of high aspect ratios, tend to lean on one another in clusters when standing freely on a support.¹⁶⁷ Ideally, we would prefer the nickel nanorods to remain parallel to one another and untouched (Figure 5-15A). This would be reflected as perfectly parallel pores in any replica membrane generated from a mold of this type. However, it turns out any leaning of the nanorods to the point of contact with one another would not be catastrophic.

In the ideal case of mold production from a CP200 membrane, we would obtain free-standing nickel nanorods of 200 nm in diameter and 60 μm long. In the non-ideal case, we would obtain nickel nanorods that lean together in small cluster (Figure 5-15B). Due to the high aspect ratios of these nanorods, if they were to lean onto one another there would still be little shift in their overall original orientation, producing little change from ideality in any subsequent replica membrane (Figure 5-15C).

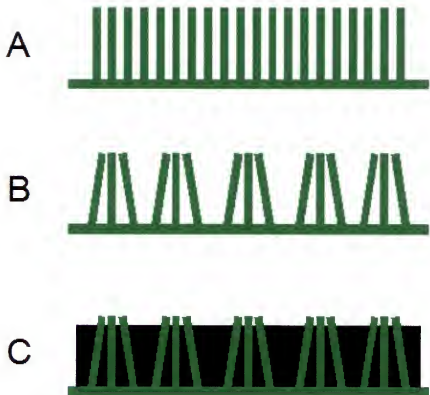


Figure 5-15. Schematics of a mold produced via the *incomplete* mold technique after the removal of the membrane. A) Ideal result, B) non-ideal result, and C) case B) after the introduction of a membrane material.

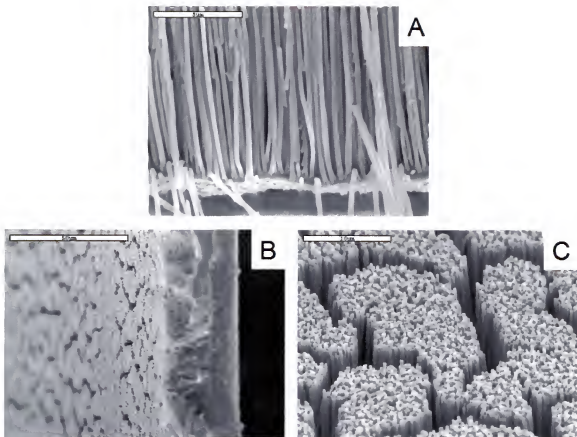


Figure 5-16. SEM micrographs of an *incomplete* mold fabricated from a CP200 membrane. A) and B) are micrographs of different views of the cross-section, and c) is a higher magnification of the upper surface where the nanowires have leaned together (scale bars 5 μ m, 50 μ m, and 10 μ m respectively).

Figure 5-16 shows SEM micrographs of an *incomplete* mold after the removal of the CP200 template membrane. Obviously the spatial location of the nanorods (where they contact the lower layer of the mold) can not change with respect to one another (Figure 5-16A). As expected, on the upper surface (where the nanorods are unsupported) the rods are seen to lean together forming “clusters” on the low micron scale. The low micron scale sized “clusters” and fixed location of the nanorods at their bases supports the assumption there is little change in the nanorod overall orientation and alignment even in the event of rod leaning.

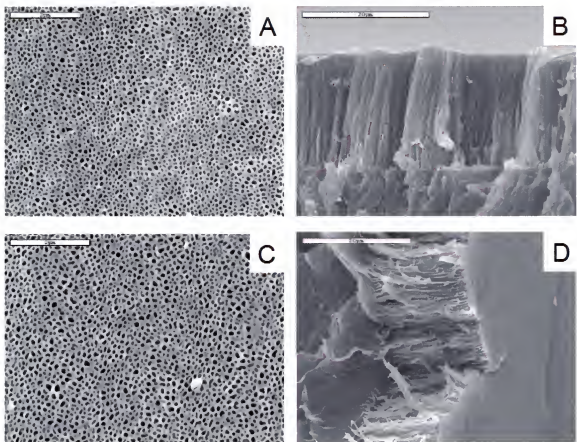


Figure 5-17. SEM micrographs of PE15000 and PS250000 replicas using the *incomplete* mold method . A) Surface and B) cross-section micrographs of PE15000 replica, and C) surface and D) cross-section micrographs of PS250000 replica (scale bars 2 μm , 20 μm , 2 μm and 20 μm respectively).

PE15000 and SP250000 were melted over and injected into these *incomplete* molds. After the, solidification of the polymeric melt, the nickel mold was dissolved (Figure 5-17). The pore spacing and orientation of the replicas at the surface where the nanorods were anchored to the lower layer of the mold have been preserved (A and C). Further, the pores of the replicas running the length of the membranes are essentially parallel to one another (B and D). Having reached this point with such success, the next step is to produce a free-standing replica where the pores are open on both ends (the pores run the full thickness of the membrane).

Conclusions

We have explored several methods for the production of a polymeric replica of track-etch and nanoporous anodic alumina membranes. All methods were centered around the placement of a mold into and around the porous membrane, the removal of the original template membrane, injection of a new polymeric material into the mold, and dissolution of the mold to liberate and recover the replica membrane.

Polyethylene and polystyrene were first selected and utilized as the molding materials. Using their melt properties, they could be readily used to fill the pores and encase the template membrane; however, after removal of the original membrane they lacked the required mechanical properties. This lack of mechanical properties was seen as the leaning and touching of the polymeric nanorods.

Next, nickel a much sturdier substance, was explored as the molding material. First attempts were based upon electroless deposition methods. However, it was found a complete mold could not be produced using these electroless deposition solutions. Coverage of one face of the original membrane was successful but, instead of continuous nickel nanorods, discontinuous nickel nanoparticles were dispersed throughout the length of the pores. Failure of the electroless deposition methods was thought to be a direct result of hydrogen gas formation within the nanometer sized pores.

Electrochemical deposition of a nickel mold was next performed to a much greater success. Based on the *complete* mold method, track-etch membranes with pores as small as 100 nm in diameter could be replicated into polyethylene and polystyrene. Unfortunately, the replicas of nanoporous anodic alumina membranes using the *complete* mold method left much to be desired. At the surface, the pore structures and orientations

were well preserved; but, also deep within the membrane, the internal pore structures seemed discontinuous and contained small voids from incomplete injection of the polymeric material. It was concluded that an external pressure had to be used to promote the complete injection of the polymeric melt. Lacking the means to perform this type of injection the *incomplete* mold method was derived.

The nature of the *incomplete* mold method circumvented the partial injection problem. Replicas produced from nanoporous anodic alumina membranes using the *incomplete* mold method were the most ideal. To date a free-standing replica has not been produced. The next step is to use the *incomplete* mold method to manufacture an ideal replica membrane. Once this is achieved, the use of the *incomplete* mold method will be completely validated for the production of replicas from nanoporous anodic alumina membranes.

CHAPTER 6 CONCLUSIONS

There were two main objectives of this work. The first was to explore the transport properties of nanoporous anodic alumina membranes before and after silane surface modifications. The second was to formulate a method for the production of a polymeric replica of nanoporous anodic alumina membranes. Both objectives utilized nanoporous anodic alumina membranes and reside in the general field of membrane based techniques and technology.

Chapter 1 was presented as an introduction and background source to the vast field of membranes, specifically focusing on track-etch membranes and nanoporous anodic alumina membranes, the substrates used for most of the work in this dissertation. Separations based on membranes, the Langmuir adsorption isotherm, and electroless and electrochemical methods used to deposit materials into these porous membranes were introduced. The basics of scanning electron microscopy (SEM) were also outlined because this was used extensively for method validation in Chapter 5.

In Chapter 2, transport with commercial nanoporous anodic alumina and alkyl silane-treated nanoporous anodic alumina membranes was explored. Surface modification with a C₁₈ alkyl silane rendered the membrane highly hydrophobic and unwettable to aqueous solutions. This was evident due to the prevention of the passage of the charged species Ni²⁺. The properties of these silane-treated membranes were investigated further using a homologous series of permeate molecules. The modified

membranes transported the more hydrophobic member of the family [2,4,6-trimethyphenol (TMP)] faster than the more hydrophilic (phenol). This disparity in flux was quantified by a term called selectivity. The selectivity of these membranes was enhanced when a subphase of kerosene or mineral oil was used to fill the pores.

Phenol was demonstrated to exhibit a Langmuirian adsorption transport behavior with the alkyl silane-treated membranes. Most distinguishing was the exhibited saturation plateau with increasing feed concentrations. When the flux data was fitted to the Langmuirian adsorption equation, good agreement was found between the theory and experimental results. However, at very high feed phenol concentrations pore flooding eventually occurred because of changes in the properties of the aqueous solution.

Chapter 3 explored the modification of nanoporous anodic alumina membranes with three different hydrophobic silanes. For these studies, three distinct alkyl substitutive groups were explored. The first was a silane with two phenyl groups, the second possessed a single alkyl group resembling 8-hydroxyquinoline, and the third was a fluorinated eight member straight alkyl chain. After surface modification with the first two silanes, the pores of the membrane still experienced flooding to aqueous solution. However, the flux of the transported homologous series of permeate molecules was enhanced by a factor of almost three. The third silane, the fluorinated silane, was able to prevent the flooding of the pores, even at high concentrations of phenol. Like the alkyl silane case in Chapter 2, a Langmuirian adsorption transport behavior was observed and fitted to the Langmuir adsorption equation with good agreement.

Kerosene and mineral oil subphases were also introduced into the pores of these three silane-treated membranes. Membranes with the subphases all transported the

homologous series of permeate molecules in the same manner, meaning the primary transport mechanism through any of the membranes containing a subphase was dominated by the partitioning of the analyte into and out of the solvent. The fluorinated membranes could not be modified with a subphase due to a lack of wetting between the organic phase and the fluorinated polymer.

The studies in Chapter 4 returned to the alkyl silane-treated membranes from Chapter 2. However, this time species with two available states (a neutral and charged state depending on solution pH) were chosen. The fluxes of benzoic acid, 2-nitrophenol, pyridine, and aniline were recorded versus the pH of the feed solution. When graphed, a profile very similar to a titration curve, containing an inflection point at the species pK_a value, was observed. It was surmised this behavior could be modeled by each species' alpha curve.

After graphing these results on a log scale versus pH, a remarkable agreement was found between the alpha calculations and experimental results. Further, a linear relationship was found between the flux and calculated concentration of the neutral species at a given pH. This led us to the conclusion that the flux of the species through these membranes only depended on the concentration of the species in the neutral state in solution. Based on all previous results and observations, we predicted species could be concentrated on one side of the membrane or the other depending on the pH in each side of the permeation cell and on the pK_a of the species.

Two-nitrophenol was selected for these experiments. Equal concentrations of 2-nitrophenol were placed on each side of the permeation cell (one side at pH 3 and the other at pH 10). With time, the 2-nitrophenol began to concentrate on the pH 10 side of

the permeation cell. After nearly 24 hours, almost 100% concentration of 2-nitrophenol was obtained. Similarly, 2-nitrophenol and pyridine were predictably separated based on solution pH and their differing pK_as.

Chapter 5 explored the derivation of a method for the production of a polymeric replica of a nanoporous anodic alumina membrane. The basic concepts of the methods explored were as follows. A mold was placed around the alumina membrane, the membrane was subsequently removed, a polymeric material was injected into the mold, and the mold was dissolved for the recovery of the polymeric replica.

The formation of a polymeric mold was then explored. Polyethylene and polystyrene were selected for use to form the polymeric molds. After casting the mold and removal of the original membrane, the polymeric molds were found to lack the needed mechanical properties. The internal spacing of the polymeric rods was not preserved and the internal morphology of the original membrane was lost. With the failure of these polymeric molds, the tougher nickel metal was selected for investigation.

An electrochemical deposition method of nickel, dubbed the *complete* mold method, was used to cast a mold completely around the membranes. This method was first tested with the thinner, and less porous, track-etch membrane family. Polymeric replicas could be fashioned from membranes with pores as small as 100 nm in diameter. However, this method was proven to fail in the replication of nanoporous anodic alumina membranes. The produced polymeric replicas contained small voids and crevices. These defects were a result of incomplete injection of the polymeric material during the injection process. An *incomplete* mold method was formulated to circumvent the injection problems associated with the *complete* mold method.

Unlike the *complete* mold method, the *incomplete* mold method did not completely encase the original membrane, leaving the upper surface of the mold uncovered. This enabled easier and more efficient injection of the polymeric material into the mold. With the *complete* mold method the polymeric melt material had to travel from the edge of the mold several centimeters to the center of the mold, and with the *incomplete* mold method it only had to travel a few microns. This logistical variation was proven to be advantageous with the production of non free-standing replica membranes. The next step is to show the *incomplete* replication method can produce a free-standing replica of nanoporous anodic alumina membranes.

LIST OF REFERENCES

1. Sikdar, S.K.; Grosse, D.; Rogut, I. *J. Mem. Sci.* **1998**, 151, 75-85.
2. Liu, Q; Xiao, J. *J. Mem. Sci.* **2004**, 230, 121-129.
3. Han, S.; Ferreira, F.C.; Livingston, A. *J. Mem. Sci.* **2001**, 188, 219-233.
4. Ferreira, C.F.; Han, S.; Boam, A.; Zhang, S.; Livingston, A.G. *Desalination* **2002**, 148, 267-273.
5. Ferreira, F.C.; Han, S.; Livingston, A.G. *Ind. Eng. Chem. Res.* **2002**, 41, 2766-2774.
6. Pithan, F.; Staudt-Bickel, C.; Lichtenhaler, R.N.; *Desalination* **2002**, 148, 1-4.
7. Simon, J.; Kirchhoff, A.; Gultzow, O. *Talantra* **2002**, 58, 1335-1341.
8. Meindersma, G.W., Haan, A.B. *Desalination* **2002**, 149, 29-34.
9. Chen, S.; Taylor, J.S.; Mulford, L.A.; Norris, C.D. *Desalination* **2004**, 160, 103-111.
10. Lauridsen, F.S.; Kjolholt, J. *Water Res.* **2000**, 34, 3478-3482.
11. Ozaki, H.; Huafang, L. *Water Res.* **2002**, 36, 123-130.
12. Gotoh, T.; Iguchi, H.; Kikuchi, K. *Biochem. Eng. J.* **2004**, 19, 165-170.
13. Yang, X.J.; Fane, A.G.; Soldenhoff, K. *Ind. Eng. Chem. Res.* **2003**, 42, 392-403.
14. Zhang, B.; Gozzelino, G. *Col. Sur. A:Physico. Eng. Aspects* **2002**, 00, 1-10.
15. Alguacil, F.J.; Navarro, P. *Hydrometal.* **2001**, 61, 137-142.
16. Kentish, S.E.; Stevens, G.W. *Chem. Eng. J.* **2001**, 84, 149-159.
17. Kohli, P.K.; Wirtz, M.; Martin, C.R. *Electroanalysis* **2004**, 16, 9-18.
18. Tsai, S.H.; Chao, C.W.; Lee, C.L.; Liu X.W.; Lin, I.N.; Shih, H.C. *Electrochem. Solid-State Letters* **1999**, 2, 247-250.

-
19. Zhao, L.; Yang, W.; Ma, Y.; Yao, J.; Li, J.; Liu, H. *Chem. Commun.* **2003**, 2442-2443.
 20. Zhang, X.Y.; Zhang, L.D.; Chen, W.; Meng, G.W.; Zheng, M.J.; Zhao, L.X. *Chem. Mater.* **2001**, 13, 2511-2515.
 21. Fleischer, R.L. Tracks to Innovation: nuclear tracks in science and technology **1998**, 1-23.
 22. Nikezic, D.; Yu, K.N. *Mater. Sci. Eng. R.* **2004**, 46, 51-123.
 23. Young, D.A. *Science* **1958**, 182, 375.
 24. Ilic, R.; Skvarc, J.; Golovchenko, A.N. *Radiat. Meas.* **2003**, 83-88.
 25. Fleischer, R.L., Price, P.B.; Walker, R.M. Nuclear Tracks in Solids:Nuclear Tracks in Science and Technology **1975**.
 26. Durrani, S.A.; Bull, R.K. Solid State Nuclear Track Detection. Principles, Methods and Applications **1987**.
 27. Durrani, S.A.; Ilie, R. Radon Measurements be Etched Track Detectors **1997**.
 28. Poretics Catalog: Microfiltration & Laboratory Products **1995**.
 29. Apel, P. *Rad. Meas.* **2001**, 34, 559-566.
 30. Apel, P. *Nucl. Instru. Meth. Phys. Res. B.* **2003**, 208, 11-20.
 31. Fisher Scientific Literature. **2004**.
 32. Thompson, G.E.; Wood, G.C. *Treatise Mat. Sci & Tech.* **1983**, 23, 205-329.
 33. Smith, A.W. U.S. Patent, **1974**, no. 3,850,762.
 34. Shimizu, K.; Habazaki, H.; Skeldon, P.; Thompson, G.E.; Wood, G.C. *Electrochim. Acta* **2000**, 45, 1805-1809.
 35. Masuda, H.; Hasegwa, F. *Electrochem. Soc.* **1997**, 144, L127-L130.
 36. Thompson, G.E.; Furneaux, R.C.; Wood, G.C. *Corrosion Sci.* **1978**, 18, 481-498.
 37. Patermarakis, G. *J. Electroanal. Chem.* **1996**, 404, 69-76.

-
- 38. Patermarakis, G.; Moussoutzanis, K. *Corrosion Sci.* **2001**, 43, 1433-1464.
 - 39. Ba, L.; Li, W.S. *J. Phy. D* **2000**, 33, 2527-2531.
 - 40. Li, F; Zhang, L.; Metzger, R.M. *Chem. Mater.* **1998**, 10, 2470-2480.
 - 41. Thompson, G.E. *Thin Sol. Films* **1997**, 297, 192-201.
 - 42. Li, A.P.; Muller, F.; Birner, A.;Nielsch, K.; Gosele, U. *J. Appl. Phy.* **1998**, 84, 6023-6026.
 - 43. Li, A.P.; Muller, F.; Birner, A.;Nielsch, K.; Gosele, U. *J. Vac. Sci. Technol. A* **1999**, 17, 1428-1431.
 - 44. Jessensky, O.; Muller, F.; Gosele, U. *Appl. Phys. Lett.* **1998**, 72, 1173-1175.
 - 45. Li, A.P.; Muller, F.; Gosele, U. *Electrochem. Sol.St. Lett.* **2000**, 3, 131-134.
 - 46. Jessensky, O.; Muller, F.; Gosele, U. *J. Electrochem. Soc.* **1998**, 145, 3735-3740.
 - 47. Palibroda, E.; Farcas, T.; Lupsan, A. *Mat. Sci. Eng.* **1995**, 1-5.
 - 48. Furneaux, R.C.; Rigby, W.R.; Davidson, A.P. *Nature* **1986**, 337, 147-149.
 - 49. Li, A.P.; Muller, F.; Birner, A.;Nielsch, K.; Gosele, U. *Adv. Mater.* **1999**, 11, 483-487.
 - 50. Almawlawi, D.; Bosnick, K.A.; Osika, A.; Moskovits, M. *Adv. Mater.* **2000**, 12, 1252-1257.
 - 51. Asoh, H.; Nishio, K.; Nakao, M.; Tamamura, T.; Masuda, H. *J. Electrochem. Soc.* **2001**, 148, B152-B156.
 - 52. Yakovleva, N.M.; Yakolev, A.N.; Chupakhina, E.A. *Thin Sol. Films* **2000**, 366, 37-42.
 - 53. Masuda, H.; Kanezawa, K.; Nishio, K. *Chem. Lett.* **2002**, 1218-1219.
 - 54. Masuda, H.; Yamada, H.; Satoh, M.; Asoh, H.; Nakao, M; Tamamura, T. *Appl. Phys. Lett.* **1997**, 71, 2770-2772.
 - 55. Asoh, H.; Ono, S.; Hirose, T.; Nakao, M.; Masuda, H. *Electrochim. Acta* **2003**, 48, 3171-3174.

-
- 56. Masuda, H.; Asoh, H.; Watanabe, M.; Nishio, K.; Nakao, M.; Tamamura, T. *Adv. Mater.* **2001**, 13, 189-192.
 - 57. Shawaqfeh, A.T.; Baltus, R.E. *J. Mem. Sci.* **1999**, 157, 147-158.
 - 58. Hoyer, P.; Nishio, K.; Masuda, H. *Thin Sol. Films* **1996**, 286, 88-91.
 - 59. Itoh, N.; Kato, K.; Tsuji, T.; Hongo, M. *J. Mem. Sci.* **1996**, 117, 189-196.
 - 60. Itoh, N.; Kato, K.; Tsuji, T.; Hongo, M. *Micropor. Mesopor. Mater.* **1998**, 20, 333-337.
 - 61. Bungay, P.M.; Lonsdale, H.K.; Pinho, M.N. *Synthetic Membranes:Science, Engineering and Applications* **1983**, V.181, 1-155.
 - 62. Mulder, M. *Basic Principles of Membrane Technology* **1996**, 2nd ed., 1-18.
 - 63. *Membrane Science and Technology* **1992**, Edited by: Osada, Y.; Nakagawa, T. 1-57.
 - 64. Koros, W.J.; Ma, Y.H.; Shimidzu, T. *J. Mem. Sci.* **1996**, 120, 149-159.
 - 65. Mita, D.G.; Rossi, S.; Bencivenga, U.; Pagliuca, N.; D'Acunto, A.; Peluso, F.; Gaeta, F.S. *J. Mem. Sci.* **1996**, 115, 191-206.
 - 66. Zhang, Y.K.; Kocherginsky, N.M. *J. Mem. Sci.* **2003**, 225, 105-114.
 - 67. Rovinsky, L.A.; Yarovenko, V.L. *J. Food Eng.* **1995**, 24, 511-528.
 - 68. Kargol, A. *J. Mem. Sci.* **2001**, 191, 61-69.
 - 69. Yu, S.; Lee, S.B.; Martin, C.R. *Anal. Chem.* **2003**, 75, 1239-1244.
 - 70. Gill, J.S.; Singh, H.; Gupta, C.K. *Hydrometallurgy* **2000**, 55, 113-116.
 - 71. Gyves, J.; Miguel, E.R. *Ind. Eng. Chem. Res.* **1999**, 38, 2182-2202.
 - 72. Alhusseini, A.; Ajbar, A. *Math. Com. Mod.* **2000**, 32, 465-480.
 - 73. Gelest Inc. product catalog.
 - 74. Skoog, D.A.; Leary, J.J. *Principles of Instrumental Analysis*. 4th ed. **1992**.
 - 75. Yang, S.S.; Gilpin, R.K.; *Anal. Chem.* **1987**, 59, 2750-2752.

-
76. Dressick, W.J.; Dulcey, C.S.; Chen, M.; Calvert, J.M. *Thin Solid Films* **1996**, 284, 568-572.
 77. Solymos, K.G.; Varhegy, B.; Kalman, F.H.; Gal, M.; Hencsei, P.; Bihatsi, L. *Corros. Sci.* **1993**, 35, 1455-1457.
 78. Friessnegg, T.; Boudeau, M.; Brown, J.; Mascher, P.; Simpson, P.S.; Puff, W. *J. Appl. Phys.* **1996**, 80, 2216-2223.
 79. Peanasky, J.; Schneider, H.M.; Granick, S. *Langmuir* **1995**, 11, 953-962.
 80. Feng, X.; Fryxell, G.E.; Wang, L.; Kim, A.Y.; Kemner, K.M. *Science* **1997**, 275, 923-926.
 81. Langmuir, I. *J. Am. Chem. Soc.* **1916**, 38, 2221-2295.
 82. Saeed, M.M.; Ahmed, M. *Analytica Chim. Act.* **2004**, 525, 289-297.
 83. Ho, Y.; Chiang, T.; Hsueh, Y. *Process Biochem.* **2005**, 40, 119-124.
 84. Dogan, M.; Alkan, M.; Onganer, Y. *Water, Air, Soil Pollut.* **2000**, 120, 229-248.
 85. http://orac.sunderland.ac.uk/~hsobcl/gg/langmuir_isotherm.htm **2004**.
 86. www.jhu.edu/~chem/fairbr/Derive.html **2004**.
 87. http://www.chem.qmw.ac.uk/surfaces/scc/scat3_1.htm
 88. <http://www.erpt.org/012Q/NelsW-07.htm> **2004**.
 89. Wang, S.; Boyjoo, Y.; Choueib, A.; Zhu, Z. *Water Resear.* **2004**, article in press.
 90. Silva, J.P.' Sousa, S.; Rodrigues, J.; Antunes, H.; Porter, J.J.; Goncalves, I.; Dias, S.F. *Sep. Purifi. Technol.* **2004**, 40, 309-315.
 91. Hullebusch, E.D.; Peerbolte, A.; Zandvoort, M.H.; Lens, P.N. *Chemosphere* **2004**, article in press.
 92. Davis, T.A.; Volesky, B.; Mucci, A. *Water Resear.* **2003**, 37, 4311-4330.
 93. Al-Qunaibit, M.H.; Mekhemer, W.K.; Zaghloul, A.A. *J. Col. Interface Sci.* **2004**, article in press.
 94. Ngah, W.S.; Ghani, S.A.; Kamari, A. *Bioresour. Technol.* **2005**, 96, 443-450.

-
95. Ghiaci, M.; Abbaspur, A.; Kia, R.; Seyedeyn-Azad, F. *Separat. Purificat. Technol.* **2004**, 40, 217-229.
 96. Fallah, M.Z.; Guiochon, G. *Anal. Chem.* **1991**, 63, 859-867.
 97. Fallah, M.Z.; Guiochon, G. *Anal. Chem.* **1991**, 63, 2244-2252.
 98. Surfaces of Nanoparticales and Porous Materials. Edited by Schwarz, J.A.; Contescu, C.I. **1999**.
 99. Goldstein, J.I.; Newbury, D.E.; Echlin, P.; Joy, D.C.; Romig, A.D.; Lyman, C.E.; Fiori, C.; Lifshin, E. Scanning Electron Microscopy and X-Ray Microanalysis **1992**.
 100. Knoll, M. *Z. Tech. Phys.* **1935**, 11, 467.
 101. Ardenne, M.V. *Z. Phys.* **1938**, 109, 553.
 102. Ardenne, M.V. *Z. Techn. Phys.* **1938**, 19, 407.
 103. Zworykin, V.K.; Hillier, R.L.; Snyder, R.L. *ASTM Bullet.* **1942**, 117, 15.
 104. Electron Microscopy: Principles and Fundamentals. Edited by Amelinckx, S.; Dyck, D.; Landuyt, J.; Tendeloo, G. **1997**.
 105. Berger, M. Methods in Computational Physics I. **1963**.
 106. Shimizu, R.; Murata, K. *J. Appl. Phys.* **1971**, 42, 387.
 107. Heinrich, K.F.J. *Adv. in Optical and Elec. Microsc.* **1975**, 6, 275.
 108. Newbury, D.E.; Myklebust, R.L. Electron Beam Interactions with Solids **1984**.
 109. Heinrich, K.F.L.; Newbury, D.E. Electron Probe Quantitation **1991**.
 110. Joy, D.C. Monte Carlo Modeling for Electron Microscopy and Microanalysis **1995**.
 111. Electroless Plating: Fundamentals and Applications. Edited by Mallory, G.O.; Hajdu, J.B. **1987**.
 112. Nishizawa, M.; Menon, V.P.; Martin, C.R. *Science* **1995**, 268, 700-702.
 113. Yu, S.; Li, N.; Wharton, J.; Martin, C.R. *Nano Lett.* **2003**, 3, 815-818.

-
114. Jirage, K.B.; Hulteen, J.C.; Martin, C.R. *Science* **1997**, 278, 655-658.
 115. Yu, S.; Lee, S.B.; Kang, M.; Martin, C.R. *Nano Lett.* **2001**, 1, 495-498.
 116. Kobayashi, Y.; Martin, C.R. *J. Electroanal. Chem.* **1997**, 431, 29-33.
 117. Miller, T.C.; Holcombe, J.A. *Anal. Chim. Acta* **2002**, 454, 37-44.
 118. Jirage, K.B.; Hulteen, J.C.; Martin, C.R. *Anal. Chem.* **1999**, 71, 4913-4918.
 119. Martin, C.R.; Nishizawa, M.; Jirage, K.; Kang, M.; Lee, S.B. *Adv. Mater.* **2001**, 13, 1351-1361.
 120. Steinle, E.D.; Mitchell, D.T.; Wirtz, M.; Lee, S.B.; Young, V.Y.; Martin, C.R. *Anal. Chem.* **2002**, 74, 2416-2422.
 121. Lowenheim, F.A. Guide to the Selection and Use of Electro-plated and Related Finishes **1982**.
 122. Dennis, J.K.; Such, T.E. Nickel and Chromium Plating **1986**, ch. 11.
 123. Bird, G.; *Phil. Trans.* **1837**, 127, 37.
 124. Parthasaradhy, N.V. Practical Electroplating Handbook **1989**, 183.
 125. Watts, O.P. *Trans. Am. Electrom. Soc.* **1916**, 29, 395.
 126. Lee, S. B.; Mitchell, D.T.; Trofin, L.; Nevanen, T.K.; Soderlund, H.; Martin, C.R. *Science* **2002**, 296, 2198-2200
 127. Ott, A.W.; Klaus, J.W.; Johnson, J.M.; George, S.M. *Chem. Mater.* **1997**, 9, 707-714.
 128. Kyotani, T.; Xu, W.; Yokoyama, J.I.; Touhara, H.; Tomita, A. *J. Mem. Sci.* **2002**, 196, 231-239.
 129. Martinez, F.; Martin, A.; Pradanos, P.; Calvo, J.I.; Palacio, L.; Hernandez, A. *J. Col. Inter. Sci.* **2000**, 221, 254-261.
 130. Martin, A.; Martinez, F.; Calvo, J.I.; Pradanos, P.; Palacio, L.; Hernandez, A. *J. Mem. Sci.* **2002**, 207, 199-207.
 131. Wu, J.C.; Lee, E. *J. Mem. Sci.* **1999**, 154, 251-259.

-
- 132. Shui, Y.C.; Cui, B.Z.; Guardian, R.; Acosta, D.R., Martinez, L.; Perez, R. *Carbon* **2002**, 40, 1011-1016.
 - 133. Ji, G.B.; Chen, W.; Tang, S.L.; Gu, B.X.; Li, Z.; Du, Y.W. *Sol. St. Com.* **2004**, 130, 541-545.
 - 134. Kovtyukhuva, N.I.; Martin, B.R.; Mbido, J.K.; Mallouk, T.E.; Cabassi, M.; Mayer, T.S. *Mat. Sci. Eng. C* **2002**, 19, 255-262.
 - 135. Zhao, J.; Gao, Q.Y.; Gu, C.; Yang, Y. *Chem. Phys. Let.* **2002**, 24, 77-82.
 - 136. Varghese, O.K.; Gong, D.; Dreschel, W.R.; Ong, K.G.; Grimes, C.A. *Sen. Actua. B* **2003**, 94, 27-35.
 - 137. Lazarouk, S.; Katsouba, S.; Demianovich, A.; Stanovski, V.; Voitech, S.; Vysotski, V.; Ponomar, V. *Sol. St. Elec.* **2000**, 44, 815-818.
 - 138. Li, Y.; Holland, E.R.; Wilshaw, P.R. *J. Vac. Sci. Tech. B* **2000**, 18, 994-996.
 - 139. Whatman Corporation literature.
 - 140. Parthasarathy, R.V.; Martin, C.R. *Chem. Mater.* **1994**, 6, 1627-1632.
 - 141. Lakshmi, B.B.; Patrissi, C.J.; Martin, C.R. *Chem. Mater.* **1997**, 9, 2544-2550.
 - 142. Cepak, V.M.; Martin, C.R. *Chem. Mater.* **1999**, 11, 1363-1367.
 - 143. Cepak, V.M.; Hulteen, J.C.; Che, G.; Jirage, K.B.; Lakshmi, B.B.; Fisher, E.R.; Martin, C.R. *Chem. Mater.* **1997**, 9, 1065-1067.
 - 144. Hulteen, J.C.; Martin, C.R. *J. Mater. Sci.* **1997**, 7, 1075-1087.
 - 145. Hulteen, J.C., Jirage, K.; Martin, C.R. *J. Am. Chem. Soc.* **1998**, 120, 6603, 6604.
 - 146. Jirage, K.B.; Martin, C.R. *TIBTECH* **1999**, 17, 197-200.
 - 147. Plueddemann, E.P. *Silane Coupling Agents* **1992**.
 - 148. Chimuka, L.; Mathiasson, L.; Jonsson, J. *Anl. Chim. Act.* **2000**, 416, 77-86.
 - 149. Farell, S.; Sirkar, K.K. *J. Contr. Rel.* **1999**, 61, 345-360.
 - 150. U.S. Army Corp of Engineers®. Soil Vapor Extraction and Bioventing, 3, June, **2002**, appendix B.

-
151. Berthod, A.; Broch, S.C. *J. Chrom. A.* **2004**, 1037, 3-14.
 152. Carracedo, M.P.; Andrade, J.M.; Fernandez, E.; Prada, D.; Muniategui, S. *Fuel* **2003**, 82, 1211-1218.
 153. Grob, K.; Vass, M.; Biedermann, M.; Neukom, H.P. *Food Add. Contam.* **2001**, 18, 1-10.
 154. Brookes, P.R.; Livingston, A.G. *J. Mem Sci.* **1995**, 104, 119-137.
 155. Han, S.; Puech, L.; Law, R.V.; Steinke, J.H.G.; Livingston, A. *J. Mem. Sci.* **2002**, 199, 1-11.
 156. Dastgir, M.G.; Ferreira, F.C.; Peeva, L.; Livingston, A.G. *J. Chem. Tech. Biotech.* **2004**, 79, 381-390.
 157. Wirtz, M.; Parker, M.; Kobayashi, Y.; Martin, C.R. *Chem. Record* **2002**, 2, 259-267.
 158. Foss, C.A.; Hornyak, G.L.; Stockert, J.A.; Martin, C.R. *J. Phys. Chem.* **1994**, 98, 2963-2971.
 159. Hornyak, G.L.; Martin, C.R. *Thin Solid Films* **1997**, 303, 84-88.
 160. Brumlik, C.J.; Martin, C.R. *J. Am. Chem. Soc.* **1991**, 113, 3174-3175.
 161. Liang, W.; Martin, C.R. *J. Am. Chem. Soc.* **1990**, 112, 9666-9668.
 162. Cai, K.; Lei, J.; Liang, W.; Menon, V.; Martin, C.R. *Chem. Mater.* **1991**, 3, 960-967.
 163. Brumlik, C.J.; Martin, C.R. *Anal. Chem.* **1992**, 64, 1201-1203.
 164. Lakshmi, B.B.; Dorhout, P.K.; Martin, C.R. *Chem. Mater.* **1997**, 9, 857-862.
 165. Parthasarathy, R.V.; Martin, C.R. *Nature* **1994**, 369, 298-301.
 166. Schononberger, C.; Zande, B.M.; Fokkink, G.J.; Henny, M.; Schmid, C.; Kruger, M.; Bachtold, A.; Huber, R.; Birk, H.; Staufer, U. *J. Phys. Chem.* **1997**, 101, 5497-5505.
 167. Chu, S.Z.; Wada, K.; Inoue, S.; Todoroki, S. *Electrochim. Acta* **2003**, 48, 3147-3153.

168. Tanase, M.; Bauer, L.S.; Hultgren, A.; Silevitch, D.M.; Sun, L.; Reich, D.H.; Searson, P.C.; Meyer, G.J. *Nano Lett.* **2001**, 1, 155-158.
169. Dobrev, D.; Neumann, R.; Angert, N.; Vetter. *Appl. Phys. A.* **2003**, 76, 787-790.
170. Dobrev, D.; Vetter, J. *Nucl. Instr. And Meth. In Phys. Res. B* **1999**, 156, 177-182.
171. Masuda, H.; Nishio, K.; Baba, N. *Thin Solid Films* **1993**, 223, 1-3.
172. Hoyer, P.; Baba, N.; Masuda, H. *Appl. Phys. Lett.* **1995**, 66, 2700-2702.
173. Ohmori, T.; Kimura, T.; Masuda, H. *J. Electrochem. Soc.* **1997**, 144, 1286-1288.
174. Masuda, H.; Fukuda, K. *Science* **1995**, 268, 1466-1468.
175. Masuda, H.; Mizuno, T.; Baba, N.; Ohmori, T. *J. Electroanal. Chem.* **1994**, 368, 333-336.
176. Hoyer, P.; Masuda, H. *J. Mater. Sci. Lett.* **1996**, 15, 1228-1230.
177. Masuda, H.; Fukuda, K. *J. Electroanal. Chem.* **1999**, 473, 240-244.
178. Jiang, K.; Wang, Y.; Gui, L.; Tang, Y. *Col. And Surf. A:Physiochem. Eng. Aspects* **2001**, 179, 237-241.
179. Lei, Y. Liang, C.H.; Wu, Y.C.; Zhang, L.D. *J. Vac. Sci. Technol. B* **2001**, 19, 1109-1114.

BIOGRAPHICAL SKETCH

Damian Odom was born and raised in Jacksonville, Florida, the third son of three to Bobbie and Soloman Odom. At the University of North Florida he discovered his interest and aptitude for science. This interest has increased with every passing day, and so has his dedication. After completing his Ph.D., he intends to move on into the industrial sector to use the knowledge he has gained over the years. In addition to science, Damian also enjoys various outdoor activities such as biking, hiking, camping, and the study of martial arts.

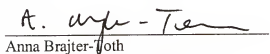
I certify that I have read this study and that in my opinion it conforms to acceptable standards of scholarly presentation and is fully adequate, in scope and quality, as a dissertation for the degree of Doctor of Philosophy.


Charles R. Martin, Chair
Professor of Chemistry

I certify that I have read this study and that in my opinion it conforms to acceptable standards of scholarly presentation and is fully adequate, in scope and quality, as a dissertation for the degree of Doctor of Philosophy.


Richard Yost
Professor of Chemistry

I certify that I have read this study and that in my opinion it conforms to acceptable standards of scholarly presentation and is fully adequate, in scope and quality, as a dissertation for the degree of Doctor of Philosophy.


Anna Brajter-Yost
Associate Professor of Chemistry

I certify that I have read this study and that in my opinion it conforms to acceptable standards of scholarly presentation and is fully adequate, in scope and quality, as a dissertation for the degree of Doctor of Philosophy.


James Deyrup
Professor of Chemistry

I certify that I have read this study and that in my opinion it conforms to acceptable standards of scholarly presentation and is fully adequate, in scope and quality, as a dissertation for the degree of Doctor of Philosophy.


Rolf Hummel
Professor of Materials Science and
Engineering

This dissertation was submitted to the Graduate Faculty of the Department of Chemistry in the College of Liberal Arts and Sciences and to the Graduate School and was accepted as partial fulfillment of the requirements for the degree of Doctor of Philosophy.

May 2005

Dean, Graduate School